

AUS Repository

Adopting Geophysical Testing Techniques in Geotechnical Investigation and Shallow Foundation Design

Item Type	Thesis
Authors	Amer, Mohammad
Download date	2026-03-16 05:48:31
Link to Item	http://hdl.handle.net/11073/9308

ADOPTING GEOPHYSICAL TESTING TECHNIQUES IN GEOTECHNICAL
INVESTIGATION AND SHALLOW FOUNDATION DESIGN

by

Mohammad Amer

A Thesis presented to the Faculty of the
American University of Sharjah
College of Engineering
In Partial Fulfillment
of the Requirements
for the Degree of

Master of Science in
Civil Engineering

Sharjah, United Arab Emirates

Spring 2018

Approval Signatures

We, the undersigned, approve the Master's Thesis of Mohammad Amer

Thesis Title: Adopting Geophysical Testing Techniques in Geotechnical Investigation and Shallow Foundation Design.

Signature

Date of Signature
(dd/mm/yyyy)

Dr. Magdi El-Emam
Associate Professor, Department of Civil Engineering
Thesis Advisor

Dr. Mousa Attom
Professor, Department of Civil Engineering
Thesis Committee Member

Dr. Samir Emam
Associate Professor, Department of Mechanical Engineering
Thesis Committee Member

Dr. Robert John Houghtalen
Head, Department of Civil Engineering

Dr. Ghaleb Hussein
Associate Dean, College of Engineering

Dr. Richard T. Schoephoerster
Dean of College of Engineering

Dr. Mohamed El-Tarhuni
Vice Provost for Graduate Studies

Acknowledgements

Being at this major stage of my life, I would like to first express my gratitude to Allah, the Almighty God, for granting me the strength and patience to go through all the challenges, overcome each and every obstacle in the journey of this thesis, and achieve my master's degree.

Secondly, I would like to thank all the people who supported me and were always there to keep me moving forward. I want to start with my great parents, Okab Amer and Mona Jarbough, who gave me all the love and motivation, and always believed in me. I can never succeed without you. In addition, I would like to convey my thanks to my sisters, Rasha, Rama, Roua, and Leen, for their continuous support, and for standing next to me in every step I took in this journey.

Thirdly, I would like to express my great thanks to my mentor and advisor, Dr. Magdi El-Emam, who was with me from the first step, providing me with valuable pieces of advice and always directing me to the right track. His knowledge, experience, and his huge efforts are main reasons to accomplish this research.

I am also thankful to Eng. Aqeel Ahmed for his help, patience, and support in my experimental work at the Geotechnical Lab at the American University of Sharjah (AUS). He helped me to overcome several difficulties faced in the lab. Special thanks go to Mr. Ibrahim Abu Saif, Senior Laboratory Instructor at the AUS, for his support in electronic connections of the accelerometers, and for providing us with the Pico Scopes used in this study.

I would also like to acknowledge AUS and the College of Engineering for the financial support in the form of Graduate Teaching Assistantship (GTA). Additional funding to support my research was also provided by research grant from the AUS awarded to Dr. El-Emam.

Dedication

To my beloved Family

Okab Amer, Mona Jarbou, Rasha Amer, Rama Amer, Roua Amer & Leen Amer

Abstract

The purpose of the current research is to implement Geophysical Techniques (GT) in measuring small strain wave velocity at different soil properties. Soil properties that are considered include void ratio (degree of compaction), water content (degree of saturation), particle sizes (gradation), clay content, and cement content. Furthermore, to develop a soil wave velocity-stress relationship, wave velocity through externally loaded soil is measured under a shallow foundation applying different vertical stresses. To fulfill the investigation purpose, local sand was collected and subjected to in-depth laboratory tests, such as sieve analysis, compaction tests, shear tests, and full soil classification. For index tests, twenty 6-in-diameter specimens were prepared with different soil properties. In addition, two identical 1/3-scale strip footing model tests are constructed and instrumented with geophones, accelerometers, and load cells. The purpose of these tests is to establish correlations between wave velocities measured on granular materials at different applied vertical stresses. These relationships can be utilized to predict, from *in situ* velocity measurements, the velocity expected under a shallow foundation required for numerical modeling of various soil materials. Index test results indicate that the P-wave velocity decreases by 40 to 70% as the soil water content increases up to certain thresholds of 3.5 to 4%, which itself increases with compaction effort. In addition, the wave velocity increases by 30 to 80% when sand gradation tends to be fine. A 10% clay content increases the sand wave velocity by 40% in dry condition and 200% in wet condition. Results also show that the addition of 3% Portland cement resulted in a 5 time increase in soil wave velocity, especially after three-days of curing time. The scaled footing tests indicate that the P-wave velocity increases nonlinearly as the footing applied stress increases, and the largest value was measured directly at the bottom of footing. For practical implementation, a nonlinear relationship has been developed to calculate the increase in the P-wave velocity due to footing external applied stress. This increase can be used together with measured *in situ* velocity, which can be measured using any suitable geophysical method, to estimate the change in soil modulus at different depths below the footing.

Search Terms: *Nondestructive techniques, Wave velocity, Geophones, Accelerometers, Soil properties, Strip footing.*

Table of Contents

Abstract	6
List of Figures	9
Chapter 1: Introduction	13
1.1. General	13
1.2. Problem Statement	14
1.3. Research Objectives	15
1.4. Significance of the Research	16
1.5. Thesis Organization.....	16
Chapter 2: Literature Review	18
2.1. General	18
2.2. Geophysical Technique	18
2.3. Geophysical Technique and Bearing Capacity	22
2.4. Bearing Capacity Wave Relations.....	24
2.5. Types of Failure in Sandy Soil at Ultimate Load.....	27
2.6. Bearing Capacity of Shallow Foundation	29
2.7. Settlement of Shallow Foundation	30
Chapter 3: Experimental Work	39
3.1. General	39
3.2. Soil Properties	39
3.3. Accelerometers and Pico Scope	44
3.4. Sensitivity Analysis	45
3.5. Parameters Studied in Index Tests	52
3.6. Scaled Footing Test	56
3.6.1. General.....	56
3.6.2. Sand box and model instrumentations	56
3.6.3. Model compaction	62

3.6.4. Signal processing and interpretation.....	63
Chapter 4: Results and Discussion.....	68
4.1. General	68
4.2. Index Tests Results.....	68
4.2.1. Effect of degree of compaction and void ratio	70
4.2.2. Effect of soil grain size distribution (soil gradation).....	73
4.2.3. Effect of clay content.....	76
4.2.4. Effect of portland cement content	78
4.3. Strip Footing Test.....	82
4.3.1. General.....	82
4.3.2. Wave velocity at different vertical stresses	83
4.3.3. Average velocities	91
Chapter 5: Conclusion and Recommendations	98
5.1 Conclusion.....	98
5.2 Recommendations for Future Research	100
References.....	101
Vita.....	105

List of Figures

Figure 1: Multi-Channels Surface Wave Analysis (MCSWA) technique	19
Figure 2: Example of recorded multi-channel data in MCSWA method and processing steps	20
Figure 3: Comparative results of ‘Conventional’ and ‘Dynamic’ methods [19]	23
Figure 4: Shear failure in soil, and variation of bearing capacity with foundation settlement.....	28
Figure 5: Nature of failure in soil with relative density of sand (D_r) and D_f/R [22].....	29
Figure 6: Variation of S_w/B for surface foundation (D_f/B) on sand [22]	31
Figure 7: Evaluation of travel time [25]	32
Figure 8: Shear wave velocities versus moisture content [29]	34
Figure 9: Shear wave velocities versus void ratio [28].....	35
Figure 10: Velocity versus clay content for dry sand-clay mixtures [29].....	36
Figure 11: Shear wave velocity versus moisture content obtained for different compaction efforts [30].....	37
Figure 12: Grain size data, sand-gravel mixes [31]	37
Figure 13: Influence of gravel content on shear wave velocity [31]	38
Figure 14: gradation for RAK original sand and fine sand passing 2mm sieve	40
Figure 15: Dry unit weight versus water content (%).....	42
Figure 16: Direct shear test results for RAK sand	43
Figure 17: Liquid limit test for the clay soil	43
Figure 18: Accelerometers used in the current investigation.....	44
Figure 19: Pico Scope used for recording accelerometers output signals	45
Figure 20: Compacted sandy soil samples with different dimensions and different boundary conditions.....	47
Figure 21: Example of generated and received waves at both sides of the soil specimen	48
Figure 22: Steel plate attached to accelerometer base “base plate”	50
Figure 23: Clamping the soil specimen to a rigid table	50
Figure 24: Final set-up for index tests	51
Figure 25: Example of dried specimen after fully tested.....	54
Figure 26: Dissolved sample after soaking in water	55
Figure 27: Schematic diagram for the large scale test model for strip footing with geophones and accelerometers.....	57

Figure 28: Two load cells under the actuator, LVDT's, strip footing, and reaction beam.....	58
Figure 29: Example time lag of two accelerometers readings.....	58
Figure 30: Applied vertical stress increment on the top of the strip footing	59
Figure 31: Locations of top and side impact pulse hits	60
Figure 32: Locations of Accelerometers and geophones inside the sand and at the backfill surface.....	61
Figure 33: Data acquisition used with load cells and LVDT's.....	62
Figure 34: Soil compaction stages during construction of the model footing	63
Figure 35: transmitted signals from a bender element test [35].....	64
Figure 36: Time domain interpretation methods [35].....	65
Figure 37: Input, output, and cross-correlation signals [40].....	66
Figure 38: Determination of the accelerometers first arrival times.	67
Figure 39: Determination of geophones first arrival times.....	67
Figure 40: Using the first arrival for estimating the travel time	69
Figure 41: Using peak-to-peak, and first arrival for estimating the travel time	70
Figure 42: variation of P-wave velocity with water content, at different compaction effort.....	72
Figure 43: variation of P-wave velocity with degree of saturation, at different compaction effort	72
Figure 44: variation of P-wave velocity with void ratio, at different compaction water content.....	73
Figure 45: Variation of P-wave velocity with soil water content, for different soil types	74
Figure 46: Variation of P-wave velocity with soil degree of saturation, for different soil types	75
Figure 47: Comparison of P-wave velocity for soil types, at different soil degree of saturation.....	75
Figure 48: Variation of P-wave velocity with soil water content, at different clay contents	77
Figure 49: Variation of P-wave velocity with soil degree of saturation, at different clay contents.....	78
Figure 50: Variation of P-wave velocity with soil clay contents, at different degree of dryness	78

Figure 51: Variation of P-wave velocity with soil cement contents, at time of curing	80
Figure 52: Variation of P-wave velocity with soil cement contents, at time of curing	81
Figure 53: Variation of P-wave velocity with water contents, at different cement content percent	81
Figure 54: Distribution of geophones and accelerometers on the scaled model strip footing	82
Figure 55: Variation of wave velocity at different locations under strip footing at different vertical stresses.....	85
Figure 56: Variation of wave velocity with vertical stresses at different locations under strip footing.....	87
Figure 57: Comparison between variation of wave velocity V_2 and V_5 measured with geophones and accelerometers with the applied vertical stresses.....	88
Figure 58: Example acceleration responses (sender and receiver) at side hit.....	89
Figure 59: Locations of different nodes where geophones are inserted	90
Figure 60: Variation of wave velocity at different top surface locations with vertical stresses	90
Figure 61: Variation of wave velocity at different locations of depth $d = B$ from the surface with vertical stresses.....	91
Figure 62: Variation of wave velocity at different locations of depth $d = 2B$ from the surface with vertical stresses.....	91
Figure 63: Variation of wave velocity a depths $d = 0, B,$ and $2B$ from the backfill surface with vertical stresses.....	92
Figure 64: Variation of percentage increase in wave velocity a depths $d = 0, B,$ and $2B$ from the backfill surface with vertical stresses.....	95
Figure 65: Variation of stress calculated using Equation (4.9) at different locations with the applied vertical stresses.....	95
Figure 66: Variation of stress ratio versus velocity ratio	97

List of Tables

Table 1: Backfill soil specific gravity results	41
Table 2: Results of sensitivity analysis	46
Table 3: Soil samples tested in index test and the parameters changed.....	55

Chapter 1: Introduction

1.1. General

The design of any structure that will be built in direct contact with the soil usually starts with subsoil investigation process. The result of this process is usually a geotechnical report that incorporates different soil properties necessary for completing the structure design. The subsoil geotechnical report includes a comprehensive evaluation of geotechnical parameters, main recommendations for foundation design, and major inputs for analytical and numerical analysis. The recommendations and conclusions of the geotechnical report are mainly based on a series of laboratory and field tests that are designed and standardized to measure different soil properties. These tests are generally tended to be costly and time-consuming, which in turn adds to the overall project budget and construction time. Examples of field tests that usually one or two are conducted for structures are: Standard Penetration Test (SPT), Cone Penetration Test (CPT), Vane Shear test (VST), Pressure-meter Test (PMT), Flat-Plate Dilatometer (FPD), or Plate Load Test (PLT). In addition to being costly and time consuming, the results of field and laboratory tests are usually interpreted based on correlation equations that may render results with 100% difference [1][2]. Furthermore, most of the field tests require borehole loges in order to conduct the test at different depths and to collect disturbed and undisturbed samples for the lab tests, which adds to the cost.

On the other hand, laboratory tests need highly skilled technicians and are conducted on soil specimens that are either collected from the field, “undisturbed samples”, or reconstituted samples. These samples are usually subjected to certain degree of disturbance during drilling and sampling process [3]. Furthermore, in highly variable and anisotropic soil, these samples might not be representatives of the full soil domain. Therefore, tests conducted using these samples may not represent the real soils that samples are extracted from. Other disadvantages of these tests include test duration which is too lengthy and very expensive, especially for time consuming, high tech tests.

To eliminate disadvantages and limitations of both field and lab tests discussed earlier, nondestructive, non-invasive techniques have been developed and incorporated in soil investigation. Geophysical Technique (GT) is one of the

nondestructive tests that are employed to determine the stiffness properties of the soil. This technique relies on the measured body wave velocity in order to determine the soil stiffness. The main objective of this research is to adapt the Geophysical Technique (GT) facilities that are available at the AUS in predicting the variation of soil stiffness with different soil properties. In addition, the same technique is used to measure the variation of the body wave velocity under shallow foundation. This allows for the measurement of soil stiffness under large applied stress from strip footing.

1.2. Problem Statement

A review of the current state of practice with respect to measurement and variation of soil stiffness reveals that fewer studies have considered the correlation between the wave velocity in soil and the stress applied from shallow foundation. In addition, Bender Element that is commonly used for wave measurement in soil due to its simplicity and relatively low cost was reported to be unsuitable for undisturbed or cemented materials [4][5]. This is because Bender Element is always inserted into the soil specimen which may cause significant disturbance in the vicinity of the inserted element. This disturbance might affect the wave transmitted from one side to the other side of the soil specimen, which in turn might affect the measured velocity and soil stiffness. Therefore, the surface flat shape or disk transducer can be applied to various types of specimens, including stiff or cemented materials, with relative ease, and no disturbance effect. A disk transducer usually measures the compression wave (P-wave) velocity. However, it can also be used simultaneously to measure shear waves in an identical specimen, as opposite to the Bender Element which is generally used to measure only shear wave velocity. Based on the review of the current practice, the following points are relevant to the objectives of this thesis:

- There is a lack of laboratory studies required for establishing relations between the physical properties of the soils and their seismic properties, especially at low pressures which is equivalent to these shallow depths.

- The effects of soil formation, degree of saturation, water content, void ratio, cementitious material, and compaction on seismic (P- and S-wave) properties of soils are largely unknown.
- Interpretation of seismic data at shallow depth (i.e., small overburden pressure) requires measuring the P-wave and, to a lesser extent, S-wave propagation at low pressures; however, most available measurement lack information about P-wave which is crucial for field seismic interpretation [6].

In addition, it is noted that P-wave laboratory data collected for soils at low-pressure conditions appropriate to the near surface are sparse in the literature and information about both compressional and shear wave velocity measurements as a function of pressure at the extremely low pressures representing the shallow subsurface is required. A research strategy to meet this goal is to develop laboratory experiments involving the measurement of P-wave velocity at low pressures in compacted soil specimens. Therefore, a simple, easy to use, and cost efficient setup is developed in order to measure P-wave velocity in different sandy soil specimens with different properties. In designing this setup, the shortcomings of Bender Element were avoided to the best way possible.

1.3. Research Objectives

Based on the problem statement explained above, the current study aims to achieve the following objectives:

1. Develop a laboratory setup that is capable of making accurate measurements of P-wave velocity in soil specimens at different soil conditions and properties, and at low confining pressure.
2. Conduct a sensitivity analysis to select the setup dimensions that fulfill the requirements of wave length and wave propagation through soil specimens.
3. Use the developed experimental setup to quantify the variation of P-wave velocity with different soil properties; for example, dry density, void ratio and different soil gradation, water content, clay content, and cement content.

4. Develop and construct model test setup for a strip footing on sandy soil that instrumented with accelerometers and geophones to measure both soil bearing capacity and wave velocity at different stress increments.
5. Develop a P-wave velocity-bearing stress equation for shallow foundation that can be used alternatively to either predict stress at known velocity, or to predict velocity at known stress.

1.4. Significance of the Research

The significance of the current research work could be summarized in the following points:

1. This research belongs to nondestructive testing techniques which are considered a new research trend emerging in the area of geotechnical engineering.
2. It is the first time to measure the P-wave velocity in soil using this simple, yet easy technique that relays mainly on the fundamentals of wave propagation on soil mass.
3. This research is unique as it uses the geophysical instrumentations at different depths under strip footing although they are always practically used at the ground surface.
4. The implementation of geophones together with accelerometers to measure P-wave velocity under strip footing adds to the reliability of the results of this research.
5. The experimental results obtained in this research allow for the development of empirical relationship that permits more accurate inversion of wave velocity to stress, and vice versa.

1.5. Thesis Organization

Chapter 2 summarizes the available literature related to research subject of wave velocity in soil and methods of measuring it. Fundamentals of geophysical techniques are presented first, and then relationships between wave velocity and bearing capacity are introduced. The types of failure under strip footing at ultimate load are also

discussed. Finally, the effect of moisture content, void ratio, and clay content in both P-wave and S-wave velocity is discussed.

Chapter 3 begins with a description of the material properties, and then it provides a detailed discussion of procedures used to determine these properties. The instrumentation used to measure the P-wave velocity in both index tests and strip footing model is described next. Sensitivity analysis that is conducted to select the index test dimensions and setup is also explained. In addition, scaled footing tests with description of the instrumentation are introduced in details. Finally, signal processing and interpretation for determining wave velocity are explained.

Chapter 4 presents and discusses the study results, starting with index test results. In addition, it introduces different effects of soil properties on measured wave velocity. Then, the strip footing test results are presented and discussed. The chapter ends with a useful velocity-stress relationship.

The last chapter, Chapter 5, summarizes the important findings and provides final conclusions and recommendations. Potential future studies on the subject are also suggested.

Chapter 2: Literature Review

2.1. General

Geotechnical geophysics is defined as the application of geophysics to geotechnical engineering problems; for example, investigations extended to a total depth of thousands of feet in some instances. There are several types of Geotechnical geophysical surveys, such as tests that are performed on the ground surface, within boreholes, and from the water and air. These methods, with the exception of seismic tomography, are primarily surface-based techniques. Moreover, the field of geotechnical geophysics is different from nondestructive testing.

According to Oyedele et al. [7], the geophysical and the geotechnical methods can be widely used in a number of areas, such as geotechnical investigations (e.g., Standard Penetration Test and Cone Penetration Test) that are carried out on the site, and geophysical techniques (e.g., Vertical Electrical Sounding) that are also implemented.

Moreover, according to Jamiolkowski [8], geophysical testing in geotechnical engineering is used for various reasons, such as measuring stiffness at small strain as obtainable from the (S and P) velocities, evaluation of void ratio and porosity from the measured S and P velocities, and using the S-wave velocity to evaluate the coarse grained soils susceptibility to cyclic liquefaction.

2.2. Geophysical Technique

Geophysical Technique uses the mechanical wave spread through the solid and its characteristic velocities in order to determine stiffness, damping, and different layers thicknesses. Stiffness (k) and damping (c) that are measured using the Geophysical Technique represent small strain response of the soil. Both S-wave and P-wave can be utilized in geotechnical site characterization in a multi-channel surface wave's analysis (MCSWA) technique. In this technique, a multiple number (usually twelve or more) of receivers (geophones) with a seismograph are used as shown in Figure 1. In this method, ground response is usually generated by using impulsive seismic source that is produced by a hammer. Recorded data in Figure 2a could be presented after the test to produce the dispersion curve in Figure 2b, which is used to produce the shear wave velocity profile as shown in Figure 2c.

In addition, seismic velocity profile can provide information on the variability beneath a certain site. Moreover, it allows for creating a qualitative assessment of the variability of soil properties, such as strength and stiffness. Features, such as fractures, voids, rock layers and soft spots, which are considerably difficult to detect using the conventional boring and drilling techniques, can be detected by the geophysical techniques. Geophysical techniques can be used also to provide values of the stiffness of the soil layers (G_0 or G_{max}) based on the shear wave velocity, and the soil bulk density (ρ) through the following equation:

$$G_0 = \rho V_s^2 \quad (2.1)$$

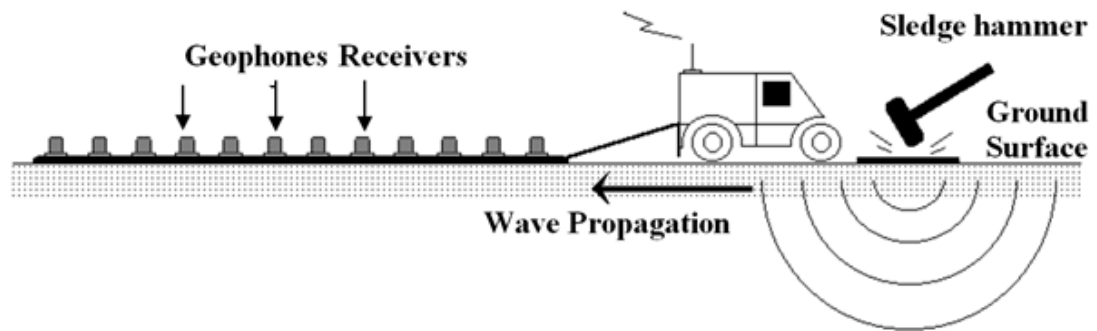


Figure 1: Multi-Channels Surface Wave Analysis (MCSWA) technique

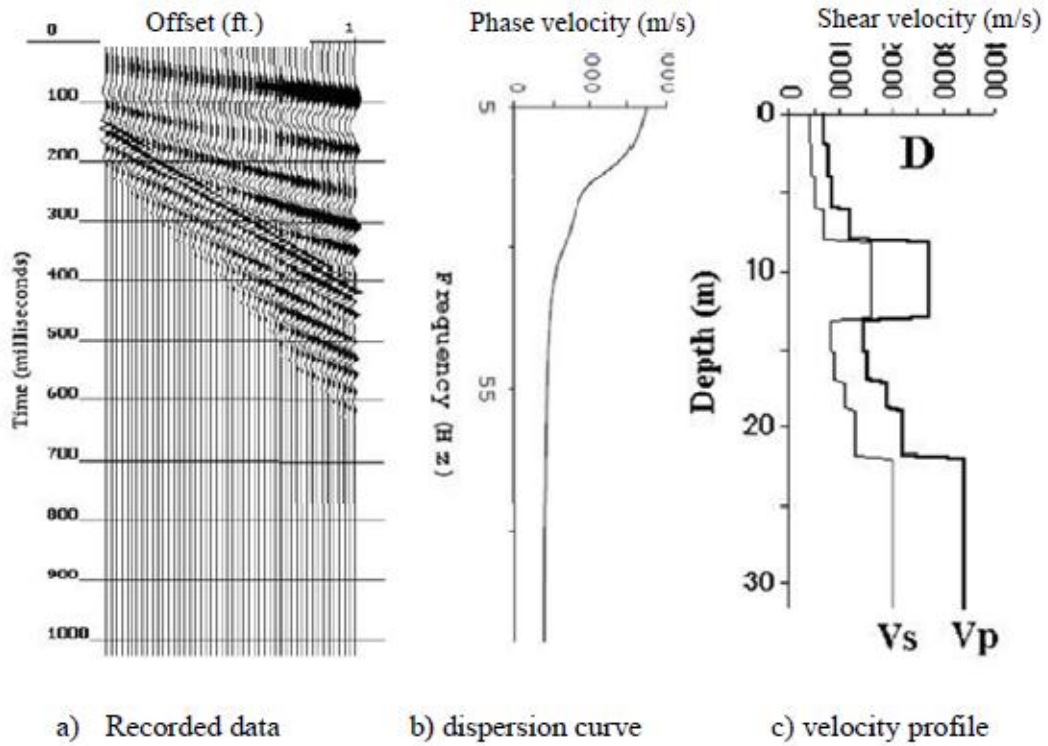


Figure 2: Example of recorded multi-channel data in MCSWA method and processing steps

Measuring the shear wave velocity in the site has an advantage of reflecting the true soil properties, such as void ratio, density, stress history, mean effective stress, shear strength, and geological ageing. Sirikarn [9] states that both P- and S-wave velocities increase with an increase in the soil density and effective stress and with the reduction in the soil porosity. As a result, the wave velocity increases as the depth below ground surface increases. Gardner et al. [10] suggest the following relationship between P-wave velocity (V_p) in m/s and density (ρ) in gm/cm^3 :

$$\rho = 0.31(V_p)^{\frac{1}{4}} \quad (2.2)$$

However, Dey and Stewart [11] state that there is a need of more information in the equation that is proposed by Gardner et al. [10]. In addition, Minsu and Gye-Chun [12] point out a relationship between the internal angle of friction and the shear wave velocity. However, they indicate that the void ratio (e), and the effective overburden pressure (σ_o) should be included in any equation that correlates soil

friction angle and wave velocity. In addition, they report 25% difference between values of friction angles predicted with shear wave velocity and those predicted using standard penetration test (SPT). In other words, the shear wave velocity underestimated the friction angle compared to SPT. The reason for this difference is attributed to the very small strain state in measuring V_s compared to the large strain in conducting SPT. Nonetheless, the researchers did not propose a clear and solid correlation equation relating soil friction angle (ϕ) and shear wave velocity (V_s).

According to Sirles [13], the geotechnical geophysical survey is often the most cost-effective method to obtain subsurface information over large study areas. It is generally used to select borehole locations and can provide information about the variability and nature of the subsurface between the existing boreholes. Other advantages of geotechnical geophysics are related to site accessibility, noninvasiveness, portability, and safety. Moreover, according to Jamiolkowski [8], geophysical testing in geotechnical engineering is used in various ways, such as measuring stiffness at small strain as obtainable from the (S and P) velocities, evaluation of void ratio and porosity from the measured S and P velocities, and using the S-wave velocity to evaluate the coarse grained soils susceptibility to cyclic liquefaction.

Moreover, Schulze [14] states that *“For the determination of allowable bearing pressure, the geophysical methods, utilizing seismic wave velocity measuring techniques with absolutely no disturbance of natural site conditions, may yield relatively more realistic results than those of the geotechnical methods, which are based primarily on borehole data and laboratory testing of so-called undisturbed soil samples.”* Since that time, numerous trials have been made to solve the geotechnical problems using the geophysical techniques. For example, the P-wave velocity was used to determine the unconfined compressive strength and the modulus of elasticity for different samples of soils (sand and rock). In addition, Hardin and Black [15] and Hardin and Drnevich [16], based on extensive experimental data, establish relations between the shear wave velocity, shear rigidity, and the void ratio of soils. Likewise, Ohkubo and Terasaki [17] provide various expressions trying to relate the seismic wave velocities to weight density, water content, permeability, modulus of elasticity, and the unconfined compressive strength.

2.3. Geophysical technique and bearing capacity

For the sake of rapid, cost effective determination of the soil bearing capacity, and to avoid the limitation of empirical equations that relate soil properties to shear wave velocity, a number of researchers suggest to directly relate the soil bearing capacity (q_u) to the wave velocity (V_s). Based on extensive site investigation, laboratory testing, and geophysical tests, Tezcan et al. [18] propose an empirical formula to correlate the allowable bearing capacity of shallow foundations in soils and rocks to the wave velocity and soil unit weight. The proposed equation takes the following form:

$$q_a = \frac{0.1(\gamma_o + 0.002V_{P1})V_{s2}}{n} \quad (2.3)$$

In the equation above, γ_o is the reference unit weight and is assumed to be 16 kN/m³ for loose, sandy and clayey soils, V_{P1} is the P-wave velocity for soil above the foundation level, V_{s2} is the S-wave velocity for soil below foundation level, and n is considered as a safety factor. However, Equation (2.3) has several assumptions and limitations that need to be clarified. For example, not only Equation (2.3) is driven based on modified Rankine's methods that are dated back to 1920, but also Tezcan and Ozdemir [19] build their equation based on the expression $q_u = \gamma D_f$. Comparing this expression with [21] (i.e., Equation (2.5)) indicates that Tezcan and Ozdemir neglect a number of highly significant terms; for instance, bearing capacity factors (N_q and N_γ), and most importantly they neglected the term $0.5\gamma BN_\gamma F_\gamma$'s which is called γ -term in the general bearing capacity equation. Finally, Tezcan and Ozdemir [19] measured shear velocity in-site at very small shear strain while they conducted plate load tests to measure q_u at large strains. This deficiency forced them to use several baseless assumptions, and to use n as a calibration factor, not as a safety factor.

Values of the allowable bearing pressures, q_a , estimated using conventional Terzaghi theory are shown in Figure 3. In the same figure, values of the P and S wave velocities have been measured *in situ*, right at the foundation level for the purpose of determining the allowable bearing pressures, q_a , using the method suggested in Equation (2.3). It is clear that, for V_s smaller than 400 m/s, the two methods predict closer and quite acceptable results. For V_s larger than 400 m/s, the proposed method

started to over predict the bearing capacity. In fact, Tezcan and Ozdemir [19] state that the conventional method fails to produce reliable and consistent results for relatively strong soils and soft rocks. This is attributed to the difficulty in determining the appropriate soil parameters c and ϕ for use in the ‘conventional’ method.

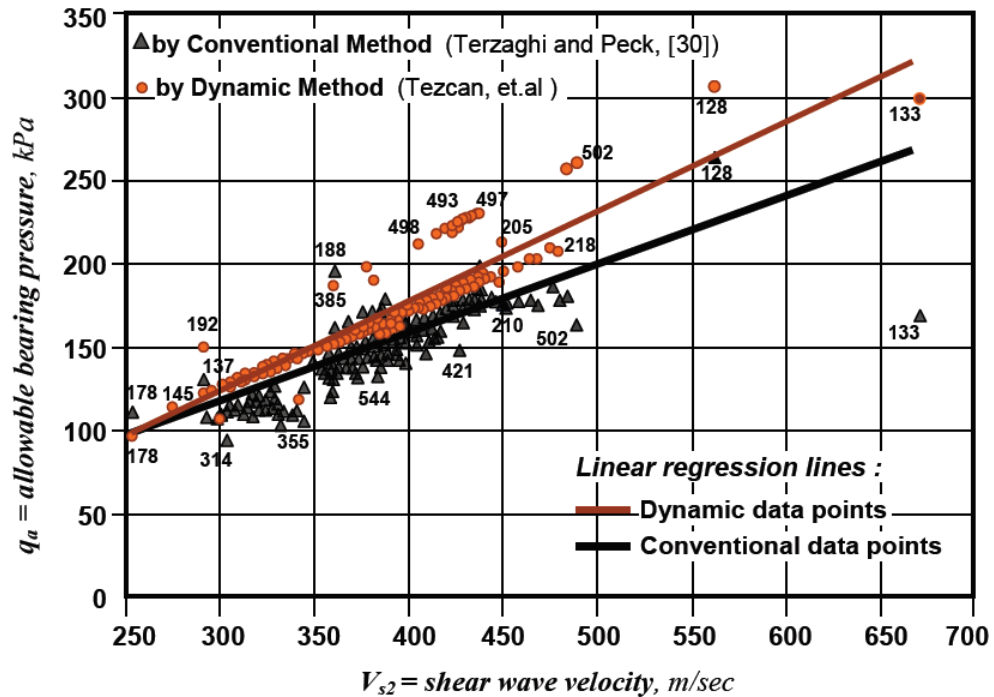


Figure 3: Comparative results of ‘Conventional’ and ‘Dynamic’ methods [19]

In addition, Joseph et al. [20] measured the P-wave and S-wave velocities using the seismic refraction survey in the city of Eket, Nigeria. Their work is extensively focused on finding mathematical relations between elastic parameters and seismic refraction velocities for the study area. Results show that the allowable bearing pressure increases when the shear modulus and shear wave velocity increase. Moreover, the relationship between the allowable bearing pressure and the shear modulus prove that the allowable bearing capacity increases with depth. In addition, the main goal of their study is to use the findings as a guide in the location of foundations. Moreover, free-free resonant column test was used for measuring shear modulus (G_{max}) and material damping (D_{min}) in laboratory for both soil and rock specimens. The advantage of free-free resonant device is that it allows measurements in a pressurized cell of sigma effective more than 80 KPa. Moreover, resonant column

test was used to find the relationship between shear modulus, material damping, and shear strain in both soil and rock. The relationship between the allowable bearing pressure and the shear modulus approve that the allowable bearing capacity increases with depth. The main goal of the study by Joseph et al. [20] is to use the findings as a guide in the location of foundations. The used procedure follows the equation below:

$$\text{Shear modulus, } \mu = \frac{\gamma V_s^2}{g} = \rho V_s^2 \quad (2.4)$$

where; $\gamma = \gamma_0 + 0.002 V_p$,

V_s and V_p are measured in the laboratory while doing the test,

$\gamma_0 = 16 \text{ KN/m}^3$ for loose sand and clayey soils,

Sub-grade coefficient and ultimate bearing capacity can be calculated respectively as:

$$K_s = 4 \gamma V_s, \quad \text{and } q_f = \frac{K_s}{40}$$

However, it should be noted that this method is only applicable for shallow foundations.

2.4. Bearing capacity wave relations

Measuring the shear wave velocity in the site has an advantage of reflecting the true soil properties, such as void ratio contributions, density, stress history, mean effective stress, shear strength, and geological ageing. Bearing capacity of a shallow foundation that is rested on a sandy soil depends on the soil friction angle, and soil bulk unit weight [21]. The relationship between the bearing capacity of a shallow foundation (q_u) with both (ϕ) and (γ) is as follows:

$$q_u = \gamma D_f N_q F_q^{'s} + \frac{1}{2} \gamma B N_\gamma F_\gamma^{'s} \quad (2.5)$$

where; D_f = foundation depth below ground surface,

N_q, N_γ = bearing capacity factors depends on ϕ ,

B = foundation width, and

F_q^s, F_γ^s = factors depend on depth of foundation, load inclination and foundation shape.

According to Narongsirikul [9], both P- and S-wave velocities increase with an increase in the soil density and effective stress, and with the reduction in the soil porosity. As a result, the wave velocity increases as the depth below ground surface increases. Shear wave velocity is the most powerful soil parameter, and it represents the family of geotechnical soil conditions; for example, compressive strength, void ratio, shear rigidity, and cohesion. Borehole tests and laboratory testing would no longer be needed if the shear wave velocity and the P-wave velocity are measured as correctly as possible, right under the foundation level. As a result, the allowable bearing pressures, the coefficient of sub-grade reaction, and the unit weight are determined by using relatively simple expressions. The most general form of the allowable bearing pressure, under the shallow foundations with depth H from the surface, is assumed to be compatible with the weight of the soil column above the foundation base, and it thus may be expressed as:

$$q_a = \frac{\gamma H}{n} \quad (2.6)$$

Where; γ = unit weight (kN/m³), n = factor of safety, and H = foundation depth.

H may be replaced by the product of V_s = shear wave velocity and the time parameter (T), as:

$$H = V_s T$$

This is substituted in equation (2.6) to yield:

$$q_a = \frac{\gamma V_s T}{n} \quad (2.7)$$

Free-free resonant column test system has several components, containing pressure cell, pressure system, vacuum system, accelerometers, rotary solenoid, function generator, and signal analyzer (oscilloscope). The procedure of free-free resonant column test starts with preparation of the specimen. For undisturbed specimens of cohesive soils and rocks, they can be placed in the membrane directly. In addition, for reconstitution specimens of cohesion less soils must be prepared in a mold and then subjected to pro vacuum during reconstitution and placement in

pressure cell. After the specimen is prepared and the pressure equilibrium is established, the test takes approximately one minute for each stress level.

Free-free resonant column test is considered as an alternative for the traditional fixed-free resonant column. One of the differences between them is that the coil magnet system used for fixed-free configuration is replaced by an expensive rotary solenoid that is very small and light, which can facilitate specimen handling and also reduce specimen damage. One of the most important advantages of the free-free resonant test is that energy leakage is reduced because the specimen is not fixed to a pedestal. Moreover, damping ratio may be measured more accurately than under fixed-free conditions.

Furthermore, seismic techniques can be used to determine the allowable bearing capacity for shallow foundation in both soils and rocks. Seismic techniques consists of only two soil parameters, the *in situ* measured shear wave velocity, and the unit weight of the soil. Moreover, the unit weight of the soil can also be measured using another empirical expression which is the P-wave velocity. Shear wave velocity and the P-wave velocity are measured *in situ* using an appropriate geophysical survey. In addition, sub-grade reaction (k) and other elasticity parameters can be measured also using these seismic techniques. Seismic techniques have several advantages; for example, saving cost and time.

Once the seismic wave velocities, V_p and V_s , are measured by geophysical means for a particular layer in the field, shear modulus G , oedometric modulus of elasticity E_c , modulus of elasticity E (Young's modulus), bulk modulus (K), and Poisson's ratio (ν) can be calculated using the following expressions. The shear modulus G and the oedometric modulus E_c are related to the shear and P-wave velocities by the following expressions, respectively:

$$G = \rho V_s^2 \tag{2.8}$$

$$E_c = \rho V_p^2 \tag{2.9}$$

Where ρ = mass density given by $\rho = \gamma/g$.

Extensive bore hole and laboratory testing of soil samples are no longer needed if the shear wave velocity and P-wave velocity are measured under the foundation level. After that, the allowable bearing capacity, the coefficient of sub-grade reaction of the soil (ks), elasticity parameters, as well as the approximate value of the unit weight using relatively simple empirical expressions are estimated. Determination of seismic velocities, elasticity modulus, and structural properties of soils are not sufficient to design engineering projects. Therefore, seismic wave velocities are used to define the soil pressure. In addition, density relation has been defined also in terms of seismic velocities.

2.5. Types of failure in sandy soil at ultimate load

Foundation is considered the lowest part of the structure, which transmits the structure loads to the soil that is underneath them. Foundation types are divided into two major parts: shallow foundations, and deep foundations (Piles). Figure 4 shows a shallow foundation with a width of B , located at a depth of D_f below the ground surface, and supported by a sandy layer of soil. If this foundation is subjected to a load (Q), the load per unit area is calculated as: $q = Q/A$, where q is the bearing capacity, and A is the area of the foundation. By increasing the load (Q), settlement (S) also increases. As the load (q) increases, failure occurs when q is equal to q_u , as shown in Figure 4. This is called a general shear failure, where q_u is the ultimate bearing capacity.

According to Vesil [22], natural failure of soils at the maximum loads depends on several factors; for instance, relative compressibility (density) and strength of the soil, the depth of the foundation (D_f) compared to the width of the foundation (B), and the width to length ratio (B/L) of the foundation. This is explained by Vesil [22] who conducted several laboratory tests on footing over sandy soils. The results of Vesil's [22] study are summarized in Figure 5. These include the effect of relative density of sand (Dr) and foundation depth (D_f) on the soil shear failure under shallow foundation. In Figure 5:

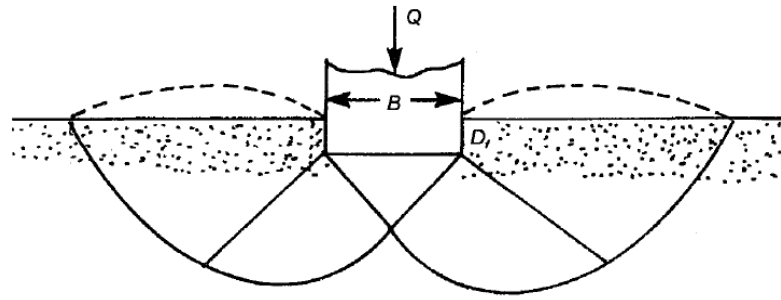
$$R = \frac{BL}{2(B+L)} \quad \text{For rectangular footing} \quad (2.10)$$

And

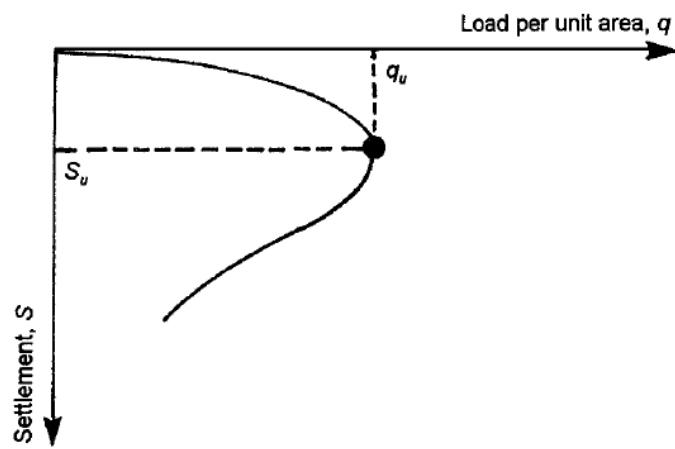
$$R = \frac{B}{4}$$

For a square foundation

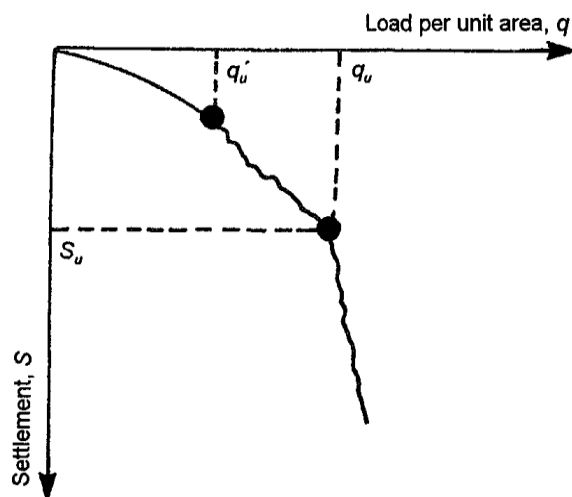
(2.11)



(a) General shear failure of soil under shallow foundation



(b) Bearing capacity versus vertical settlement of footing (General shear failure)



(c) Bearing capacity versus vertical settlement of footing (Local shear failure)

Figure 4: Shear failure in soil, and variation of bearing capacity with foundation settlement

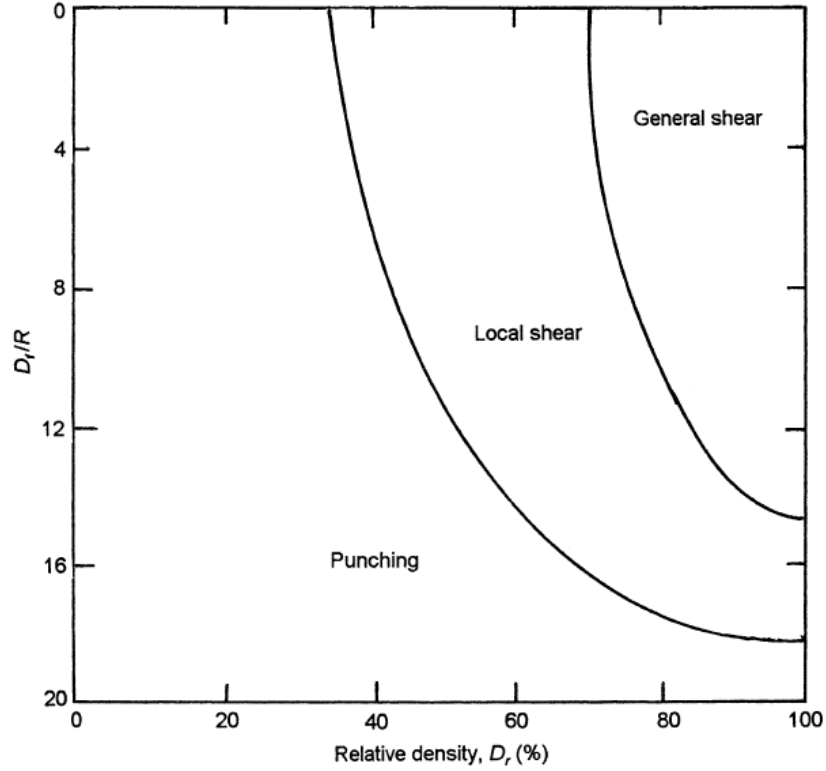


Figure 5: Nature of failure in soil with relative density of sand (D_r) and D_f/R [22]

2.6. Bearing capacity of shallow foundation

According to Terzaghi [23], the original relationship between bearing capacity of a shallow foundation (q_u) with both (ϕ) and (γ) is as follows:

$$q_u = \gamma D_f N_q + \frac{1}{2} \gamma B N_\gamma \quad (2.12)$$

Where, D_f = foundation depth below ground surface, B = foundation width, and N_q and N_γ = bearing capacity factors depending on the soil friction angle ϕ , and calculated as:

$$N_q = \frac{e^{2\left(\frac{3\pi}{4} - \frac{\phi}{2}\right) \tan \phi}}{2 \cos\left(45 + \frac{\phi}{2}\right)} \quad (2.13)$$

$$N_\gamma = \frac{1}{2} K_{\rho\gamma} \tan^2 \phi - \frac{\tan \phi}{2} \quad (2.14)$$

Krizek [24] gives empirical relations for Terzaghi's bearing capacity factors N_c , N_q , and N_γ that can relate the bearing capacity with the internal frictional angle of the soil. They are as follows:

$$N_q = \frac{40 + 5\phi}{40 - \phi}$$

$$N_\gamma = \frac{6\phi}{40 - \phi}$$

Thus, substituting the above equations yields to the following Equation (2.15):

$$q_u = \frac{(228 + 4.3\phi)c + (40 + 5\phi)q + 3\phi\gamma B}{40 - \phi} \quad (2.15)$$

Moreover, for foundations that are rectangular or circular in plan, a plane strain condition in the soil at ultimate load does not exist. Therefore, Terzaghi suggests the following relationships for circular and square foundations:

For circular footing

$$q_u = 1.3cN_c + qN_q + 0.3\gamma BN_\gamma \quad (2.16)$$

And for square footing

$$q_u = 1.3cN_c + qN_q + 0.4\gamma BN_\gamma \quad (2.17)$$

2.7. Settlement of Shallow foundation

According to Vesil [22], settlement of shallow foundations (S_u) depends on several factors and conducted laboratory tests on foundation at the surface of sandy soil (i.e. $D_f/B=0$). Results, shown in Figure 6, indicate that the vertical settlement of foundation decreases as the sand relative density (D_r) increases. In addition, the foundation dimensions show a significant effect on the foundation settlement.

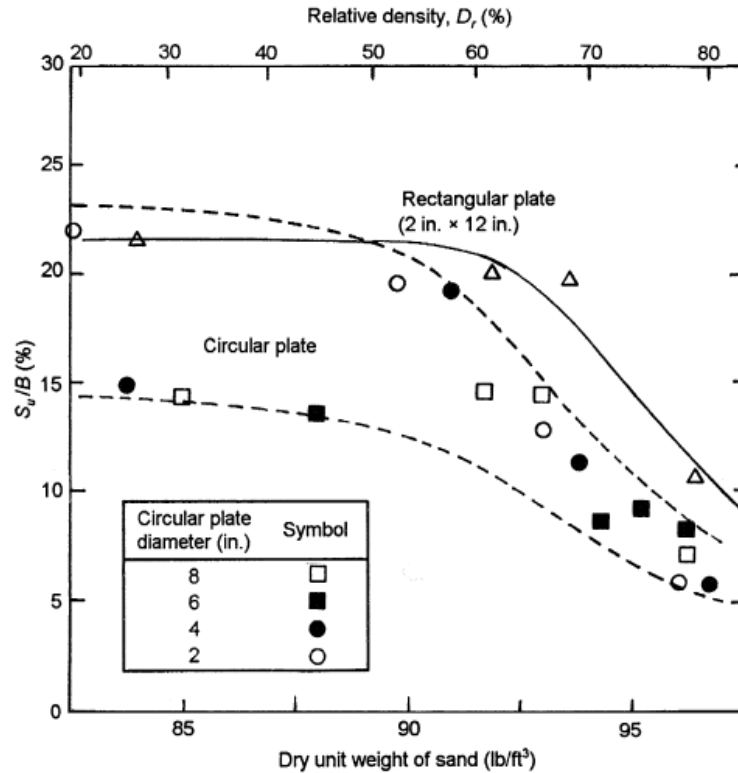


Figure 6: Variation of S_u/B for surface foundation (D_f/B) on sand [22]

In their study, Wicaksono et al. [25] prepared a test apparatus in the laboratory of the University of Tokyo in order to develop a study of wave measurements. They conducted two wave measurements methods, Trigger Accelerometer and Bender Element. Moreover, two types of sand were used, Toyoura Sand and Hime Gravel. Their goal was to determine the static and dynamic moduli. They also studied the effect of specimen size on both static and dynamic measurements. The researchers conclude that the function of Hardin and Richart, which was proposed in 1963, is the most appropriate among others for their type of sand. Figure 7 illustrates an example of measuring the time difference that was used later in order to measure the velocity. Moreover, the following equations show the procedure of measuring the static and dynamic moduli.

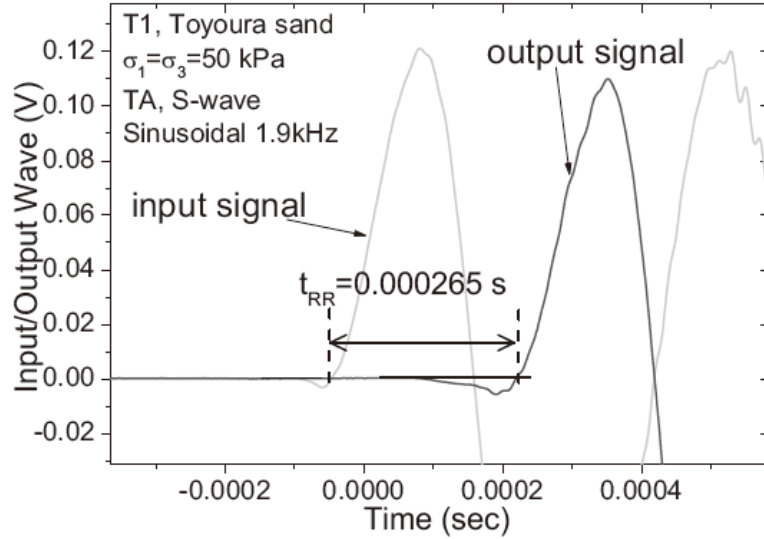


Figure 7: Evaluation of travel time [25]

$$V = \frac{d}{t} \quad (2.18)$$

where; d = the effective distance between the two sensors, and t = the time difference between input and output waves.

$$E_D = \rho \cdot V p^2 \quad (2.19)$$

$$G_D = \rho \cdot V s^2 \quad (2.20)$$

$$G_D = \frac{E_D}{2(1+\nu)} \quad (2.21)$$

$$G_{sta} = \frac{E_s}{2(1+\nu)} \quad (2.22)$$

Where; E_D = dynamic Young's modulus, E_s = static Young's modulus, G_D = dynamic shear modulus, and G_{sta} = statically measured shear moduli.

In a study conducted to measure the shear wave velocity in a granular soil using the discrete element method, the researchers [26] confirm that the shear wave velocity is a function of a number of soil parameters; for example, shape of the particles, elastic properties, gradation of the soil, void ratio, and boundary stress. They also state that measuring the effects of these soil parameters is difficult to be measured using the laboratory output results. Moreover, in order to determine an

accurate signal travel time, several factors should be taken into consideration; for instance, cross talk between the source of motion and the receiver, fabrication defects in the testing devices, system delay, and the electric and environmental noise. The study shows that the shear wave velocity can be calculated using the following equation:

$$V_S = \alpha \cdot \left(\frac{\sigma'}{1 \text{ kPa}} \right)^\beta \quad (2.23)$$

where α, β = fitting parameters, and σ' = effective confining stress in kPa.

Amaral et al. [4] conducted a set of laboratory tests in order to measure the elastic modulus and the damping ratio. Their study results were affected by the influence of experimental details, the analytical techniques used for data processing, and geometrical effects. Moreover, specimens used were made of cemented sand materials. In addition, compressional waves and longitudinal waves were generated on cylindrical specimens with a high frequency level of 20 to 70 kHz by using a designed interface. The following equations show the calculations of the compressional and shear wave velocities:

$$V_p = \left(\frac{E(1-\nu)}{\rho(1+\nu)(1-2\nu)} \right)^{\frac{1}{2}} = \left(\frac{M}{\rho} \right)^{\frac{1}{2}} \quad (2.24)$$

$$V_S = \left(\frac{E}{\rho 2(1+\nu)} \right)^{\frac{1}{2}} \left(\frac{G}{\rho} \right)^{\frac{1}{2}} \quad (2.25)$$

$$V_L = \left(\frac{E}{\rho} \right)^{\frac{1}{2}} \quad (2.26)$$

Where; ρ = the material mass density, E = Young's modulus, M = constrained modulus, G = shear modulus, and ν = Poisson's ratio.

A study by Zhang et al. [27] conducted at the Pennsylvania State University in order to study the influence of the sample size in measuring its velocity indicates that the sample area should be larger than the size of the transducer in order for the plane wave to hold. Moreover, the researchers confirm that the geometric requirement may not be easy to realize for some materials. In addition, the study results indicate that the phase velocity increases when the contact area decreased. The velocity can be calculated using the following equation:

$$v = 4204.5 \left(1 + 0.01916e^{-\frac{r}{0.4429}} \right) \quad (2.27)$$

$$v = 4662.5 \left(1 + 0.01352e^{-\frac{r}{0.4699}} \right) \text{ (Longitudinal Wave Velocity)} \quad (2.28)$$

where; $r = L/D=W/D$.

In the same vein, Heitor et al. [28] conducted a study at the University of Wollongong, Australia, in order to study the relationship between the shear wave velocity versus the moisture content and void ratio. A silty sand soil was used in their study. The study results show that when the moisture content increases, the shear wave velocity decreases. Similarly, when the void ratio increases the shear wave velocity decreases. Results of the study are shown in Figures 8 and 9.

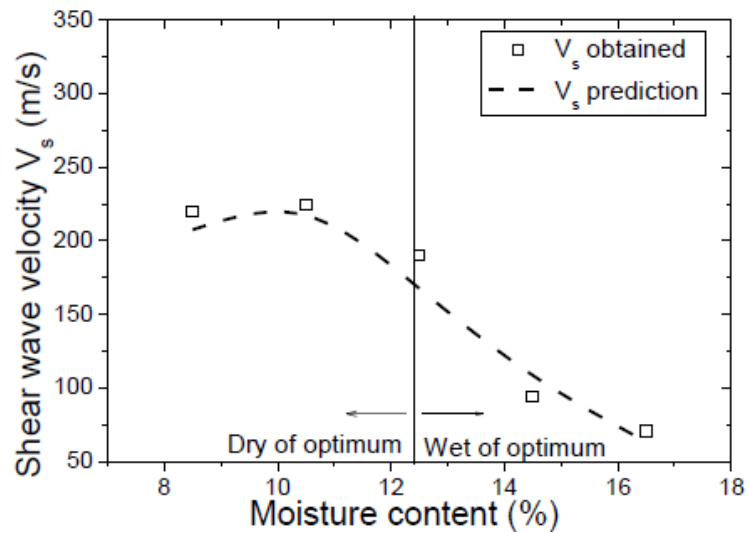


Figure 8: Shear wave velocities versus moisture content [29]

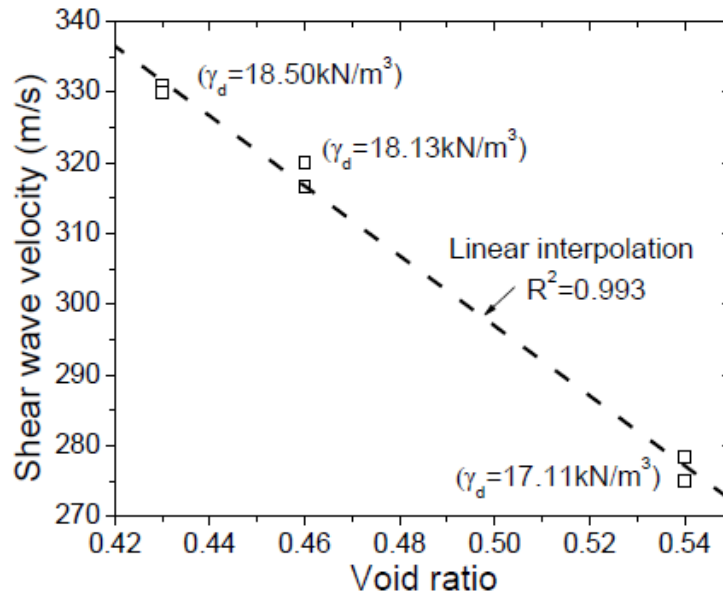


Figure 9: Shear wave velocities versus void ratio [28]

Another study by Bonner et al. [29] was conducted at the Technical University of Denmark to study the relationship between shear and compressional wave velocities with the percentage of clay content mixed with sand. The study shows that the shear and compressional wave velocities are very sensitive to the amount of clay added. The researchers conclude that the measured compressional wave velocity of the sand-clay mixture is not dependent on the clay content; nonetheless, it depends on the microstructure of the sand-clay mixture. Figure 10 shows the relationship between compressional velocities versus clay content.

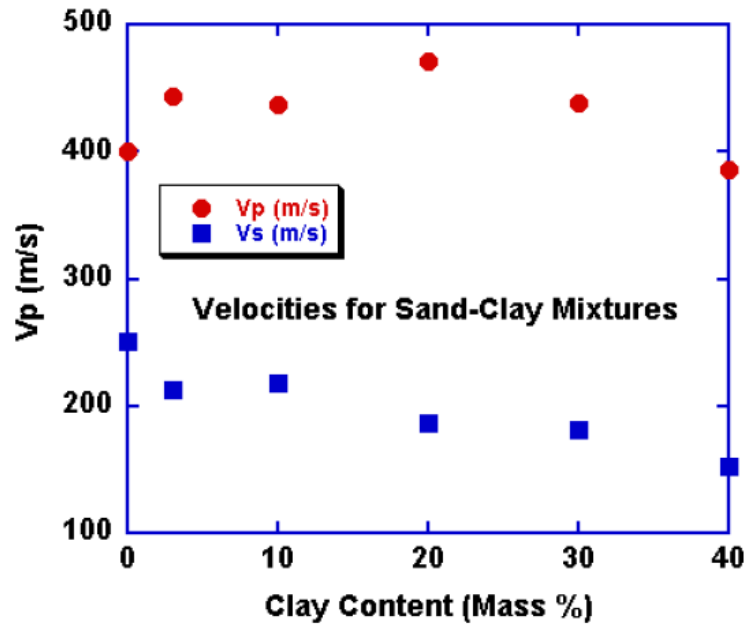


Figure 10: Velocity versus clay content for dry sand-clay mixtures [29]

A study by Indraratna et al. [30] was conducted at the University of Wollongong, Australia, in order to study the effect of compaction efforts on measuring the shear wave velocity of silty sand. The researchers prepared three samples with different compaction efforts: reduced energy, standard energy, and enhanced energy. They measured the shear wave velocity of the three samples at different timings of heating. This was in order to study the relationship between the shear wave velocity and the moisture content. Their study results are shown in Figure 11.

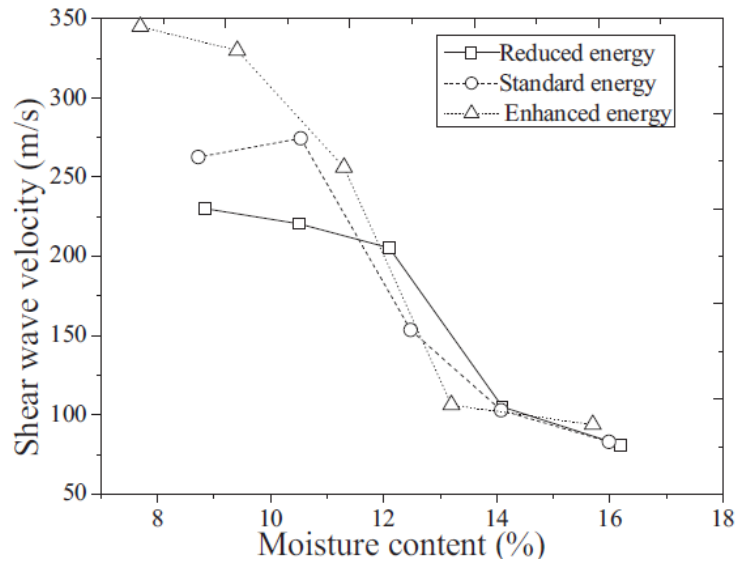


Figure 11: Shear wave velocity versus moisture content obtained for different compaction efforts [30]

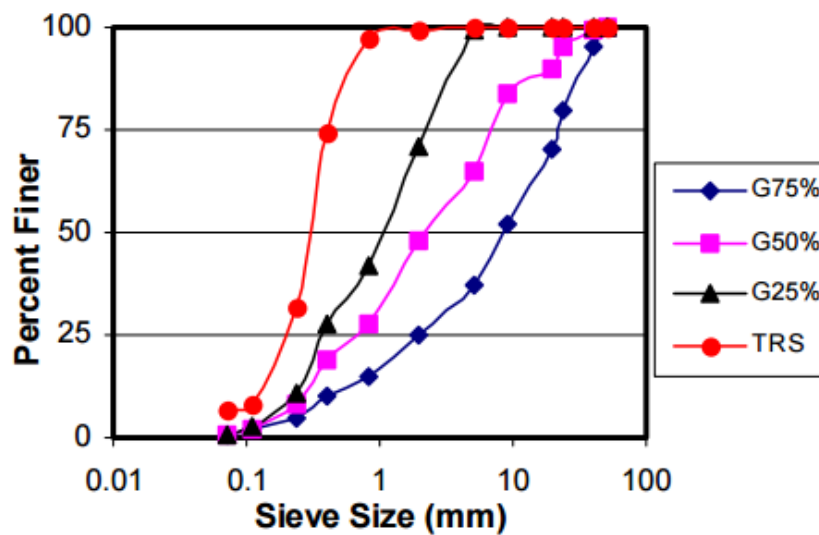


Figure 12: Grain size data, sand-gravel mixes [31]

In a study conducted in Buffalo, New York, United States of America, in order to study the effect of grain size of the soil on measuring the shear wave velocity and other dynamic and static characteristics, Thevanayagam et al. [31] used a silty soil as a reference sample, and then they started adding gravel to the original soil. They prepared four samples of gravel content of 75%, 50%, 25%, and 0%. Figures 12 and 13 show the grain size distributions that used and the final results of the study.

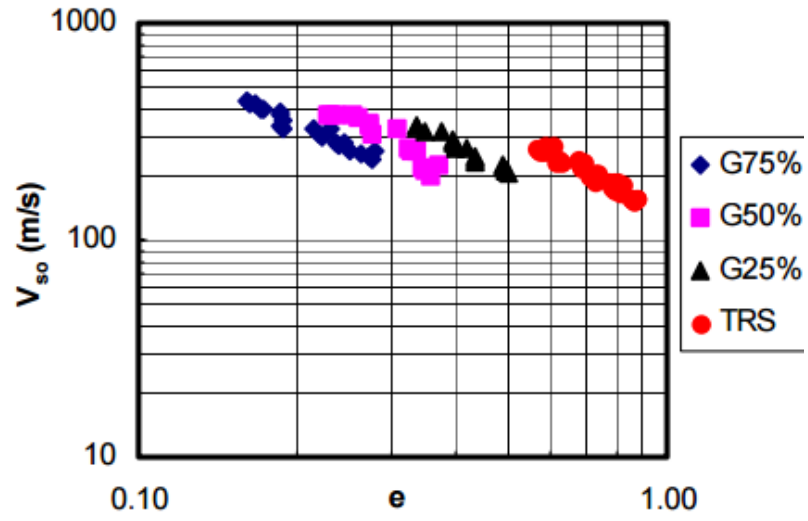


Figure 13: Influence of gravel content on shear wave velocity [31]

Chapter 3: Experimental Work

3.1. General

The current research was conducted in the Geotechnical Laboratory of the College of Engineering at the American University of Sharjah (AUS), United Arab Emirates. The Laboratory is well-equipped with the test set-up and all necessary instrumentations needed to perform the research study. The study is composed of 13 small scaled index tests, and two large scale strip footing models. The objective of the small scale models is to study the variation of the shear wave velocity with different soil parameters. Soil properties that are of high importance to the wave velocity are compaction efforts (void ratio, density, prosody), water content, soil grading size, soil clay content, and the addition of Portland cement. On the other hand, the objective of the two large scaled strip footing models is to develop a test setup that can measure the variation of the shear wave velocity with applied pressure on soil.

A preliminary sensitivity study was conducted using a number of index tests in order to come up with a final test set-up that can be used for all index tests. The main purpose of the sensitivity analysis, at the early stage of the project, is to choose the right boundary conditions, right material type, and right dimensions of the test set-up. Moreover, one large scaled model test was conducted in order to test the response of geophones, accelerometers, and other instrumentations that are used in this research. All experimental tests are explained and discussed in details in this chapter.

3.2. Soil Properties

At early stage of this research, the original sand obtained from Ras Al-Khaima (RAK), UAE, was used as is in the small index test set-up. However, it was found out that the larger particles of the soil (i.e., particles larger than 2 mm diameter) start to fall down from the ends of tested molds. In addition, it was difficult to attach accelerometer plates to the ends of samples constructed with RAK original sand. Therefore, RAK sand was used after passing from 2 mm sieve size which makes it remain inside the molds, and the particles of the soil remain in contact to each other. A number of soil tests were conducted, according to ASTM standards, in the Geotechnical Laboratory at the AUS to determine the geotechnical properties of the

sand used. Soil properties tests include sieve analysis, modified proctor test, specific gravity, and plasticity index test.

Sieve analysis was conducted according to ASTM C 136-14 standards in order to find out the grain size distribution curve for the sandy soil that was used in all lab tests. The particle size distribution curve for the backfill sand is shown in Figure 14. The soil is classified as well-graded sand (SW) with about 4% fines according to the Unified Soil Classification System (USCS). The value of the coefficient of curvature (C_c) is 2, and the value of uniformity coefficient (C_u) is 8. Modified sand from original RAK sand was obtained by passing the sand through 2 mm sieve. The grain size distribution of this sand is shown in Figure 14. The sand is classified as poorly graded sand (SP) with about 1% fines according to the Unified Soil Classification System (USCS). The value of the coefficient of curvature (C_c) is 1, and the value of uniformity coefficient (C_u) is 4.3.

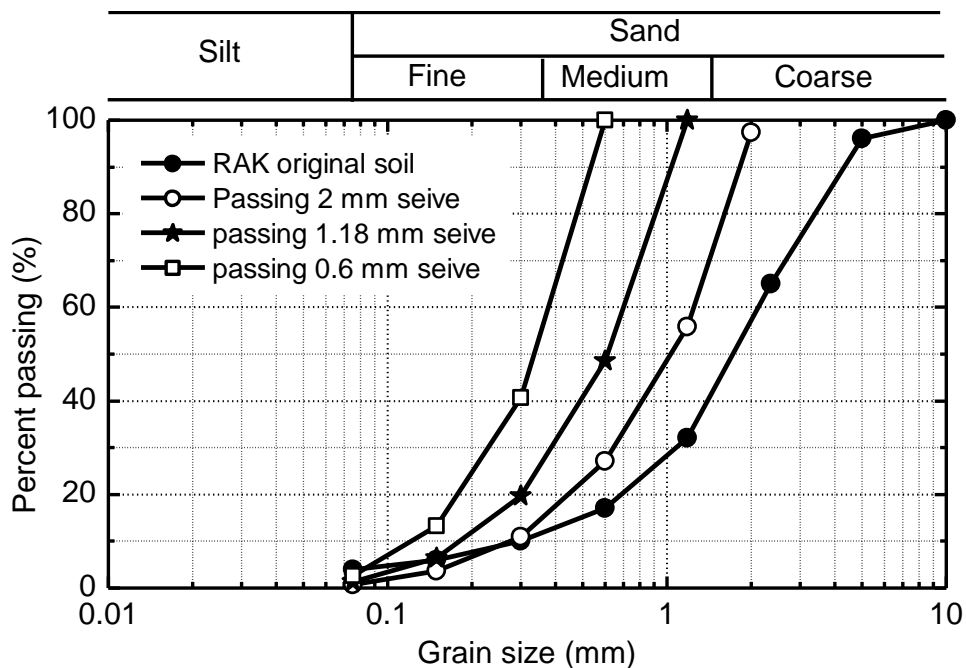


Figure 14: gradation for RAK original sand and fine sand passing 2mm sieve

Specific gravity test was conducted according to ASTM D854-14 in order to find the specific gravity of the sandy soil particles which will be used later in several calculations, such as void ratio, degree of saturation, porosity, and others. The specific

gravity of the sandy soil was found to be $G_s = 2.71$. Detailed results of the specific gravity tests are shown in Table 1.

Table 1: Backfill soil specific gravity results

Determination No	Trial 1	Trial 2
M_p (g)	125.61	125.53
M_{pwc} (g)	621	622.07
T_c	24.5	21
K_c	0.9973	0.99799
M_{pwst} (g)	690.7	710.04
T_t	24	21
$M_{pwt} = M_p + (V_p \times K_c)$ (g)	621	622.07
M_s (g)	109.75	139.39
K_t	0.99909	0.99799
$G_{s@20^{\circ}c} = \frac{K_t \times M_s}{M_{pwt} - (M_{pwst} - M_s)}$	2.73	2.71

A modified proctor test was conducted in accordance with ASTM D1557 in order to determine the maximum dry density ($\gamma_{dry-max}$) and the optimum water content (O.M.C) of the sandy soil. The maximum dry density is be used as a reference for the compaction stage that is needed to compact the soil used in the steel sand box (setup_1). Controlling the compaction stage is needed to ensure the repeatability of the test and to be able to control the unit weight at different tests. It is also expected that the density acts as a major factor that affects wave velocities and the electromagnetic wave propagation through the soils. Modified proctor tests were done at different water content percentages of 2%, 4%, 6%, 8%, and 10%. Figure 15 shows the maximum dry unit weight and the optimum water content for both RAK original and modified sand soil. It can be seen that the maximum dry unit weight $\gamma_{dry-max}$ and optimum water content O.W.C for Original RAK sand are 17.7 kN/m³ and 6%, respectively. However, the maximum dry unit weight $\gamma_{dry-max}$ and optimum water content O.W.C for modified RAK sand are 19.9 kN/m³ and 7.6%, respectively. It can be seen that as the sand becomes finer, the maximum dry unit weight and optimum water content increase.

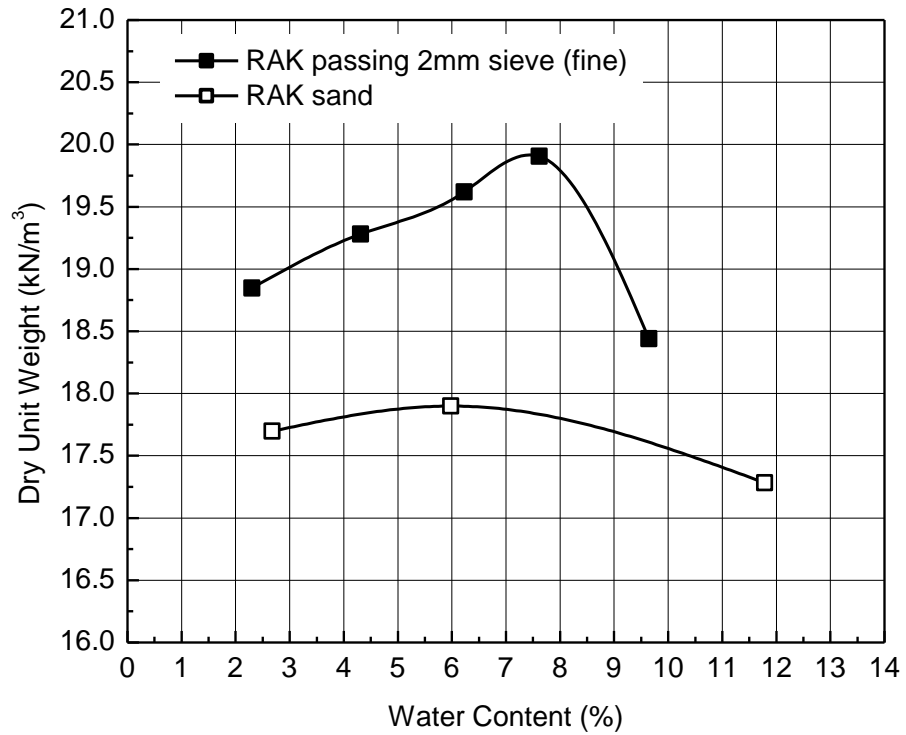


Figure 15: Dry unit weight versus water content (%)

Direct shear test was conducted in order to measure the shear strength parameters and volume change of sandy soil. For typical sand, shear strength is controlled by the internal angle of friction (ϕ), and the volume change is controlled by the dilation angle (ψ). Surface roughness, gradation, and soil density are considered to be other soil properties that affect the friction angle and the dilation angle. Results of direct shear tests are presented in Figure 16. Results indicate that the angle of internal friction of the RAK original sand used as backfill is $\phi = 49^\circ$. The angle of internal friction is found to be greater than 38° , conforming to the Unified Soil Classification System about well-graded Sand.

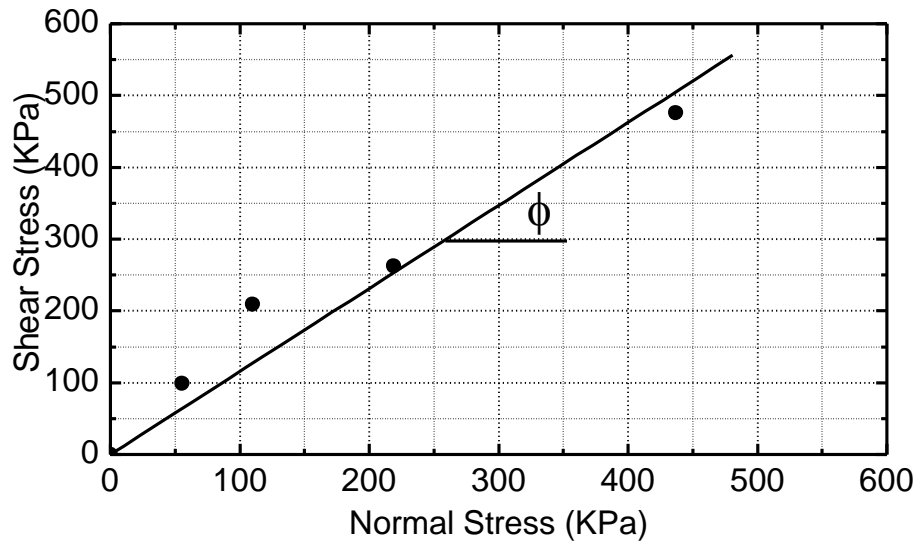


Figure 16: Direct shear test results for RAK sand

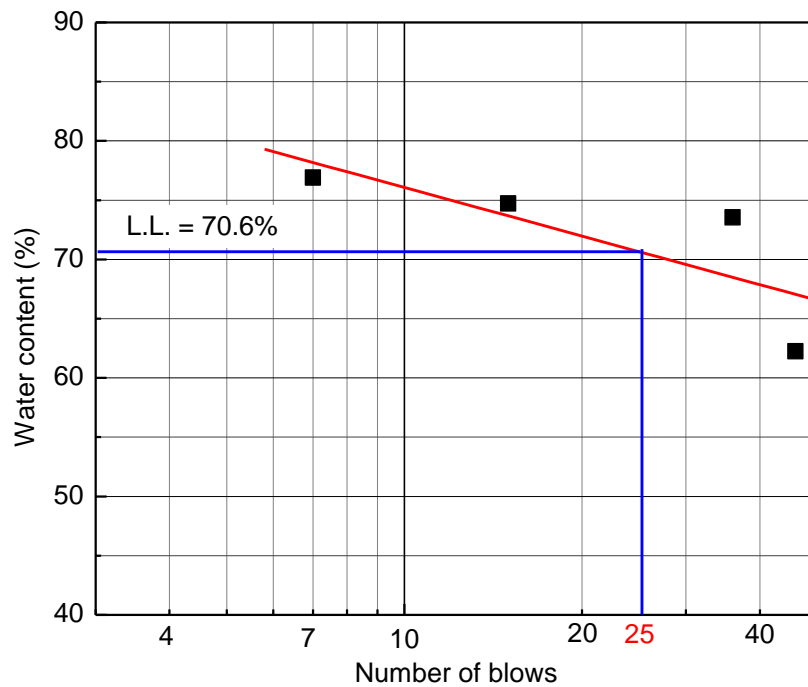


Figure 17: Liquid limit test for the clay soil

Plasticity index test was conducted in order to find the liquid limit, plastic limit, and the plasticity index of the clay which is added later to the sandy soil in order to investigate the effect of clay content percent on the shear wave velocity. The test results are shown in Figure 17. Results indicate that liquid limit L.L. = 70%, plastic limit P.L. = 46%, and plasticity index P.I. = 24%.

3.3. Accelerometers and Pico Scope

The accelerometers used in this study are miniature accelerometers produced by DYRTAN Instruments, Inc., model 3006A with a 12 g weight each, and 0.5 cm by 0.8 cm diameter and height. The accelerometers have + 50 g acceleration range, and 0.3 Hz to 5 kHz frequency range with a high resonant of 35 kHz. Figure 18 shows two of these accelerometers imbedded in the sandy soil. A line powered, 4 channel, 2-20 mA adjustable current, BNC connectors, 230VAV external Power supply was used to excite the accelerometers. The accelerometers output signals have been recorded using a two-channel Pico Scope produced by Pictech, which was connected to fast computer through a USP. Figure 19 shows the Pico Scope used in this study.

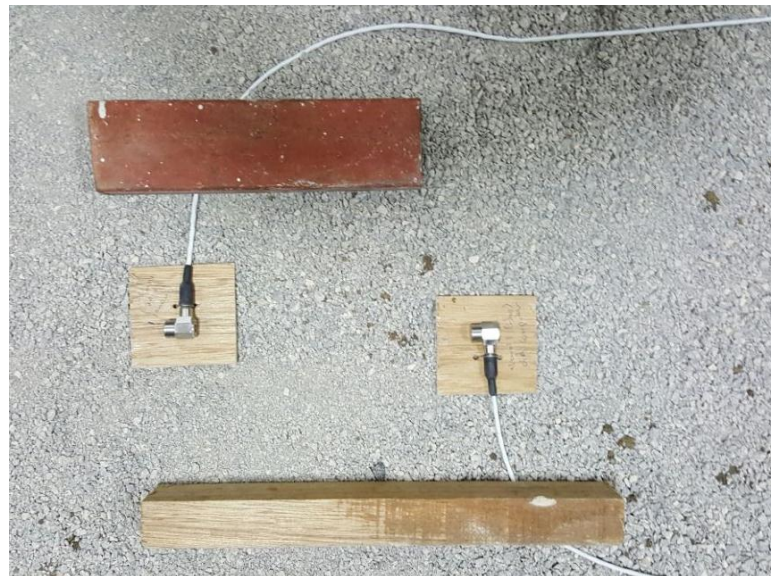


Figure 18: Accelerometers used in the current investigation



Figure 19: Pico Scope used for recording accelerometers output signals

3.4. Sensitivity Analysis

A number of index tests have been conducted in order to come up with a final index test set-up that can be used for all index tests of the soil. A major objective of the sensitivity analysis is to select the right boundary conditions, and proper dimensions of the small index test set-up. Table 2 summaries results of the sensitivity analysis; it indicates the effect of specimen different length, diameter, and different compaction efforts. Sample 5 has a length of 11.5 cm and a diameter of 4 in, sample 6 has a length of 17.3 cm and a diameter of 4 in (see Figure 20c), and sample 7 has a length of 12.5 cm and a diameter of 6 in (see Figures 20a and 20b). All samples were compacted with same compaction effort of 8 blows/layer for 3 layers, and 6% water content was used for all samples. In addition, one sample was tested without the PVC mold in an effort to isolate the effect of the mold on the measured shear velocity (see Figure 20a).

Table 2: Results of sensitivity analysis

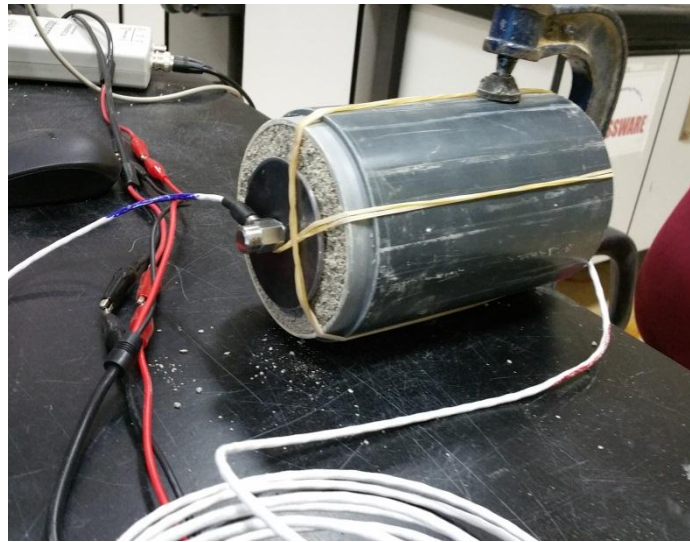
Parameter	Sample 5	Sample 6	Sample 7
L (cm)	11.5	17.3	12.5
D (cm)	10	10	15
Compaction Effort	3 layers / 8 blows	3 layers / 8 blows	3 layers / 8 blows
V₁ (Large 1) (m/s)	292.6	352	181
V₂ (Large 2) (m/s)	311.5	309.3	189.4
V₃ (Small 1) (m/s)	355	1739	244
V₄ (Small 2) (m/s)	347	297	245
F₁₁ (Large 1) (Hz)	1335	1144	953
F₁₁ (Large 2) (Hz)	1335	1144	1525
F₁₁ (Small 1) (Hz)	1526	763	381
F₁₁ (Small 2) (Hz)	381	763	381
λ (Large 1) (m)	0.22	0.31	0.19
λ (Large 2) (m)	0.23	0.27	0.12
λ (Small 1) (m)	0.23	2.28	0.64
λ (Small 2) (m)	0.91	0.39	0.64



(a) Sample with no PVC mold diameter



b) Sample with PVC mold and large diameter



c) Sample with small diameter and PVC mold

Figure 20: Compacted sandy soil samples with different dimensions and different boundary conditions

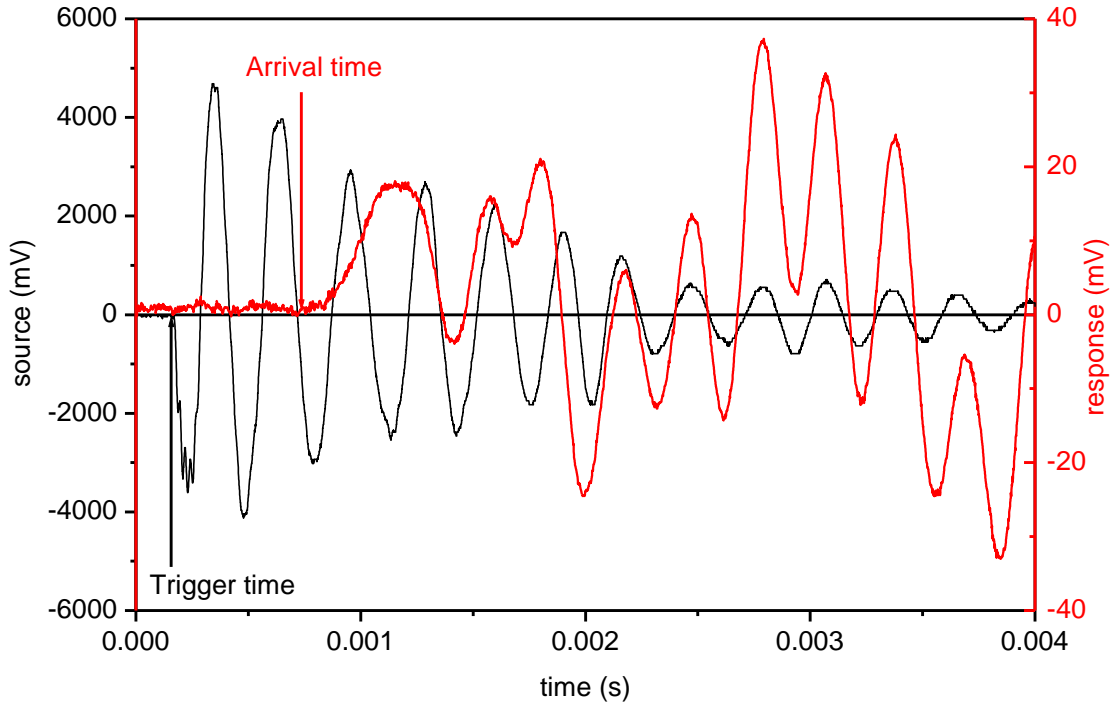


Figure 21: Example of generated and received waves at both sides of the soil specimen

Waves were triggered by lightly hitting one of the accelerometers attached to the side of the sample (Figure 20b), and hence this accelerometer is denoted as source. Then, the waves that arrived to the other side of the sample were received and recorded by a second accelerometer which is called a receiver. Figure 21 shows a typical example of generated and received waves recorded with the two accelerometers. Velocity was calculated by dividing length of the specimen by the time captured with the two accelerometers attached with the specimens at both sides. f_{11} is first phase frequency in Hz at 70% of the maximum magnitude, calculated from the Fast Fourier Transformation (FFT) of the received signals. Parameter λ is the wavelength in meters, which can be calculated using Equation 3.1[32] as follows:

$$\lambda = \frac{v}{f_{11}} \quad (3.1)$$

Knowing the Wavelength (λ) is needed in this study to ensure that the wavelength is less than half of the total sample length. In other words, this will help ensuring that one full wave or more can travel through the sample length before it is

received by the accelerometer on the other side (receiver). Moreover, the near field distance (Length of zone) was calculated using Equation 3.2 [32] as follows:

$$NF = \frac{D^2}{4\lambda} \quad (3.2)$$

Where D is the specimen diameter and λ is the wavelength. Near field distance was measured in order to ensure that it is less than the radius of the specimen. In other words, to make sure that the waves are not interfering with the PVC cylindrical boundary of the specimen, the near field value NF should be less than the specimen radius. An average value of NF for typical specimen with $D = 15$ cm and wave length $\lambda = 0.4$ m is calculated as $NF = 0.024$ m, which is much less than the radius of the specimen ($r = 0.075$ m).

To increase the contact between the accelerometer base and the sides of the sand specimen, a steel base plate was attached to each accelerometer base as shown in Figure 22. Different diameters of the base plate have been investigated to isolate its effect on the measured wave velocity, and a plate with 5 cm diameter was found to be suitable for good accelerometer connectivity with minimal effect on the measured wave velocity. It is found that the circular steel plate should not be very small to penetrate the soil, and not very large to interfere with the PVC boundary.

Another factor that was investigated during this sensitivity analysis is how the soil specimens will be positioned during the tests. Different positions have been tried; for instance, putting the sample free of any connectivity on the disk, as shown in Figure 5c. Another position was to connect the sample firmly to the disk in an effort to prevent the free vibration mode, as shown in Figure 23.

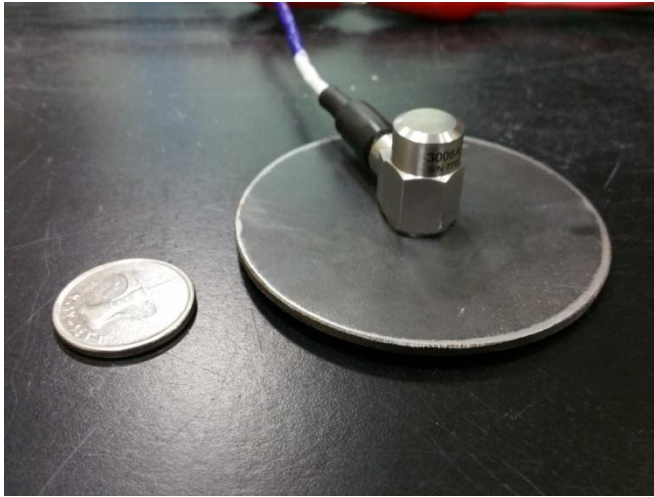


Figure 22: Steel plate attached to accelerometer base “base plate”



Figure 23: Clamping the soil specimen to a rigid table

After the sensitivity analysis, a 6-in diameter sample was selected to be used in this study. This selection was made according to three main reasons. First, a 6-in diameter is the standard size for the CBR test and the modified proctor test. Second, these dimensions (i.e., diameter and length) are in accordance with the wavelength equation and the near field effect calculated previously. Third, the larger diameter of a mold reduces the wave reflection from the PVC boundaries to the end of the sample where the accelerometers are attached. In addition to careful selection of the sample size, a PVC mold was selected to be the right material for all up-coming tests.

Moreover, accelerometer’s connectivity to the samples is an important factor on the measured wave velocity. As mentioned earlier, two accelerometers were

attached to the sample ends by using a group of rubber bands. Moreover, each accelerometer was attached to a circular steel plate to ensure that the accelerometers are well attached to the sample, and axis of motion is well aligned with the axis of the cylindrical specimen. It is found that the axis of accelerometers cannot be adjusted if they are attached directly to the specimen without base plates, which works as a base for the accelerometers to perfectly rest on the sample sides.

Ways of holding the sample are also studied in order to ensure that it doesn't affect the results. This impact can be due to the free vibration of the sample while triggering the source pulses. This free vibration might generate additional noises in the recorded pulses. Furthermore, the sample was rested on a flexible surface as well as a rigid surface to check if there is any change in the measured records. The sample was attached firmly to the rigid surface using steel clips (see Figure 23) in order to compare the results of all mentioned different conditions. It is found that all mentioned conditions do not have an impact on the results. The final testing set-up is shown in Figure 24.

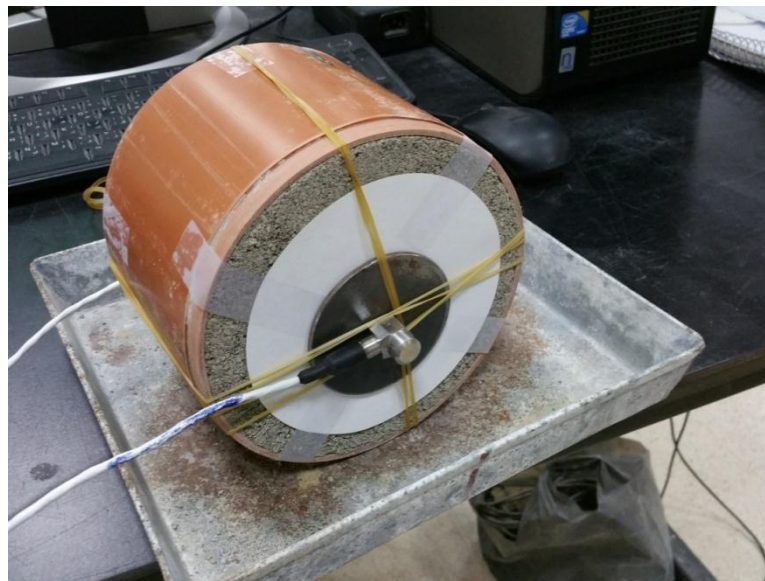


Figure 24: Final set-up for index tests

3.5. Parameters Studied in Index Tests

According to Marjanovic [33], accelerometers give high noise results compared to extensometers and ultrasonic P-wave transducers. In this research, for index tests, two accelerometers were attached to each specimen, as shown earlier, and were used to record sent and received signals. During preparation stage, a tube of PVC with 6 in diameter was cut into small tubes of 11.5 cm height at the manufacturing laboratory. In addition, a number of two accelerometers were used in the test. One accelerometer was used as a transducer where the waves were formed, and the other accelerometer was used as a receiver where the waves were collected. The two sensors were connected to a power supply and, at the same time, to a USB-PicoScope in order to digitize the data collected from the tests using a computer. Moreover, two circular steel plates were cut at the manufacturing lab and attached to the sensors from one side, and they were rested on the specimen from the other side. In addition, a steel spoon was used to hit the sensor in order to generate the waves at the sender end. The main objective of the index tests is to measure the variation of wave velocity with the sample void ratio, degree of saturation, and water content.

A number of 13 samples were prepared and tested at the Geotechnical Lab using the test setup shown in Figure 24 and described earlier. All the samples were mixed with 6% by weight initial water content, as evaluated from proctor tests. Moreover, all the samples were compacted into 5 layers using the modified hummer. Sample 1 was used as a reference sample, and it was compacted at 5 layers with 56 blows for each layer. This sample was prepared using a RAK soil after passing the 2 mm sieve size. In addition, samples 2, 3, and 4 were formed in order to study the effect of void ratio using three different compaction efforts of 28, 14, and 7 blows per layer, respectively, and they were then compared to sample 1 compacted with 56 blows per layer. All these samples were prepared using passing 2 mm sieve soil. Samples 5, 6, and 7 were prepared to study the effect of soil gradation on wave velocity. The three samples were compacted at 28 blows per layer and were compared later to sample 2. Samples 5 and 6 were formed using RAK sandy soil after sieving it on sieve No.16 (1.18 mm). Sample 7 was formed using a sandy soil which passed sieve No.30 (0.600 mm). Moreover, samples 8, 9, and 10 were prepared in order to investigate the effect of adding clay to the sandy soil. Three different percentages of

clay of 10%, 20%, and 30% have been used with samples 8, 9 and 10, respectively. These samples were prepared using a soil that passed the 2 mm sieve and was mixed with the clay content by weight. The three samples were compacted at 28 blows per layer and were compared later to sample 2 (reference sample).

The last three samples, which are samples 11, 12, and 13, were prepared in order to study the effect of adding a Portland cement on the wave velocity of sandy soil. Portland cement was added in percentage of 3%, 6%, and 9% of the mass of the dry soil and mixed before adding water. The three samples were compacted at 28 blows per layer for five layers. These samples were prepared using a soil passing the 2 mm sieve and were compared later with sample 2. All samples with different testing parameters are summarized in Table 3.

The protocol adopted for testing the first ten samples was the same, and the wave velocity was measured at six different timings as follows:

1. Measured directly after sample preparation.
2. Measured after oven drying the specimen to lose 50 g of water.
3. Measured after leaving the sample in air to cool down from the first heating.
4. Fourth, fifth, and sixth measurements were after heating the sample in the oven where the sample's weight kept decreasing by an increment of approximately 50 g. By that time, the soil specimen became fully dry.

On the other hand, specimens 11, 12, and 13 were tested daily for four days, and an additional test was conducted at 7 days of preparation to allow the specimens to lose water without heating and to allow the cement to be cured. Examples of fully dried and tested specimens are shown in Figure 25.



a) Sandy soil specimens



b) Cemented sandy soil specimens

Figure 25: Example of dried specimen after fully tested

After the specimens were dried and tested, some trials were conducted to measure the wave velocity in submerged sand. However, once specimens were immersed in water, they started to dissolve and damaged in less than 5 seconds. These trials were not completed due to the separation of the accelerometers from the specimens. Figure 26 shows an example of damaged specimens just after being soaked in water.



Figure 26: Dissolved sample after soaking in water

Table 3: Soil samples tested in index test and the parameters changed

Sample No.	Water Content (%)	Gradation type	Compaction effort	Clay Content (%)	Portland Cement Content (%)
1	6	Passing 2mm	56/layer	0	0
2	6	Passing 2mm	28/layer	0	0
3	6	Passing 2mm	14/layer	0	0
4	6	Passing 2mm	7/layer	0	0
5	6	Passing 1.18mm	28/layer	0	0
6	6	Passing 1.18mm	28/layer	0	0
7	6	Passing 0.6mm	28/layer	0	0
8	6	Passing 2mm	28/layer	10	0
9	6	Passing 2mm	28/layer	20	0
10	6	Passing 2mm	28/layer	30	0
11	6	Passing 2mm	28/layer	0	3
12	6	Passing 2mm	28/layer	0	6
13	6	Passing 2mm	28/layer	0	9

3.6. Scaled Footing Test

3.6.1. General

A large scale test was constructed in the Geotechnical Lab (setup_1), shown in Figure 27. The setup is composed of steel box with reaction frame, hydraulic actuator, load cells and LVDT's, a number four accelerometers, and impact source. In addition, a data acquisition to connect all these instrumentations is available in the Geotechnical Lab. The footing was manufactured of steel plates underlined with rigid wood. This setup was used to measure the shear wave velocity at different footing stress, and the settlement. The system is instrumented with geophysical equipment which is a group of geophone receivers and accelerometers. These instrumentations allowed the measurement of wave velocity during the application of different vertical stresses at the strip footing.

3.6.2. Sand Box and model instrumentations

The rigid sandbox used in this study has dimensions of 1.15 m high (H), with 1.4 m x 2.7 long and is located in the AUS Geotechnical Lab. The sand box is attached firmly to the lab floor in order to avoid any box movements. The footing dimensions are 1.39 m length and 0.15 m width to form a strip footing shape. The footing was manufactured of wood plat stiffened with a rigid steel beam from the top and lined with sand glued to the bottom. Two load cells were installed between the hydraulic actuator and the footing top in order to measure the vertical load transmitted to the footing (see Figure 28). In addition, three linear voltage displacement transducers (LVDT) were attached to the fixed reaction beam to measure the vertical settlement of the footing during subsequent loading stages. Loading was applied in incremental stages on the top of the strip footing using a displacement control hydraulic actuator (see Figure 28).

The waves should travel through the soil from right to left, passing first by accelerometer No.1. Then, the waves propagate towards accelerometers No. 2. The time lag between the two accelerometers is recorded and, by knowing the distance between each pair of accelerometers, the wave velocity can be determined. An example of time lag between accelerometers responses is shown in Figure 29. Finally, plots of wave velocity versus both footing settlement and soil pressure are generated.

These plots are used in order to derive the correlation between footing settlement, bearing capacity, and measured wave velocity.

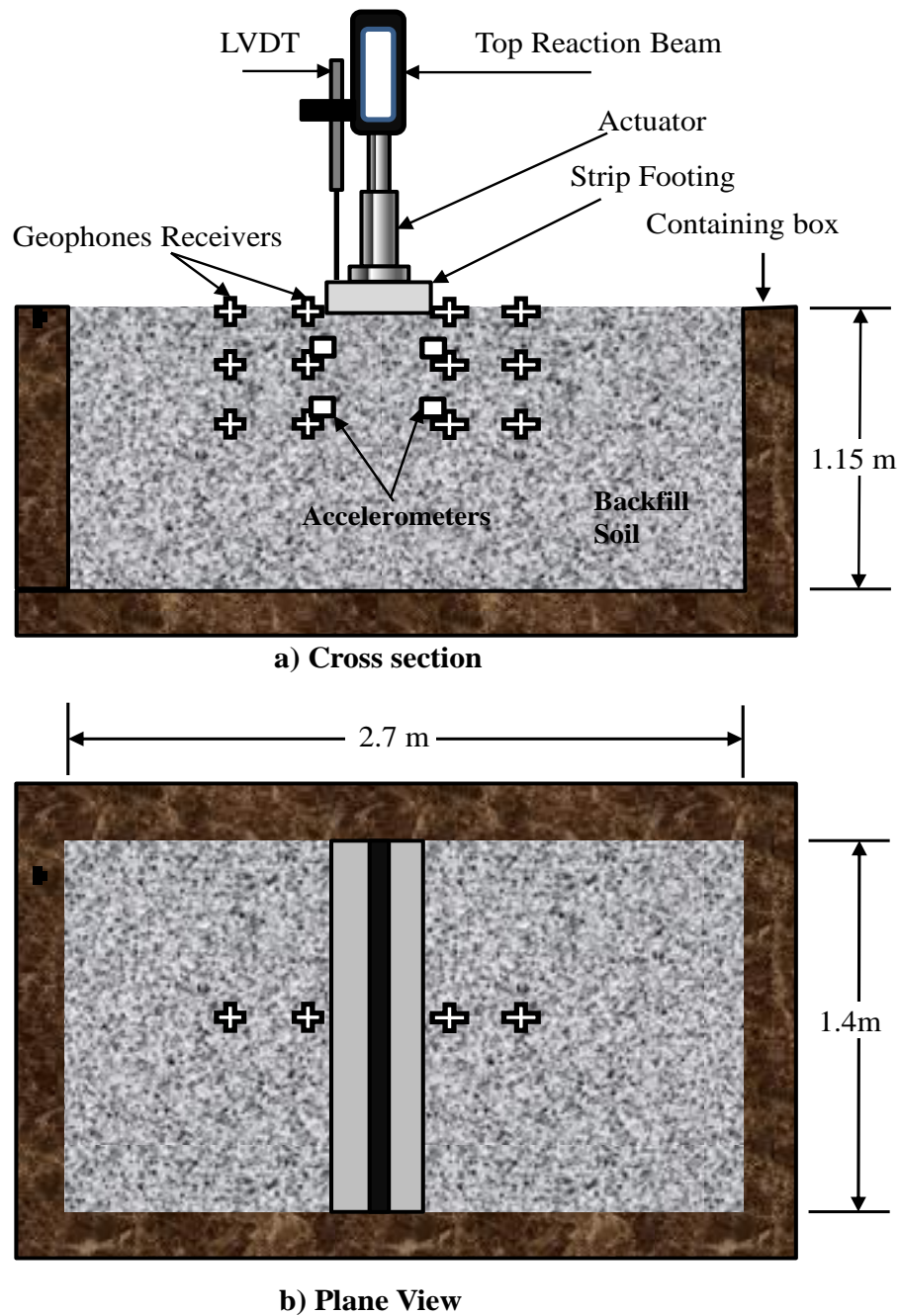


Figure 27: Schematic diagram for the large scale test model for strip footing with geophones and accelerometers

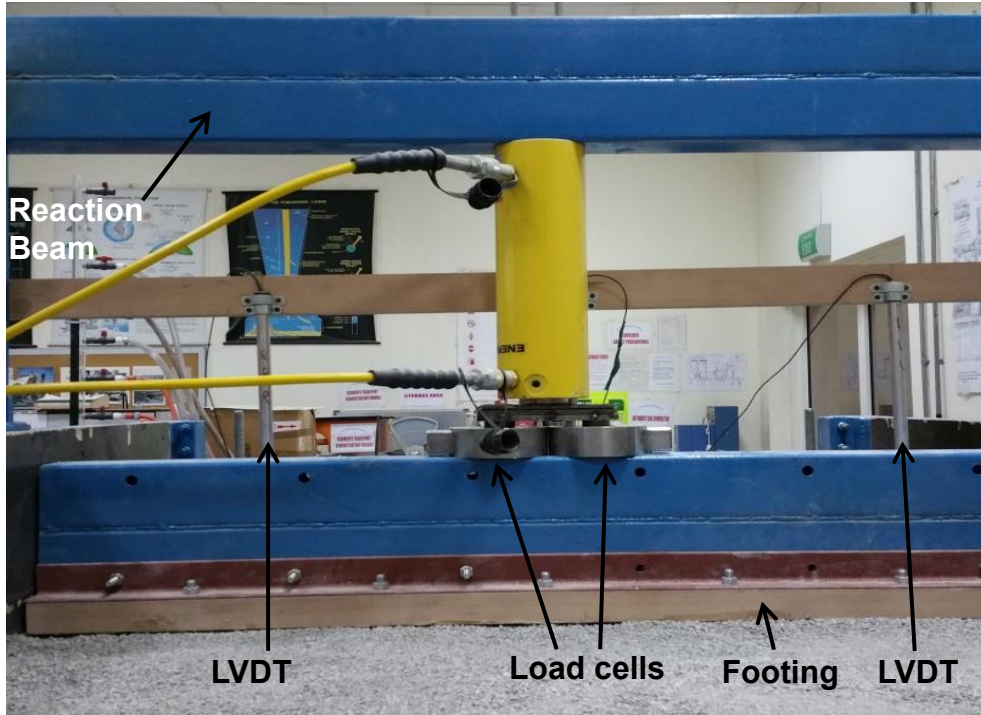


Figure 28: Two load cells under the actuator, LVDT's, strip footing, and reaction beam

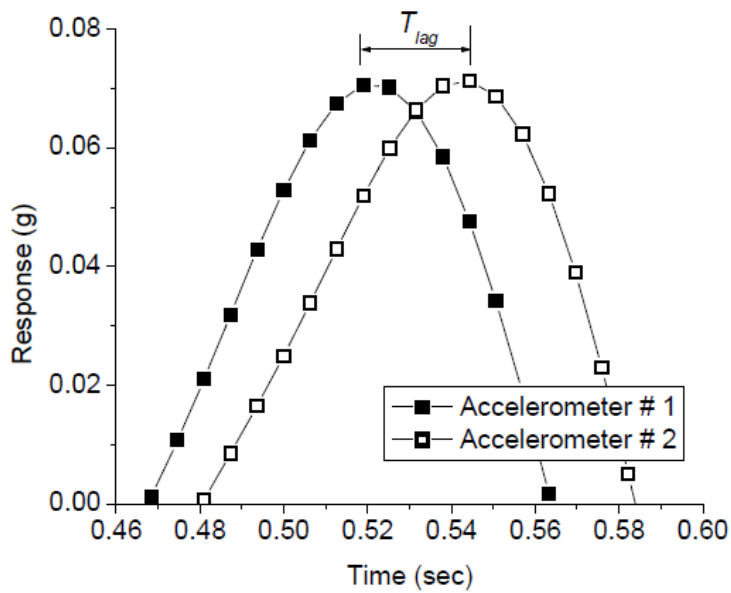


Figure 29: Example time lag of two accelerometers readings

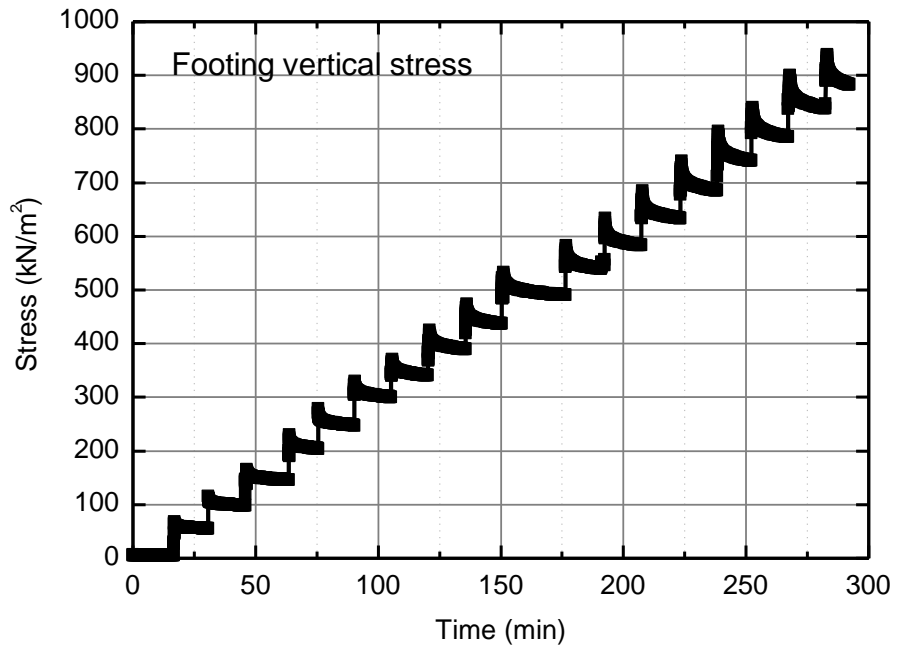
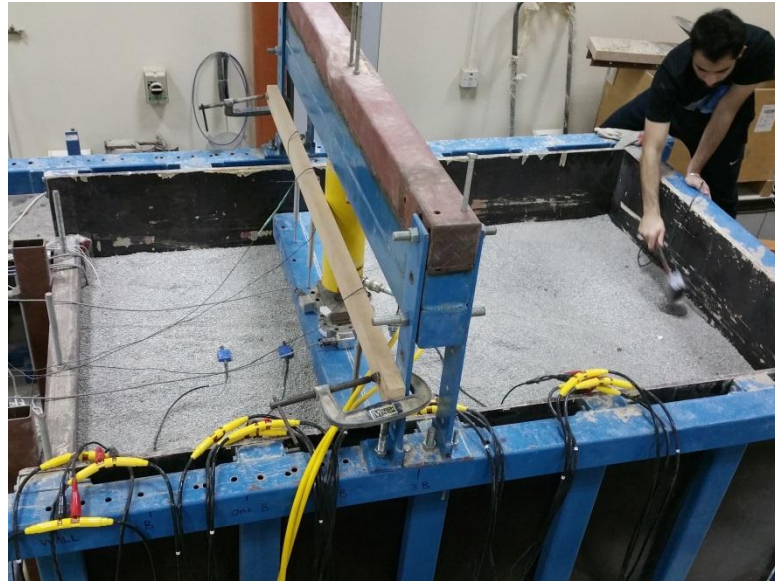


Figure 30: Applied vertical stress increment on the top of the strip footing



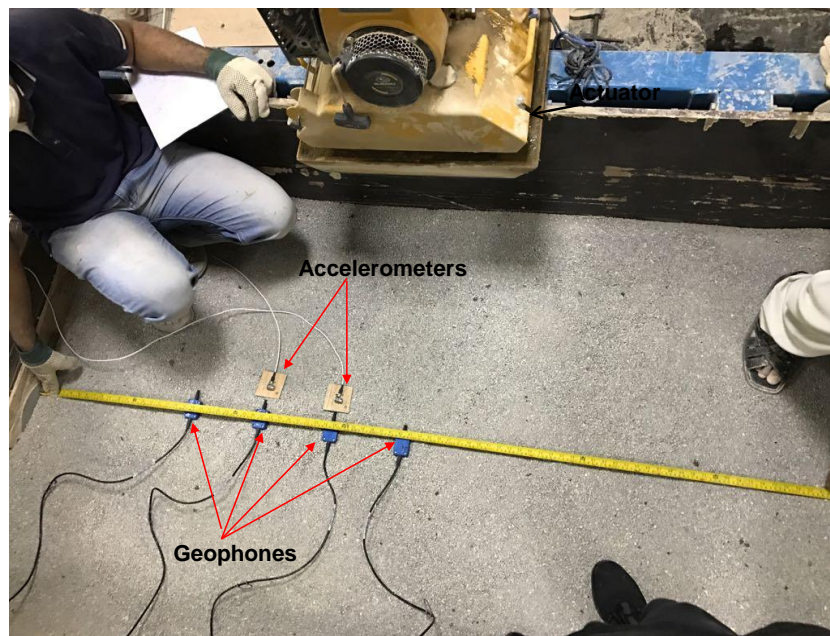
a) Side impact pulse location



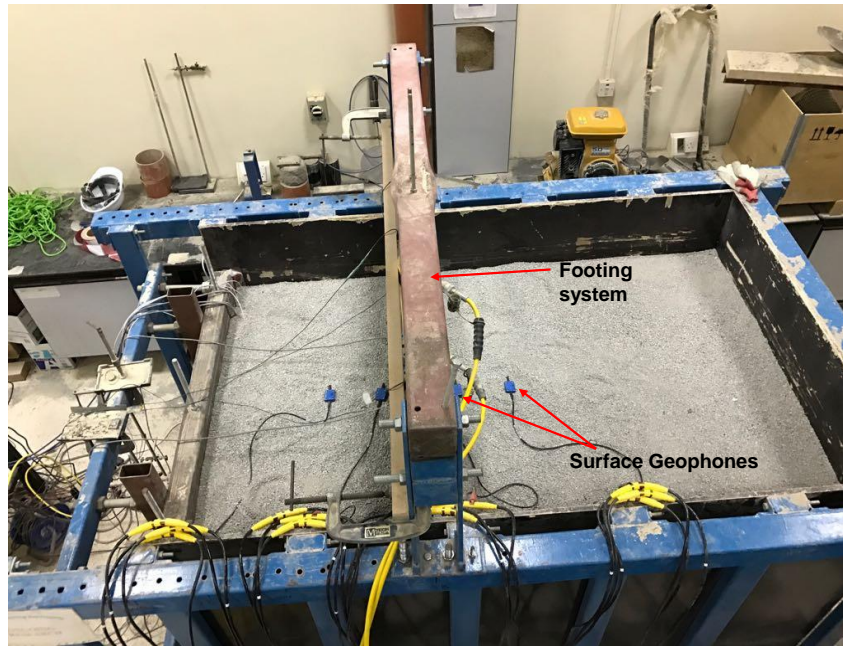
b) Top impact pulse location

Figure 31: Locations of top and side impact pulse hits

Example of measured footing load versus time is shown in Figure 30. At every loading increment shown in Figure 30, dynamic waves were generated by impact pulses at the right hand side of the steel sand box, both at the middle of the box height (Figure 31a) and at the top of the sand (Figure 31b).



a) Accelerometers and geophones inside the backfill.



b) Geophones at the top of the backfill surface.

Figure 32: Locations of Accelerometers and geophones inside the sand and at the backfill surface

As the objective of this research is to measure both soil bearing capacity and wave velocity at different loading stages, the test setup was equipped with four accelerometers, 12 geophones receivers, to measure the wave velocity and impact source to create waves. Geophones and accelerometers are used in this study in order to compare the accelerometers readings with the geophones readings for verification. Accelerometers are attached to a thin wooden plate to perfectly rest on the sand and to easily adjust the axis of motion with direction of generated waves as shown in Figure 32a. However, geophones have their own fixing fork that was attached vertically to the soil after compaction. Figure 32a shows a number of 4 geophones attached to the soil at certain depth, together with two accelerometers. Whereas, Figure 32b shows another 4 geophones inserted at the backfill surface of the model.

A data acquisition was used in this experiment to sample signals of real physical measurements and then convert them into digital values that can be stored by a computer and processed later. Data acquisition used in this research is shown in Figure 33. It should be noted that the geophones have their own acquisition system and are attached to a separate laptop, and the accelerometers are attached to a number of two PicoScopes that are attached to a third computer.



Figure 33: Data acquisition used with load cells and LVDT's

3.6.3. Model Compaction

To construct the soil-footing system, the backfill soil was placed in 5 thin lifts of 20 cm each and compacted by a 90 Kg plate vibrator (521mm × 432mm), producing 6100 vpm and a centrifugal force of 1550 Kg Force. Figure 34 shows the compactor and the compacted soil layers. After compacting the third layer, the first four geophones were installed at the pre-specified locations, at depth of 30 cm ($d = 2B$) below the backfill surface. The horizontal distance between each geophone is 20 cm and was distributed in a way that the two geophones that were in the middle were exactly aligned under the two sides of the footing. The other two geophones are located 20 cm from the two middle geophones, one in each side. Two accelerometers were also embedded exactly next to the two geophones that were in the middle, or that were at each side of the footing. At a depth of 15 cm from the backfill surface, another four geophones were installed exactly with the same horizontal locations and distribution of the first four. In addition, two other accelerometers were embedded next to the two middle geophones. Figure 32a shows the distribution and locations of the four geophones, and the associated two accelerometers at depths 30 cm and 15 cm below backfill surface. At the top of backfill surface, the last four geophones were installed, two at each side of the footing with 20 cm horizontal distances as shown in Figure 32b.

Two different methods have been used to hit the sand box to create dynamic wave propagation. The first method is to hit the box from the back side on a rigid steel bar that was attached to the sand inside the box through a drilled hole, Figure 31a. The second method is by hitting on a circular steel plate that was placed at the surface of the backfill soil, Figure 31b. The standard hammer associated with the geophones was used in hitting the model from top and side. This hammer was connected to the recording station where all geophones were connected to as well. This procedure is used with all strip footing loading increments.

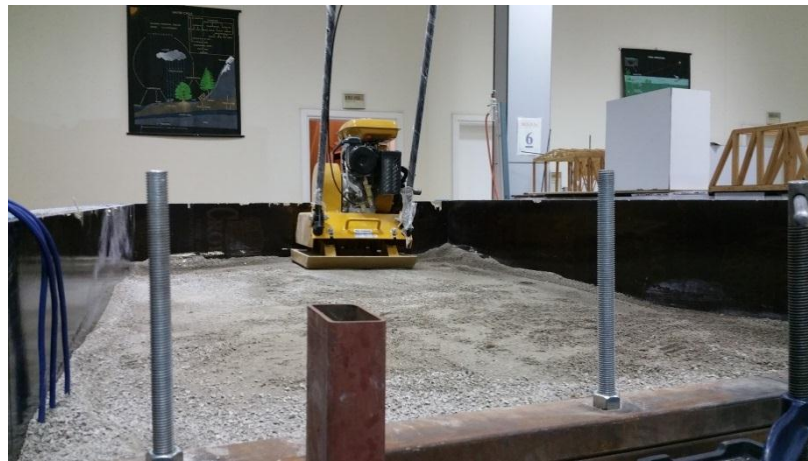


Figure 34: Soil compaction stages during construction of the model footing

3.6.4. Signal processing and interpretation

For any seismic velocity measurement, two parameters are needed to be determined: the travel distance and the travel time. Determining the travel time is considered to be the most complex parameter as the output signals are always different from the input signals. There are a number of methods for the determination of the first time arrival, ranging from the visual observation of the wave to deeper techniques of signal processing tools.

According to Black [34], there is more than one method of picking the first arrival of generated dynamic waves. Figure 35 shows an example of a transmitted signal of a bender element test. Visually picking the arrival position is considered to be the most common method used for the bender element interpretation. This approach was examined and results show that it works successfully (Viggiani and Atkinson, 1995; Arulnathan et al., 1998; Lings and Greening, 2001; Clayton et al.,

2004; Porbaha et al., 2005) [35], [36], [37], [38], and [39]. On the other hand, there were several difficulties reported for the identification of the first arrival of the received wave. Figure 35 shows that the first arrival time can be chosen at three different locations, where the first deflection occurs at (Point 1), and then the signal starts increasing until it reaches the first inflection at (Point 2) or to the first major peak at (Point 3).

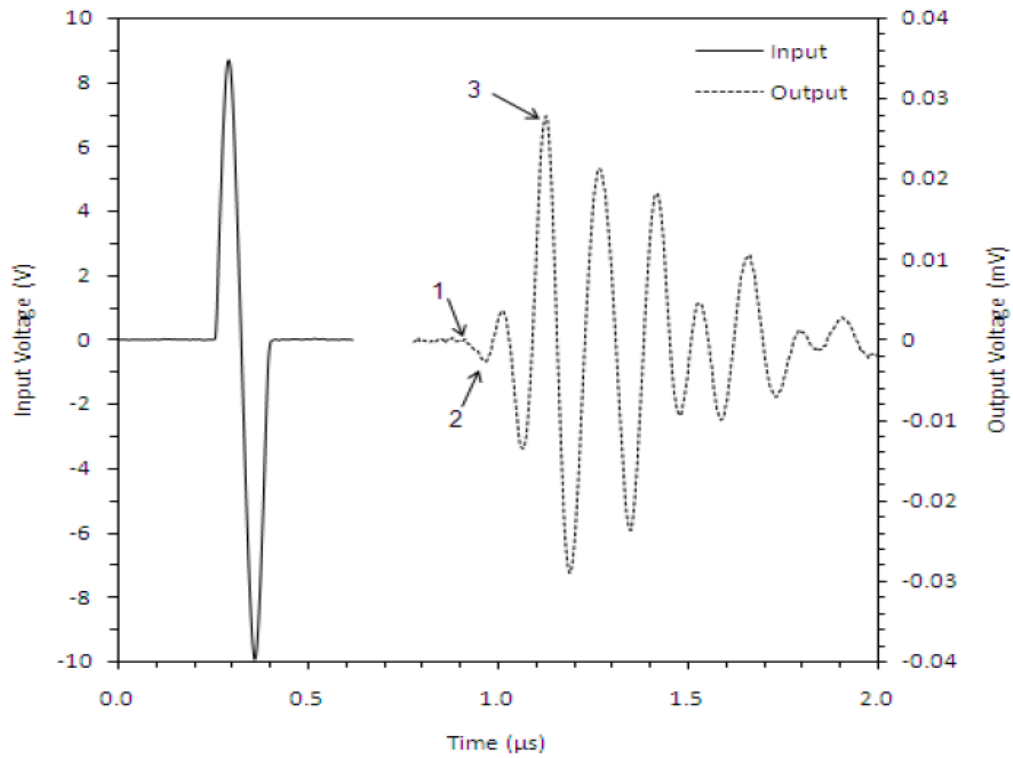


Figure 35: transmitted signals from a bender element test [35]

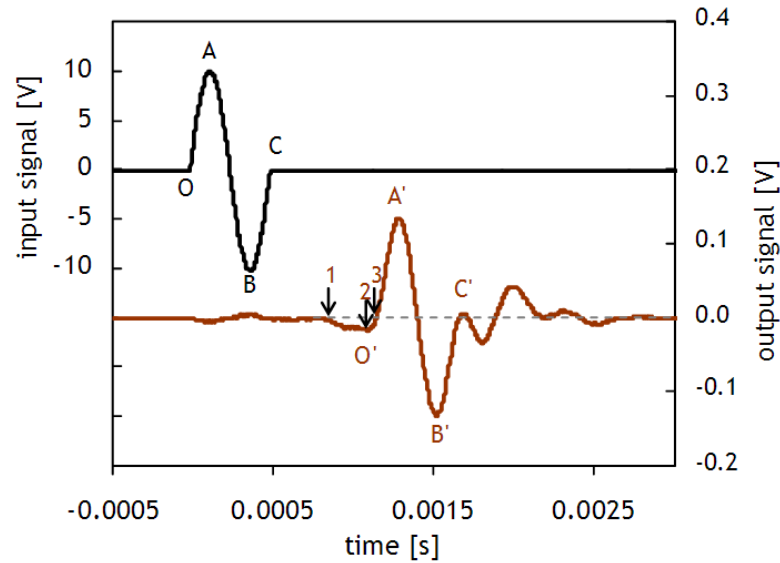


Figure 36: Time domain interpretation methods [35]

First direct arrival of the output wave is one of the proposed methods. It is considered to be the simplest method; it depends on user's visual interpretation. This method is similar to the one used in geophysical tests in the field (Abbiss, 1981; Dyvik and Madshus, 1985; Jamiolkowski et al., 1995; Jovicic et al., 1996; Pennington, 1999). However, the main disadvantage of this proposed method is that different users may choose different arrival points (e.g., points 1, 2, or 3) as shown in Figure 35.

Another method selects the arrival time at characteristic points, such as peaks, zero intercepts, and troughs. The travel time is taken as the time difference between two corresponding points (Points AA' or points BB') as shown in Figure 36. Nonetheless, the disadvantage of this method is that the successive intervals AA' and BB' are not identical, and the later intervals tend to be greater than the early intervals, so the use of this method is not highly recommended for the arrival time determinations.

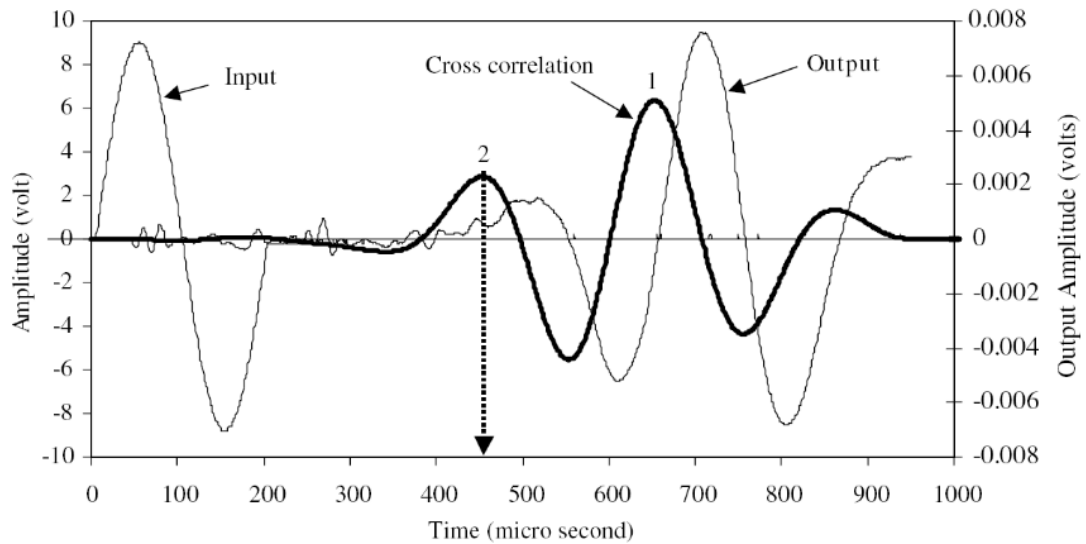


Figure 37: Input, output, and cross-correlation signals [40]

Cross-correlation of input and output signals is also a proposed method for determining the first arrival time of signals. This method consists of measuring the degree of correlation of any two signals. However, the major limitation of this method is that it is difficult to determine the correct peak in the cross correlation signal. According to Mohsin and Airey [40], the cross correlation of single frequency pulse (input wave) with the response of it produce a peak at a time shift, where that time shift is taken as the travel time between the two signals. Figure 37 shows an example of the cross-correlation technique.

In this research, for the large scaled test, a different method is used in order to pick the first arrival time of the transmitted waves. The used method consists of drawing a tangential line to the first deflection of the signal, and making that tangential line intersects with the x-axis at $y=0$. The first arrival time was taken exactly at the intersection point between the tangential line, and the x-axis. Figures 38 and 39 show an example of picking the first arrival times for both accelerometers and for the all geophones as well.

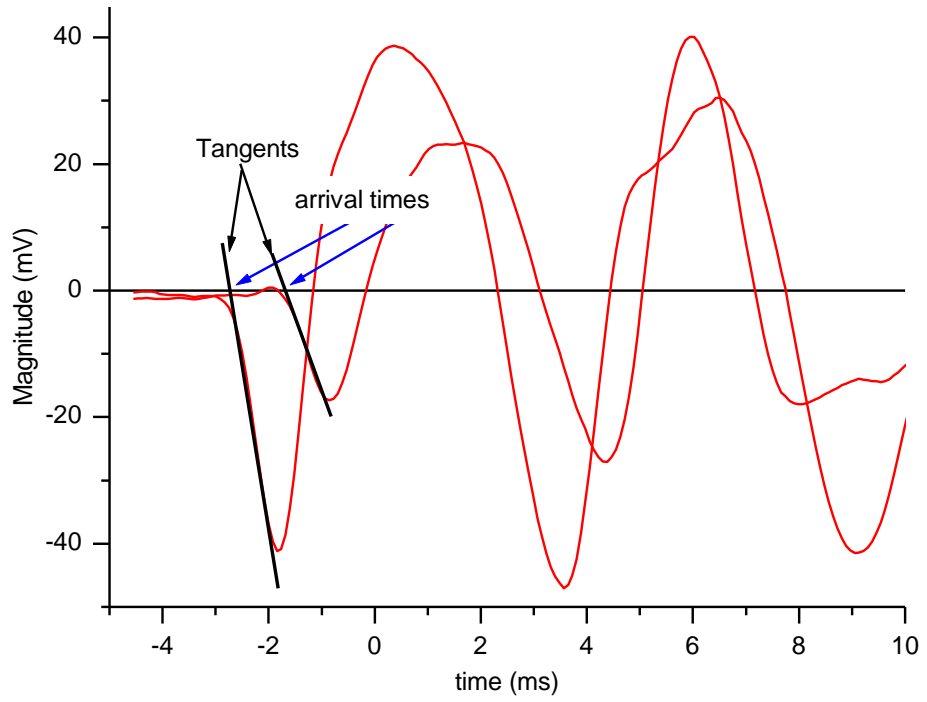


Figure 38: Determination of the accelerometers first arrival times

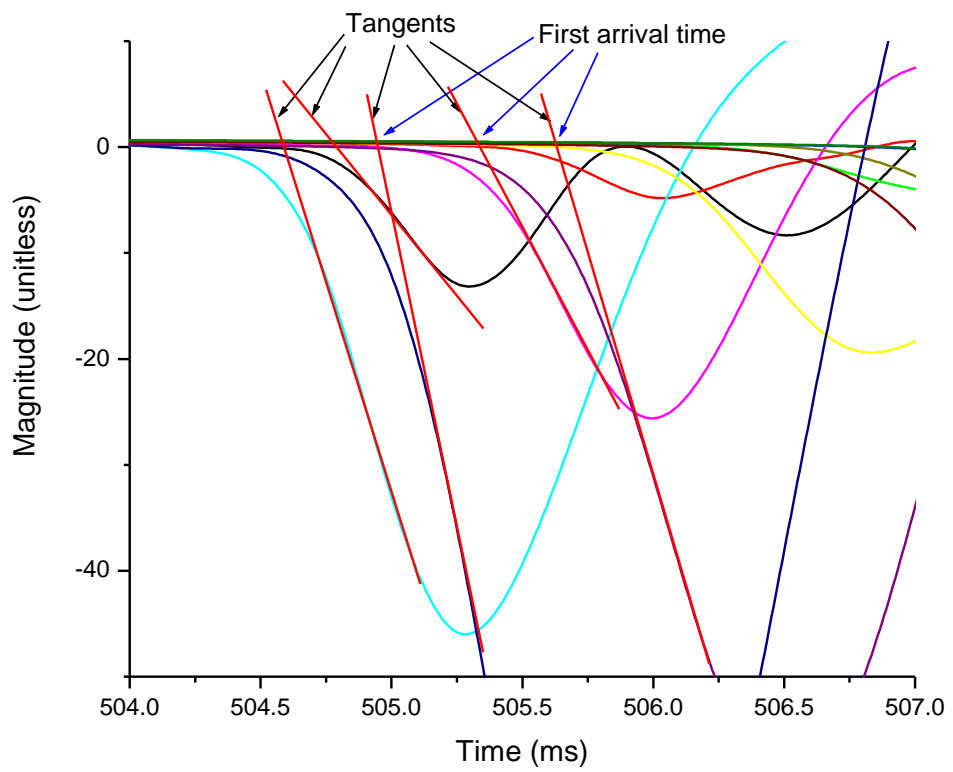


Figure 39: Determination of geophones first arrival times

Chapter 4: Results and Discussion

4.1. General

This chapter presents results of the experimental program conducted during this study. First, index test results that are performed to study effect of different soil parameters on the wave velocity are introduced. Effect of degree of compaction, which is reflected on void ratio on each soil specimen, is presented. Second, different soil gradation, starting with the original RAK soil, moving to soils passing 2 mm and 1.18 mm sieves, and ending by fine soil that is passing 0.6 mm sieve are explained and discussed. Then, the effect of clay content on the measured wave velocity is investigated and presented. Finally, the effect of cement inclusion with the original RAK soil passed by 2 mm sieve is explained and presented.

The second part of this chapter presents results from the large scale footing test. First, variation of wave velocity profile under the strip footing is presented at different applied vertical stresses. After that, wave velocity from both geophones and accelerometers is compared and presented as a relationship of footing applied stresses. Finally, relationship between applied vertical stress at the footing and measured velocity at different locations around the footing is discussed.

4.2. Index Tests Results

The arrival times of compression waves (P-waves) are estimated as the first deflection of the signals on time domain. Figures 40 and 41 show typical compression wave form obtained in this study. The travel time is obtained by considering the time lag between the taking-off of the input signal and the taking-off of the output signal (ΔT). In case of sinusoidal excitation, Jovicic et al. [41] suggest that the rising-to-rising travel time is defined as the time increment between the takeoff of input signal to the first zero crossing point on the time domain of the output signal. The criteria employed to determine the travel times based on rise to rise of signals is used also by Suwal and Kuwano [42]. Another method to estimate the travel time is to consider the peak-to-peak time lag, which is the time difference between the peak of the input signal and the peak of the output signal, which are clearly defined in Figure 41. It could be seen from Figure 41 that there is 8% difference between the two methods in determining the arrival time. However, this difference consistently occurs for all

tested samples. Therefore, for parametric comparison, this difference is eliminated and has no effect on the resulted wave velocity of all soil samples. In this study, the travel time is determined as the time difference between the arrival times of both input and output signals.

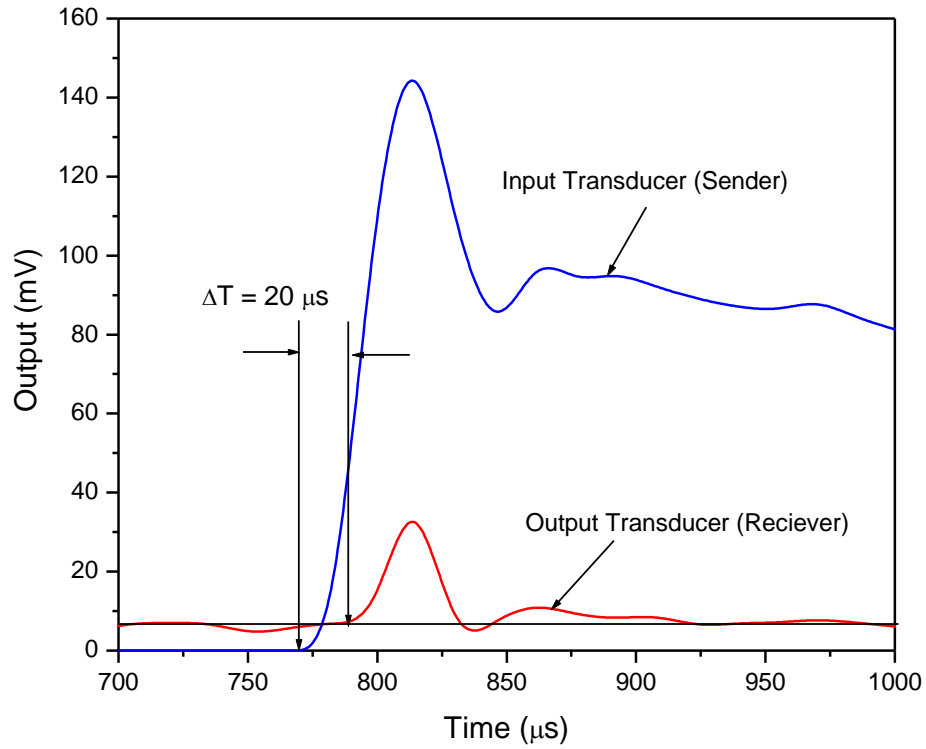


Figure 40: Using the first arrival for estimating the travel time

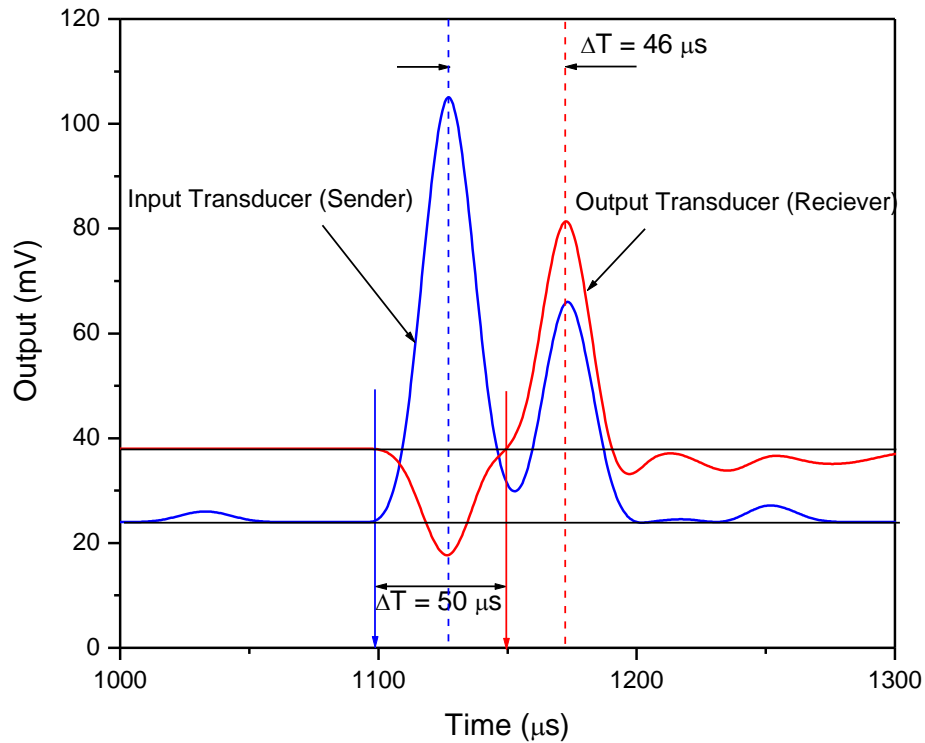


Figure 41: Using peak-to-peak, and first arrival for estimating the travel time

4.2.1. Effect of degree of compaction and void ratio

As mentioned in Chapter 3, samples 1, 2, 3, and 4 were prepared of the same soil (i.e., soil passing 2 mm sieve size) and compacted at the same initial water content which is $w = 6\%$. The main difference between the four samples is the compaction efforts used during compaction, which are 56, 28, 14, and 7 blow/layer for samples 1, 2, 3, and 4, respectively. Different compaction effort is expected to produce soil with different void ratio, different degree of saturation, and different water content percent. Variations of P-wave velocity with water content percent, degree of saturations, and void ratio are shown in Figures 42, 43, and 44, respectively. Figures 42 and 43 indicate that the P-wave velocity decreases as the soil water content and degree of saturation increases, regardless of the degree of compaction or the compaction effort used. It is well understood that the existence of water might increase the wave velocity, provided that the soil is fully saturated. In the current cases, the maximum degree of saturation is 60%, attained by soil specimen 2 in Figure 43, which is far below the 100% saturation. Even though the P-wave velocity at this high degree of saturation starts to pick up again towards an increasing trend, some other specimens start the trend of velocity increase at early values of degree of

saturation; for example, 22%, as shown by specimens 3 and 4 in Figure 43. These values of degree of saturation where the velocity started to increase are called threshold values. It could be concluded that the P-wave velocity decreases with increasing water content up to water content range of 3.75% to 4.5 % (see Figure 42). Once the water content value increases beyond this range, the wave velocity starts to increase. In addition, a P-wave velocity decrease with the degree of saturation is up to threshold values degree of saturation (S_{TH}). Figure 42 indicates that the threshold degree of saturation increases with the compaction effort.

Both Figures 42 and 43 indicate that compaction effort (i.e., degree of compaction) highly affects the measured P-wave velocity. At the same water content or same degree of saturation, the soil with high compaction effort shows high values of wave velocity compared to the soil with low compaction effort. For example, Figure 43 indicates that, at degree of saturation $S = 20\%$, $V_P = 361, 275, 135$ m/s for soil compacted with 56, 28, and 14 blow/layer, respectively. This result is clarified in Figure 44, which relates the wave velocity to the soil void ratio with variable water content. Soil void ratio decreases as the compaction effort increases, and hence the soil wave velocity increases. Finally, it can be concluded from Figure 44 that the wave velocity increases with water content decrease, as previously shown in Figures 42 and 43.

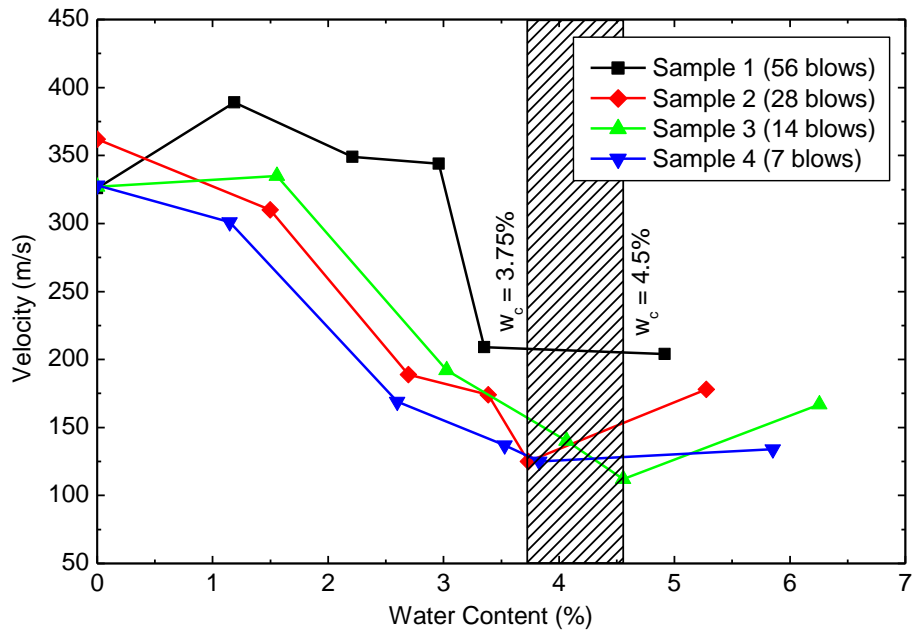


Figure 42: variation of P-wave velocity with water content, at different compaction effort

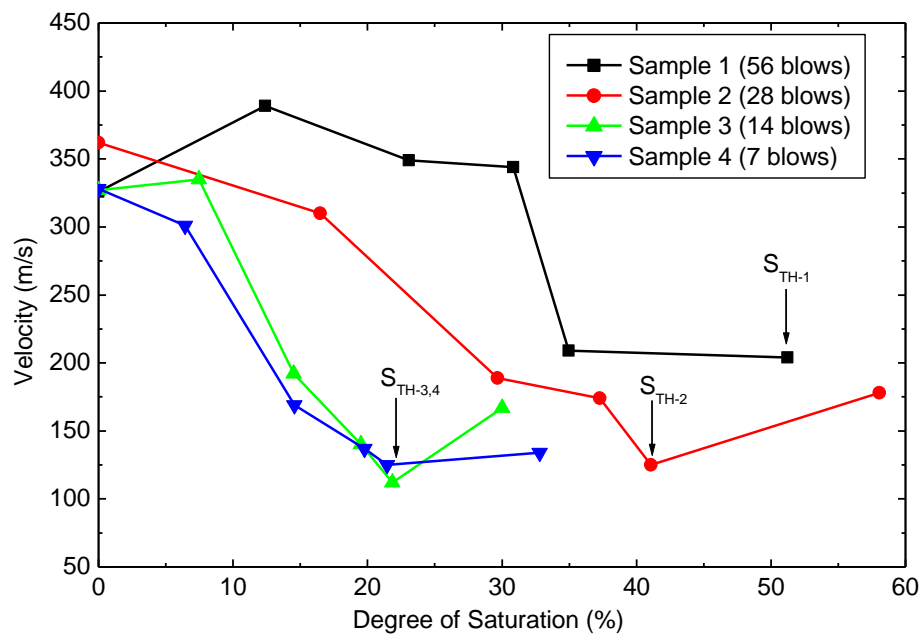


Figure 43: variation of P-wave velocity with degree of saturation, at different compaction effort

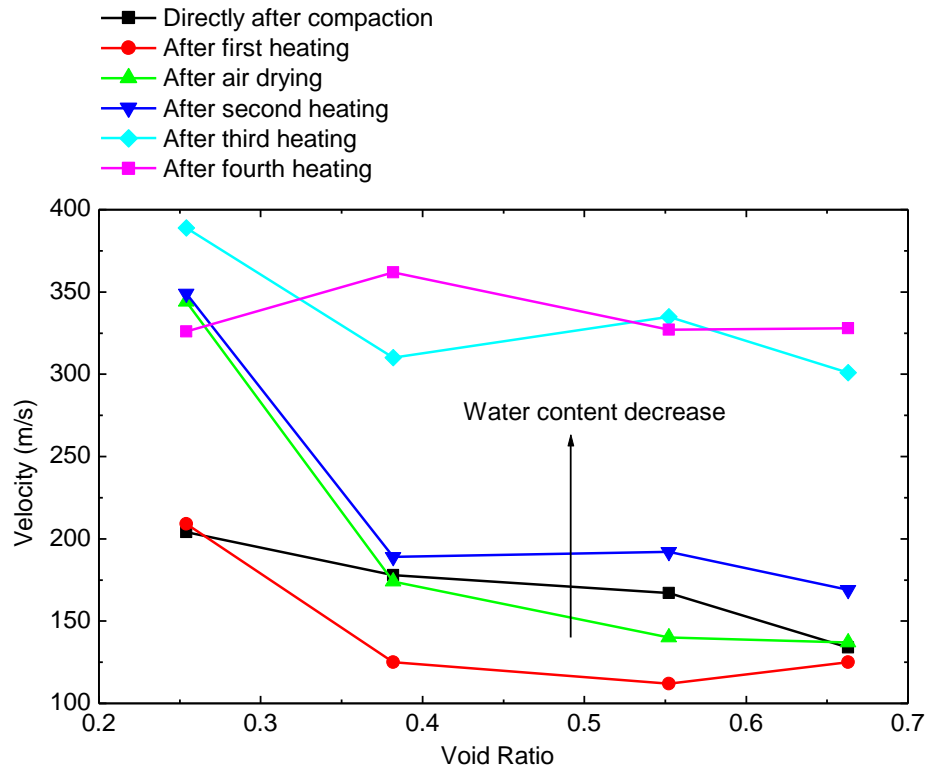


Figure 44: variation of P-wave velocity with void ratio, at different compaction water content

4.2.2. Effect of soil grain size distribution (soil gradation)

Soil gradation is expected to affect wave velocity, provided that all other factors kept similar. Three different soil gradations have been developed from the original RAK soil, as shown in Figure 14. These soil types have been created by passing the original RAK soil through different sieve sizes. Soil_1 passes 2 mm sieve size, soil_2 passes 1.18 mm sieve size, and soil_3 passes 0.6 mm sieve size. Figures 45 and 46 show respectively effects of water content percent, and degree of saturation on the measured P-wave velocity of 3 soil types. Figure 45 indicates that the wave velocity decreases with the increase in water content up to the range of 3.6% to 4.5%. When the water content of the soil specimen increases beyond this range, the wave velocity starts to increase. This result confirms the previous results presented in Section 4.2.1 about the variation of wave velocity with the water content. However, the effect of the soil gradation is not significantly clear in Figure 42.

Results in Figure 46 clearly show that the wave velocity of the soil decreases with the increase of the degree of saturation, up to threshold value of degree of saturation, S_{TH} . Once the degree of saturation of the soil specimen exceeds the

threshold value, wave velocity starts to increase accordingly. Figure 46 confirms that values of threshold degree of saturation significantly depend on the grain size distribution of the soil. As the grain size distribution of the soil becomes finer, the value of threshold degree of saturation increases. It can be seen from Figure 46 that the values of threshold degree of saturations are: $S_{TH-7} = 59\%$ (finer soil), $S_{TH-5} = 30\%$, and $S_{TH-3} = 22\%$ (coarser soil).

Figure 47 compares wave velocity for soil specimens 3, 5, and 7 at selected degrees of saturation. It can be noticed that the soil with coarse grain size distribution (i.e., specimen 3) indicates larger void ratio, “ e ”, while the soil with fine grain size distribution (i.e., specimen 7) indicates smaller void ratio “ e ”. At all selected values of degree of saturation, the soil specimen with lower void ratio “ e ” shows larger P-wave velocity compared to the other specimens with lower void ratio “ e ”. In addition, results in Figure 47 confirm that the wave velocity decreases as the degree of saturation of the soil increases.

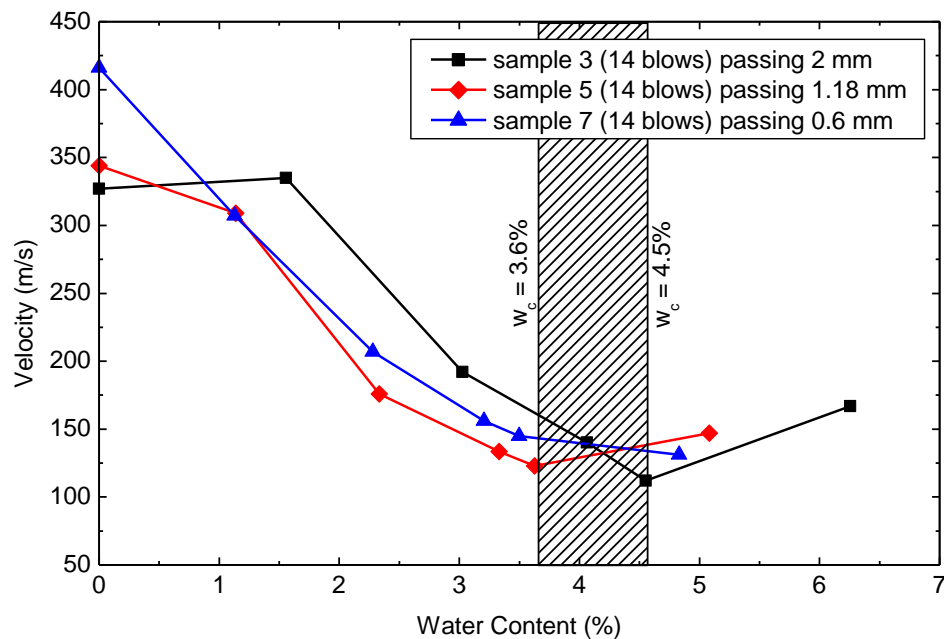


Figure 45: Variation of P-wave velocity with soil water content, for different soil types

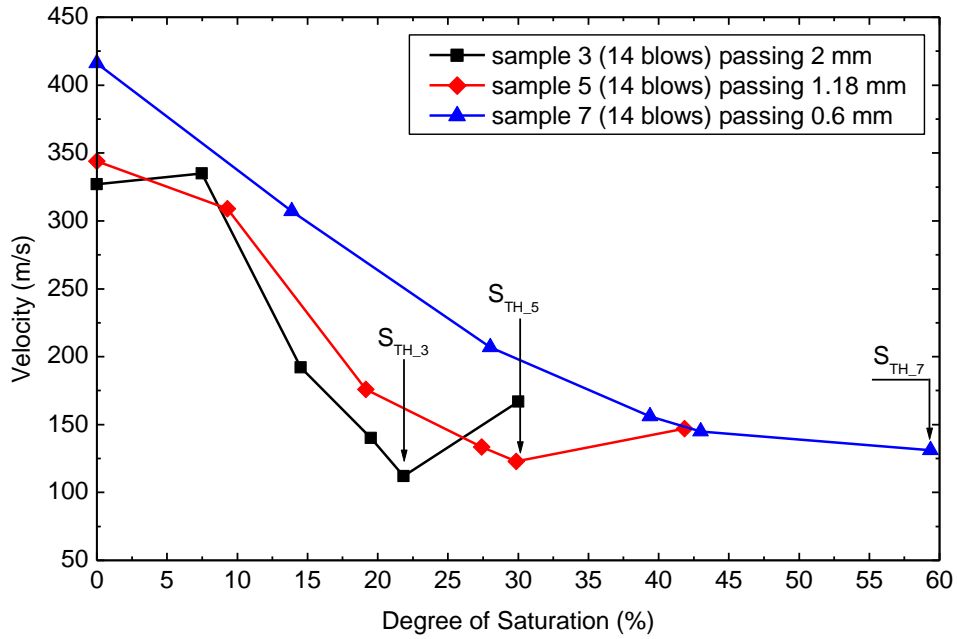


Figure 46: Variation of P-wave velocity with soil degree of saturation, for different soil types

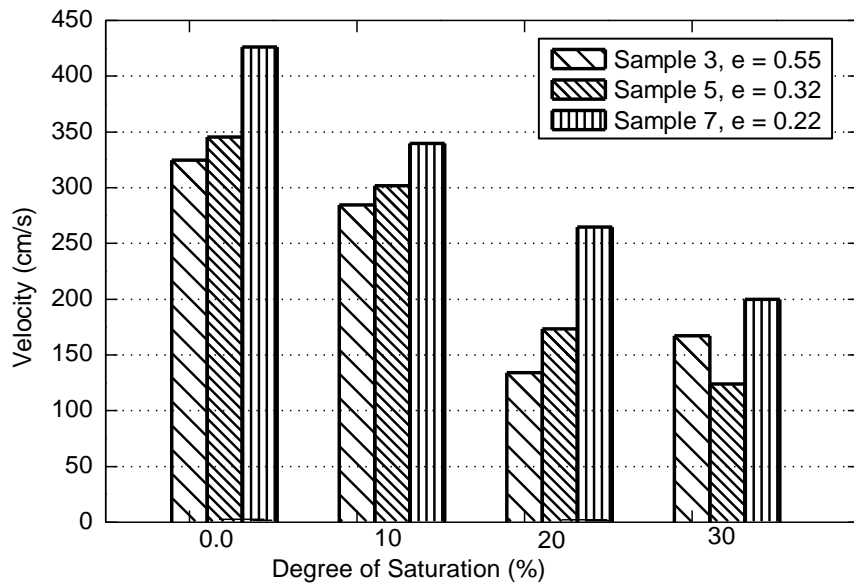


Figure 47: Comparison of P-wave velocity for soil types, at different soil degree of saturation

It can be seen that the effect of compaction effort on the measured shear wave velocity presented in Sections 4.2.1 is approximately similar to the effect of soil grain size distribution presented in Section 4.2.2. Moreover, the variation of the wave velocity with water content and degree of saturation is approximately similar for different compaction effort and different gradations. This is expected as the compaction effort and grain size distribution affect void ratio in a similar way.

4.2.3. Effect of clay content

Soil specimens 8, 9, and 10 were prepared with clay content of 10%, 20%, and 30%, respectively, in an effort to study the effect of clay content on sand wave velocity. All soil specimens were compacted with the same compaction effort, and at the same initial water content percent. Variations of P-wave velocity versus water content and degree of saturation for sandy soil contaminated with different clay content percent are shown in Figures 48 and 49. It can be seen that, for soil with zero clay content, the wave velocity significantly decreases with the increase in water content and degree of saturation up to water content of $w_c = 3.7\%$, Figure 48, and increases thereafter. It should be noticed that at this water content percent, the degree of saturation is $S = 41\%$ (Figure 49). Once the clay content increases to 10%, the wave velocity decreases slightly with the increase in water content and degree of saturation up to $w_c = 5.6\%$, as shown in Figure 48, and decreases significantly thereafter. At water content $w_c = 5.6\%$, Figure 49 indicates that the degree of saturation is $S = 50.7\%$, as shown in Figure 49. For specimen with clay content equal to 20%, wave velocity doesn't show any change with water content nor with degree of saturation up to $w_c = 6.1\%$, Figure 48 (which corresponding to $S = 56\%$, Figure 49) and considerably decreases thereafter. When the clay content in the specimen increases to 30%, the variation of wave velocity with water content and degree of saturation takes a trend of increase, instead of decrease it shows with lower clay content. For this clay content (i.e., clay content= 30%), wave velocity increases with water content and degree of saturation up to $w_c = 6.7\%$, Figure 48 ($S = 53.3\%$, Figure 49). The water content threshold values and the acceleration threshold values, where the trends of variation change its direction from increasing to decreasing and vice versa, are shown to increase with the clay content. Finally, it could be noticed that the trend of wave velocity variation with the increase in water content change gradually from a significant decrease to a slight increase, passing through a slight decrease and a non-change trend.

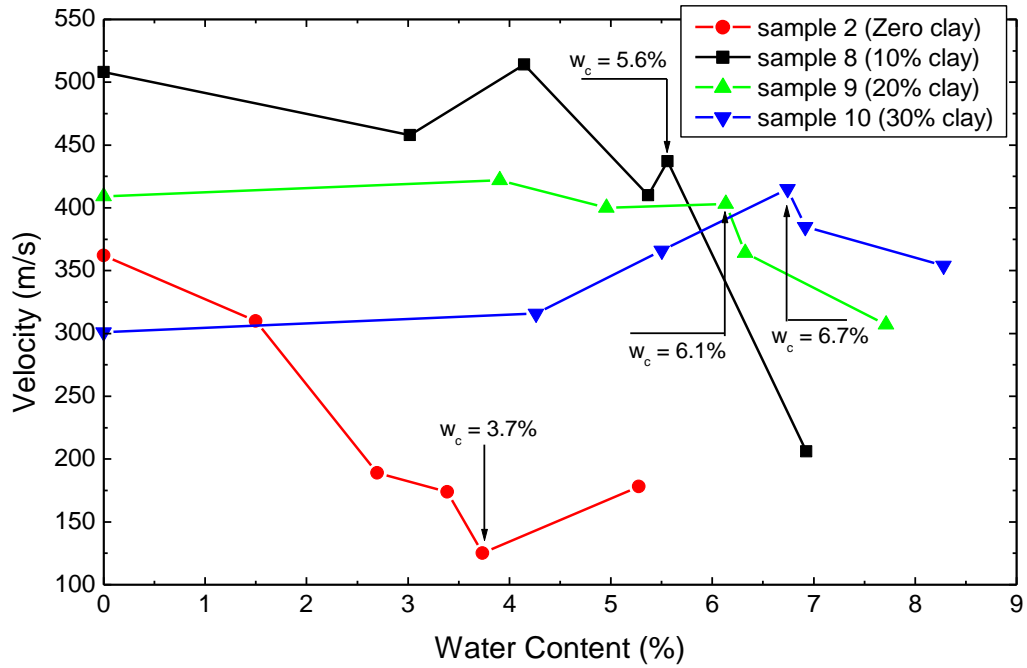


Figure 48: Variation of P-wave velocity with soil water content, at different clay contents

The effect of clay content on the P-wave velocity at different drying stages is shown in Figure 50. It is clear from the figure that, with the exception of the measurement directly after compaction, all other measurements indicate that the wave velocity increases as the clay contents increase up to 10%. Once the clay contents increases beyond 10%, the wave velocity started to decrease. The only exception of this is the measurement of wave velocity directly after specimen compaction, which indicates an increase of the wave velocity with clay content at all percentages of the clay. It can also be seen from Figure 50 that the water content affects the wave velocity at different clay contents, and as the water content increases, the wave velocity decreases at most values of clay contents. It is worth noting that the void ratio of sample 2 (pure sandy soil) is $e = 0.37$ while samples 8 and 9 with 10% and 20% clay contents respectively have void ratio of $e = 0.29$. Moreover, sample 10 with 30% clay content has a void ratio $e = 0.32$. Therefore, the three samples with clay contents show very close values of void ratio, which eliminates the void ratio as an effective parameter in this case. In conclusion, the variation of the P-wave velocity is not only dependent on the individual values clay content percent, but also on the water content at this clay content.

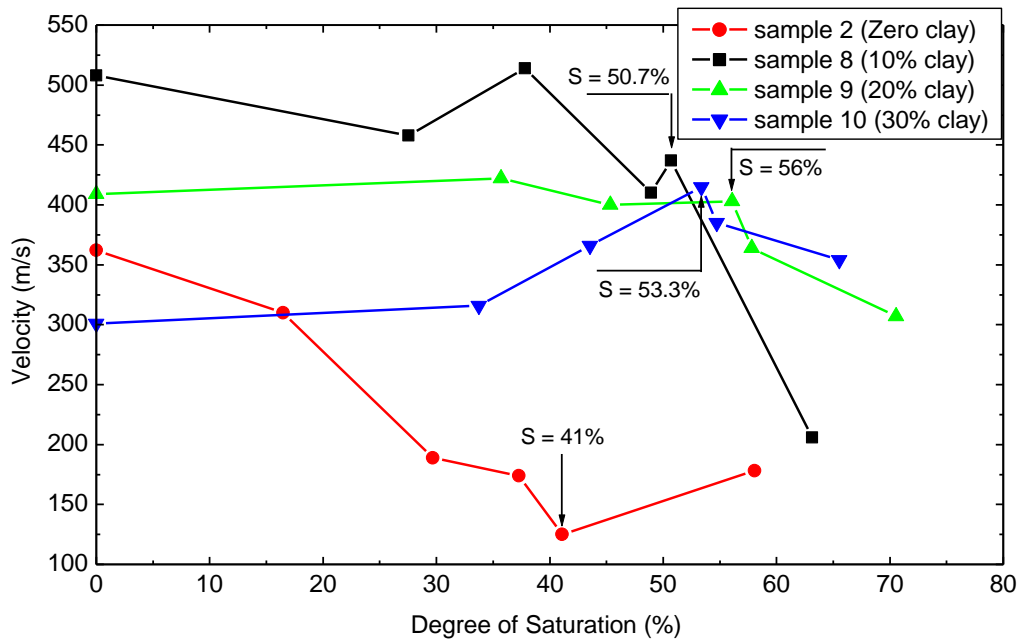


Figure 49: Variation of P-wave velocity with soil degree of saturation, at different clay contents

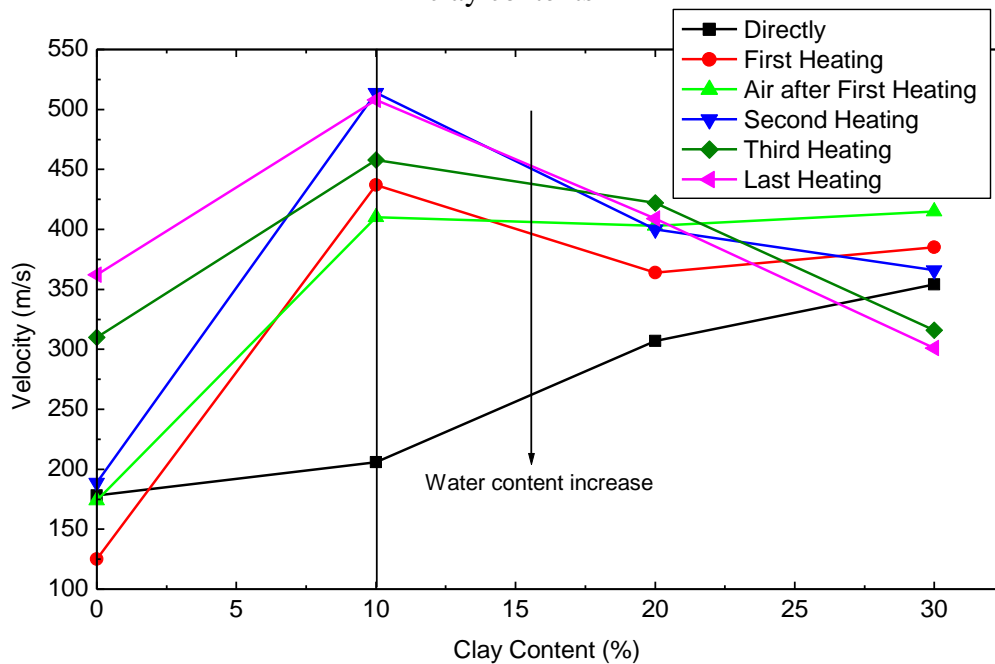


Figure 50: Variation of P-wave velocity with soil clay contents, at different degree of dryness

4.2.4. Effect of portland cement content

Samples 11, 12, and 13 were prepared and tested in order to study the effect of cementitious materials, such as Portland cement, on wave velocity of cemented sand. Figure 51 shows the effect of the percent Portland cement content on the wave velocity at different curing days. These results indicate clearly that the wave velocity

increases as the cement content increases, especially if the specimen is tested after longer time after preparation and compaction. If the cemented specimen is tested directly after compaction, it shows negligible effect of the cement content on the wave velocity. This is expected because, at this time (i.e. minutes after compaction); the cement does not cure yet and does not provide the adhesion effect to the sand particles. The most increase in wave velocity is measured after first and second days of specimen compaction. This is because the hydration of the cement grains occurs mostly during these two days. On the third day after specimen preparation and compaction, the rate of hydration slows down and the gain in specimen strength/stiffness becomes less. Therefore, a slight increase in the wave velocity occurs at the third day, and surprisingly, a decrease in the wave velocity occurs on the seventh day. Finally, the rate of increase of wave velocity with cement content percent approaches the highest on the second day of specimen compaction; this is attributed to the same reason stated earlier.

The behavior explained in the previous paragraph can be clearly seen in Figure 52, which relates wave velocity with curing time in days at different cement content percent. It can be seen that the wave velocity increases almost linearly with time in days up to the second day of sample compaction. Then, the rate of increase (i.e., slope of the line) starts to decrease up to the third day, and then a slight decrease is noticed in the velocity after a week of sample preparation. It is clear that the specimen attains its maximum wave velocity and stiffness after three days of compaction. On this day, the wave velocity and the soil stiffness become almost 4 times of their values of pure sand soil, at 3% cement content. As the cement content percent increases, the wave velocity and soil stiffness gain increase, but not equivalent to the cement content increase which; for example, doubled from 3% to 6%. Zooming on day 3 of sample compaction, it can be realized that adding 3% of Portland cement increases the wave velocity from 200 m/s to 1000 m/s; whereas, adding 9% of the same cement increases the wave velocity from 200 m/s to 1300 m/s. Therefore, the addition of 6% cement to the first 3% does not improve the soil stiffness significantly as the first 3% cement. Finally, the trend of wave velocity variation with time is almost similar for the three different cement contents used in this study.

Figure 53 shows the variation of the wave velocity with water content percent at different cement contents. In fact, the change in water content indicated in the

figure is not due to drying as in cases of un-cemented specimens before. Instead, this change in water content is due to cement hydration with time. It is well-known that, as the cement content increases, the water required for cement hydration increases as well. This could explain the difference in the specimens initial water contents, $w_{c-3\%} = 2.45\%$, $w_{c-6\%} = 1.55\%$, and $w_{c-9\%} = 0.95\%$ despite the fact that all specimens were mixed with the same 6% water content during specimens preparations. These water contents were measured after one hour of sample compaction, where the first setting time of cement occurred and consumed the majority of the 6% water content during hydration. It could be seen that, after 7 days of curing, each cemented soil specimen preserves a certain amount of water content which could not be lost by natural drying in the air. This preserved water content has slight effect on the wave velocity of the cemented sand.

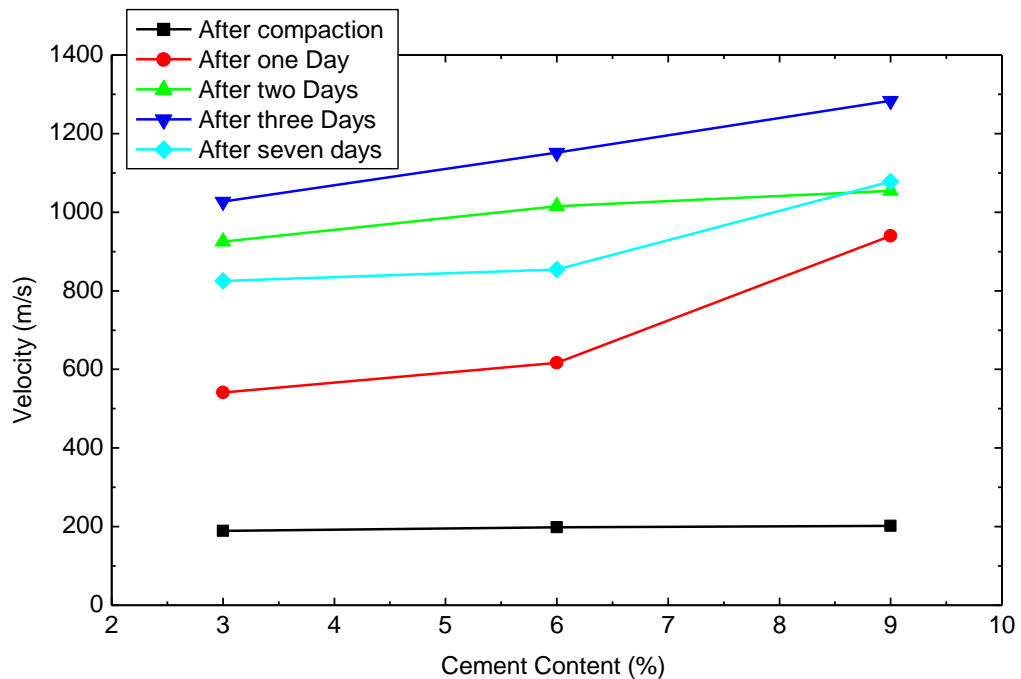


Figure 51: Variation of P-wave velocity with soil cement contents, at time of curing

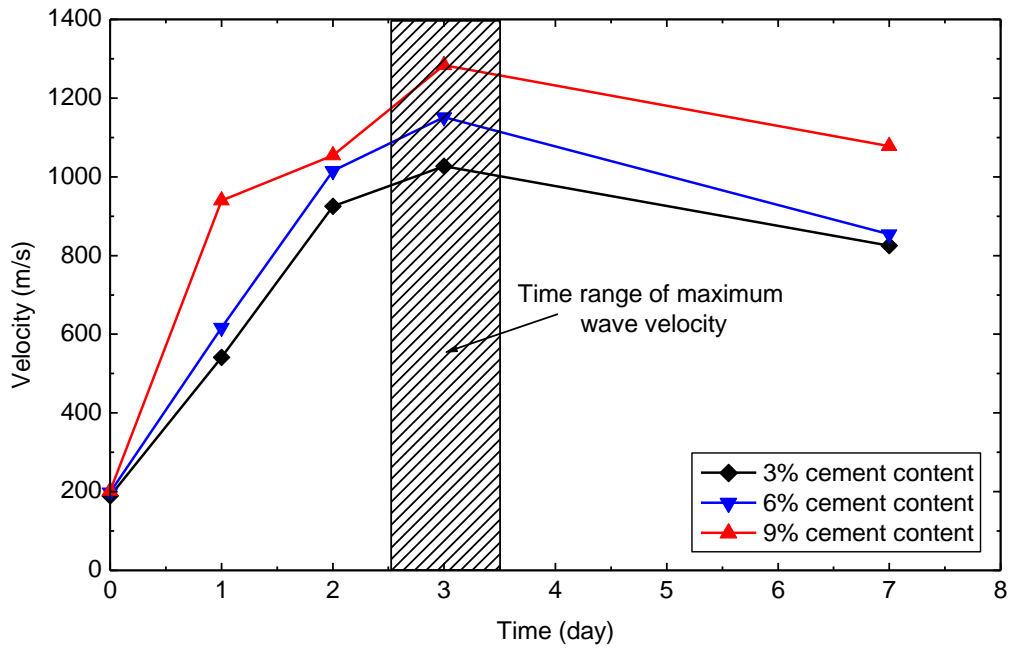


Figure 52: Variation of P-wave velocity with soil cement contents, at time of curing

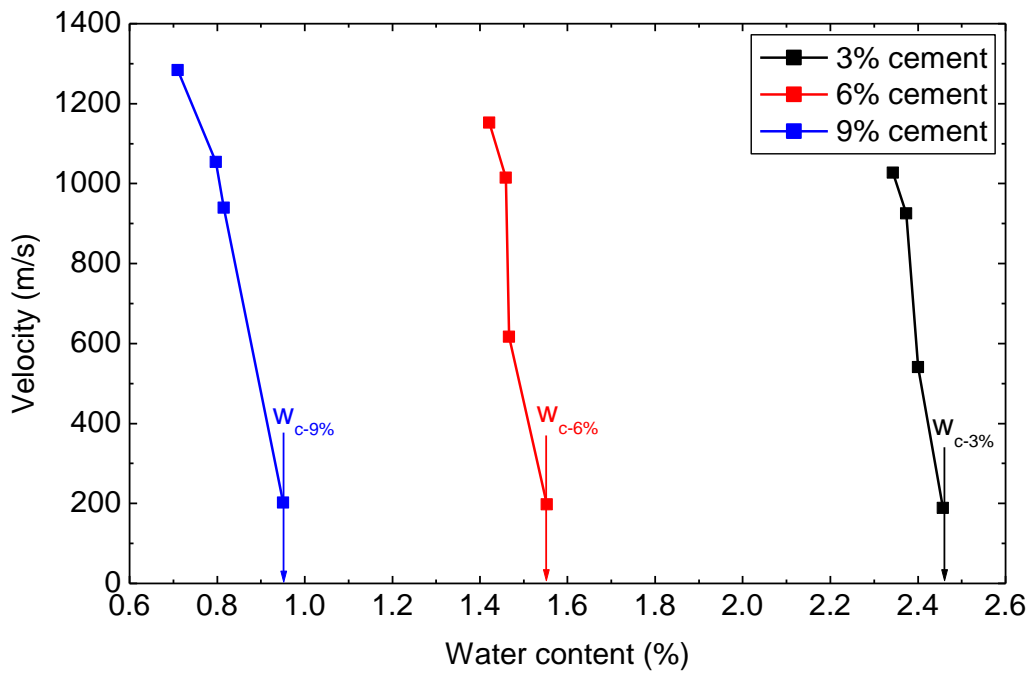


Figure 53: Variation of P-wave velocity with water contents, at different cement content percent

4.3. Strip Footing Test

4.3.1. General

As stated in Chapter 3, the second phase of this research program is to construct a one-third scale model strip footing test. The main objective of the scaled model test is to measure the variation of wave velocity with the applied load capacity through different locations in the backfill around and below the strip footing. To achieve this objective, a strip footing with specific dimensions is constructed inside the sand box described in Chapter 3. The model was equipped with 12 geophones and 4 accelerometers, distributed as shown in Figure 54. All geophones are 20 cm apart from each other in the horizontal direction and 15 cm in the vertical direction. Figure 54 shows the right side view of the sand box where geophones 1, 5, and 9 are the closest to the location of both hits (side and top). This section presents the effect of footing vertical stresses on the measured wave velocity on the soil backfill underneath the footing.

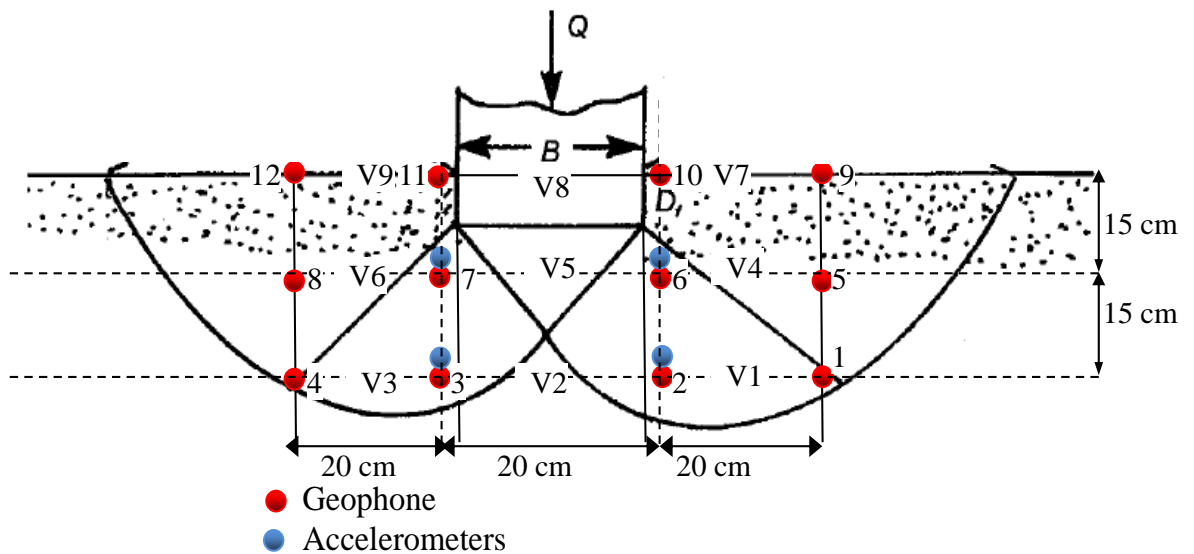


Figure 54: Distribution of geophones and accelerometers on the scaled model strip footing

4.3.2. Wave velocity at different vertical stresses

Figure 55 shows histograms of measured wave velocity at different locations, under and around the footing, calculated using the first arrivals of each two adjacent geophones. The wave velocity histograms presented in Figure 55 are for different vertical stress increments applied at the top of the strip footing. The green colored columns represent wave velocity at the backfill surface, the blue colored columns represent wave velocity at depth of 30 cm from the backfill surface, and the brown colored columns represent wave velocity at 15 cm from the backfill surface. The middle green column represents the wave velocity measured directly under the strip footing. It is clear from Figure 55a that the wave velocity measured at the backfill surface at zero footing stress is lesser than the wave velocity at other depths. As the depth below the footing increases, the measured wave velocity increases. Once the first stress increment on the strip footing is applied, the stress measured at the backfill surface increases and becomes larger than the other values of wave velocities measured at other depths (see Figure 55b). The trend of increasing wave velocity at the backfill surface compared to wave velocity at other depths is repeated with all stress increments at Figure 55. In addition, the measured velocities at all depths increase with increasing the applied vertical stress at the top of the strip footing. Finally, the largest values of wave velocity are measured at a vertical applied stress $\sigma_v = 771$ kPa (see Figure 55h).

Figure 55 displays snap shots of the wave velocity at different locations, and at selected values of vertical stresses applied on the strip footing. However, Figure 56 presents variation of the wave velocities with the applied vertical stresses by strip footing, measured at different locations. Locations of the measured velocities V_1 to V_9 are indicated in Figure 54. Figure 56 shows the measurement of velocity due to two impulses, one from the back of the box, and the other from the top of the back fill, as explained in Chapter 3. It can be seen from Figure 56 that the velocity calculated using side and top hits (V_s and V_t) are in close agreement at all locations (i.e., V_1 to V_9), and at all applied vertical stress increments. Slight disagreements between the velocities measured from the side hits and those measured from the top hits occur at some applied stress increments. For example, for velocity V_1 , Figure 56a shows some discrepancies at vertical stresses $\sigma_v = 200$ kPa, and 800 kPa. For velocity V_3 , Figure

56c shows slight disagreement that occurs at vertical stress $\sigma_v = 675$ kPa, and similar disagreement that occurs for velocity V_4 at vertical stress $\sigma_v = 350$ kPa. For velocity V_7 , Figure 56g indicates significant discrepancies that occur at almost all applied vertical stresses. Finally, for velocity V_9 , Figure 56I shows discrepancies that occur at vertical stresses $\sigma_v = 300$ kPa and 800 kPa.

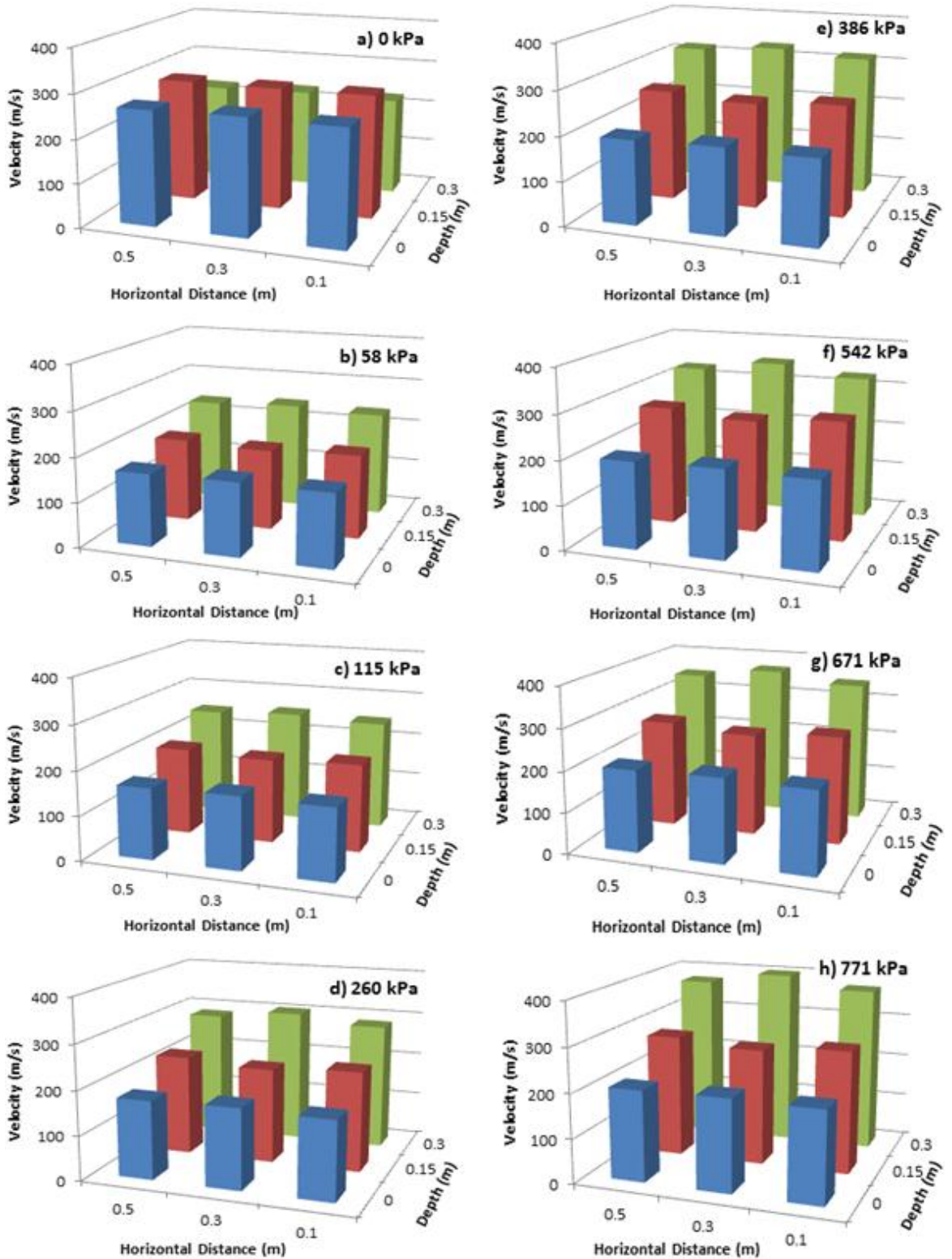


Figure 55: Variation of wave velocity at different locations under strip footing at different vertical stresses

To eliminate the difference in velocity between side and top hits, an average value of the velocity is calculated and used at each location. It can be seen that the

wave velocities measured at all locations under the strip footing increase with the applied vertical stresses. The initial average wave velocity for unloaded backfill soil is measured to be 275 m/s before it reduced to an average velocity of 210 m/s with first seating stress which is equal to 10.5 kPa. The only exception of that are velocities V_2 and V_3 which reduced to 140 m/s at the seating stress, and V_6 which reduced to 90 m/s at the seating stress. After this reduction of the wave velocity under seating stress, all velocities start to pick up and increase under subsequent stresses. However, velocities at different locations increase with different values at the same vertical stress value. A comparison between individual velocities variations with applied vertical stress can be seen in Figure 56.

Figure 57 shows a comparison between velocities measured with geophones and accelerometers at two different locations, V_2 and V_5 . V_5 is the velocity measured directly under the footing at depth equal to B , and V_2 is the velocity measured at depth equal to $2B$ under the footing. An example of accelerometer readings used to calculate V_2 and V_5 is shown in Figure 58. The time difference between the sender accelerometer and the receiver accelerometer is clear from the figure. This time difference is used together with the horizontal distance between the two accelerometers to calculate the wave velocity. De-amplification of the response is also clear between the input and output responses in Figure 58. This de-amplification is expected to be due to soil damping. Back to Figure 57, it can be noticed that the P-wave velocities V_2 and V_5 measured using accelerometers are relatively larger compared to the same velocities measured using geophones. In addition, the velocities measured using accelerometers are more scattered than those measured using geophones. However, the average of the velocity of the accelerometers using top and side hits, V_{acc_t} and V_{acc_s} , respectively, eliminates some of these scatterings, which is shown by V_{acc_av} in Figure 57.

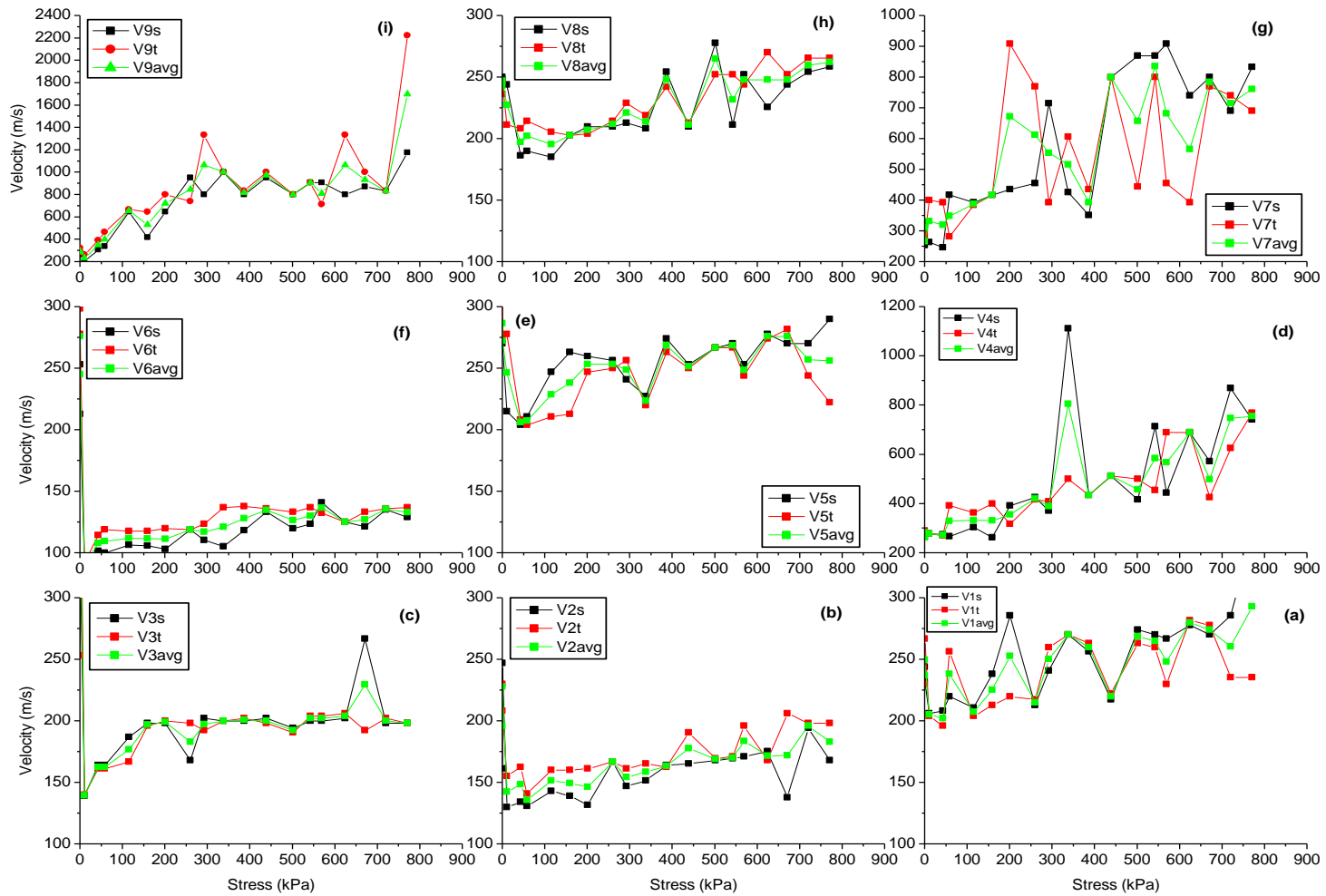


Figure 56: Variation of wave velocity with vertical stresses at different locations under strip footing

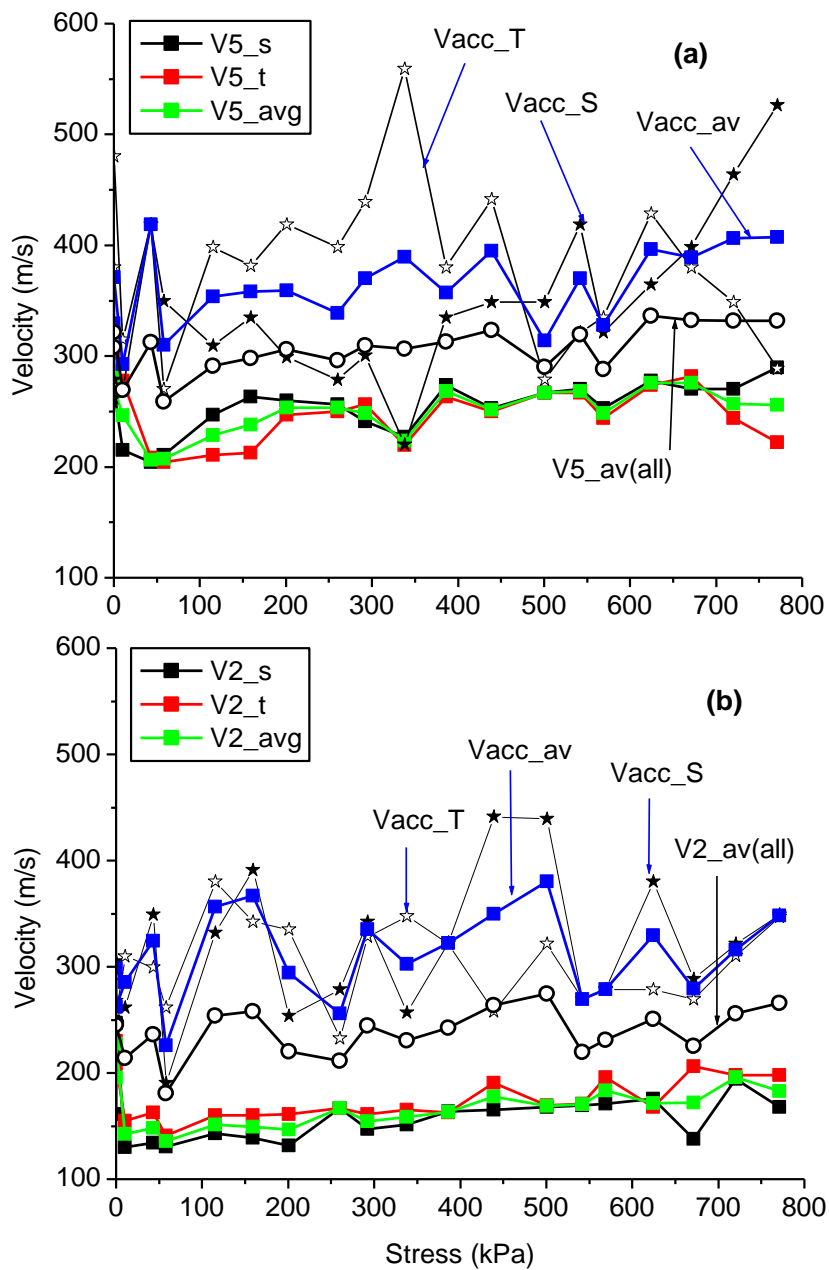


Figure 57: Comparison between variation of wave velocity V_2 and V_5 measured with geophones and accelerometers with the applied vertical stresses

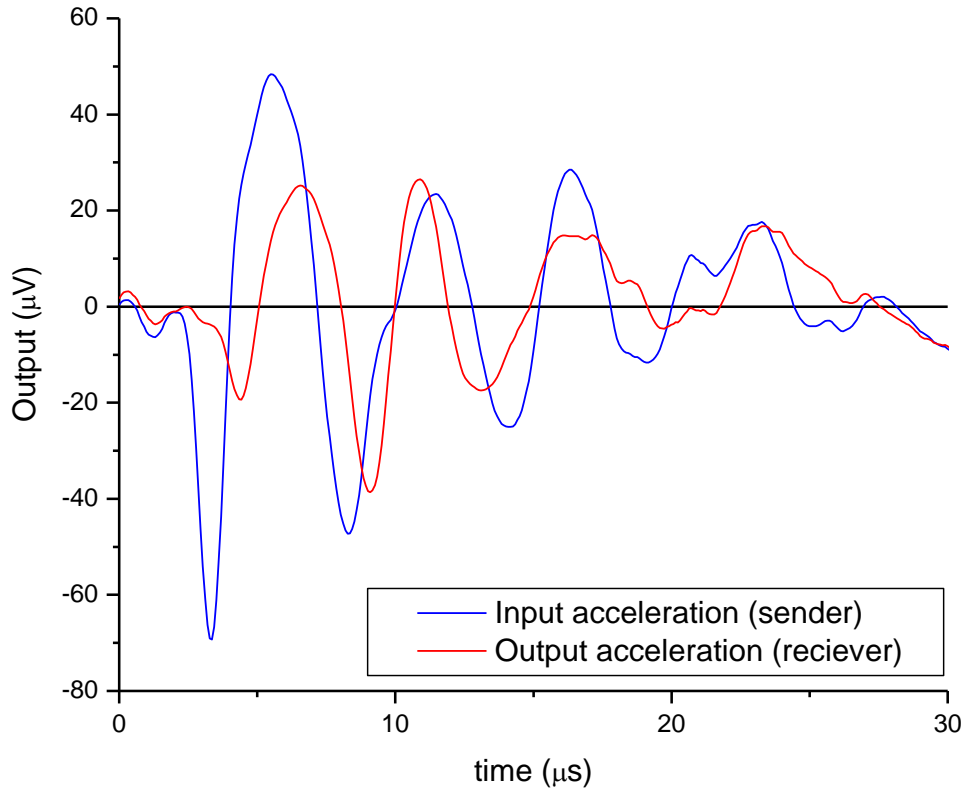


Figure 58: Example acceleration responses (sender and receiver) at side hit

The values $V_{2av(all)}$ and $V_{5av(all)}$ shown in Figure 57 are used in all calculations presented in next sections to represent V_2 and V_5 .

To engage all geophones in different arrangement and different combinations, wave velocities have been calculated using mixed combinations of geophones. Instead of using each two adjacent geophones with a horizontal distance $x = 20$ cm (e.g., geophones at nodes 1 and 2, 3 and 4, etc.), geophones with larger horizontal distances of $x = 40$ (e.g., geophones at nodes 1 and 3, 2 and 4, etc.), and cm and $x = 60$ cm (e.g., geophones at nodes 1 and 4, 5 and 8, etc.) are used as pairs to calculate values of wave velocity. This gives a better representative of the velocities by covering larger distances that the velocities propagate through. Locations of different nodes where geophones are inserted are shown in Figure 59. Results of this process are shown in Figures 60 to 62 in a version of the variation of wave velocities at different locations versus applied vertical stresses. It is clear that the wave velocity increases with the applied vertical stresses. This is true at all locations under the strip footing; however, different increase occurs at different locations. It could be noticed that the velocities measured at the right side of the footing (V_{9-11} , V_{5-7} , and V_{1-3}) are larger than the

velocities measured at left side of the footing (V_{10-12} , V_{6-8} , and V_{2-4}). This is except for the velocity measured at the top backfill surface where the velocity measured at the right side of the footing, V_{9-11} , is slightly lower than that measured at the left side, V_{10-12} . For the velocity measured using the larger distance $x = 60$ cm (V_{9-11} , V_{5-8} and V_{1-4}), Figures 60 to 62 indicate that these velocities are the largest among other velocities measured at the same depth, except for velocity V_{5-8} calculated at depth $d = B$ from the top surface, which is not the largest at the same depth.

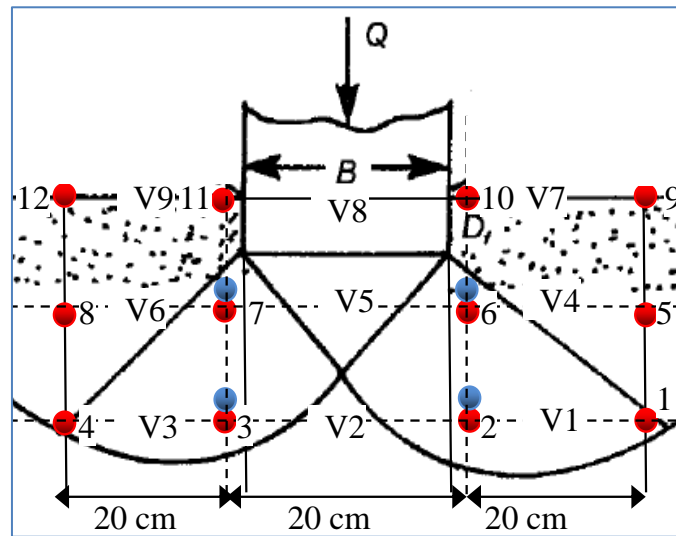


Figure 59: Locations of different nodes where geophones are inserted

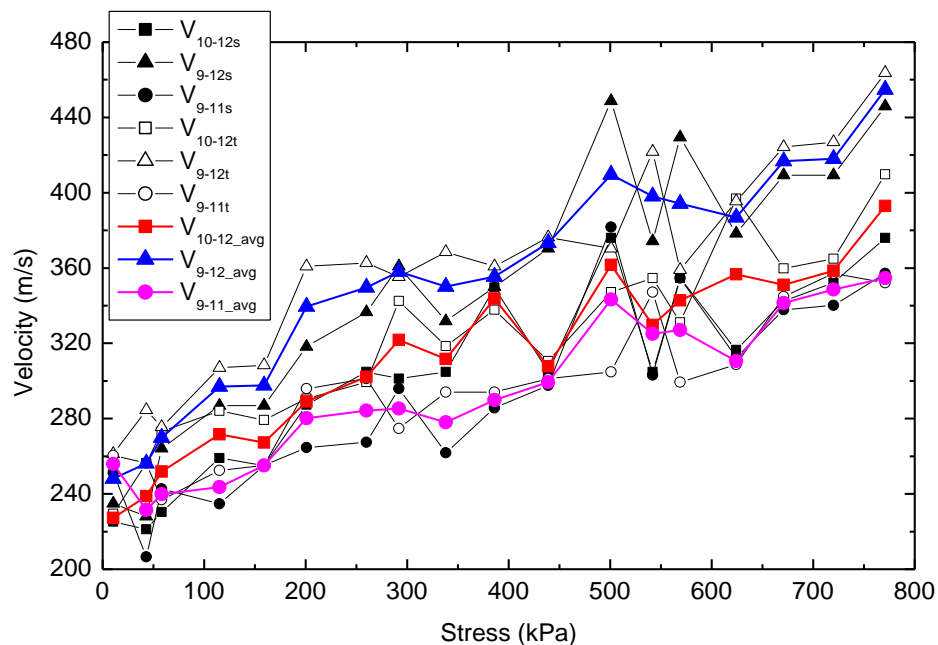


Figure 60: Variation of wave velocity at different top surface locations with vertical stresses

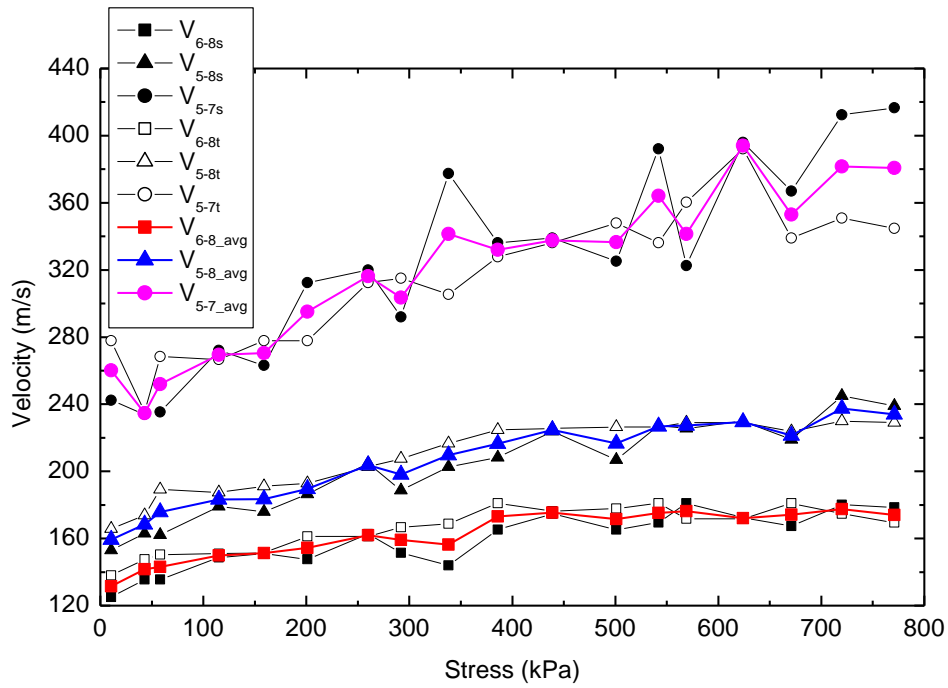


Figure 61: Variation of wave velocity at different locations of depth $d = B$ from the surface with vertical stresses

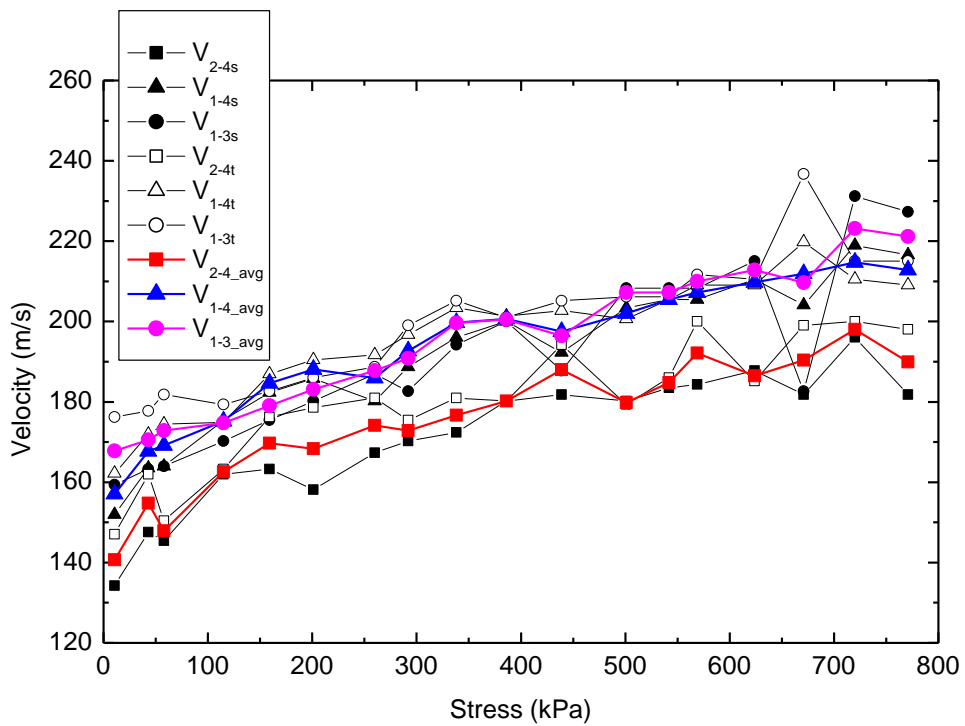


Figure 62: Variation of wave velocity at different locations of depth $d = 2B$ from the surface with vertical stresses

4.3.3. Average velocities

The short distances localized velocities calculated using geophones at horizontal distances of $x = 20$ cm (presented in Figure 56), and the velocities

calculated using long horizontal distances $x = 40$ cm and 60 cm (presented in Figures 60-62) are used to calculate average velocities at different locations. For example, the final velocity V_1 is calculated using Equation (4.1), and the final velocity V_2 is calculated using Equation (4.2). Definitions of all velocities that appear in these two equations can be found on Figure 56, and Figures 60-62. In addition, the symmetrical conditions, both geometrical and loading, in Figure 59 are considered by assuming that the velocities $V_1 = V_3$, $V_4 = V_6$, and $V_7 = V_9$. This approximation and assumption reduces the number of velocities that can be used in the result analysis and interpretations. In addition, it eliminates the effect of the left side of the steel box which is closer to the location of the footing compared to the right side.

$$V_1 = V_3 = \frac{V_{1-3avg} + V_{2-4avg} + V_{1avg} + V_{3avg}}{4} \quad (4.1)$$

$$V_2 = \frac{V_{1-3avg} + V_{2-4avg} + V_{1-4avg} + V_{2avg}}{4} \quad (4.2)$$

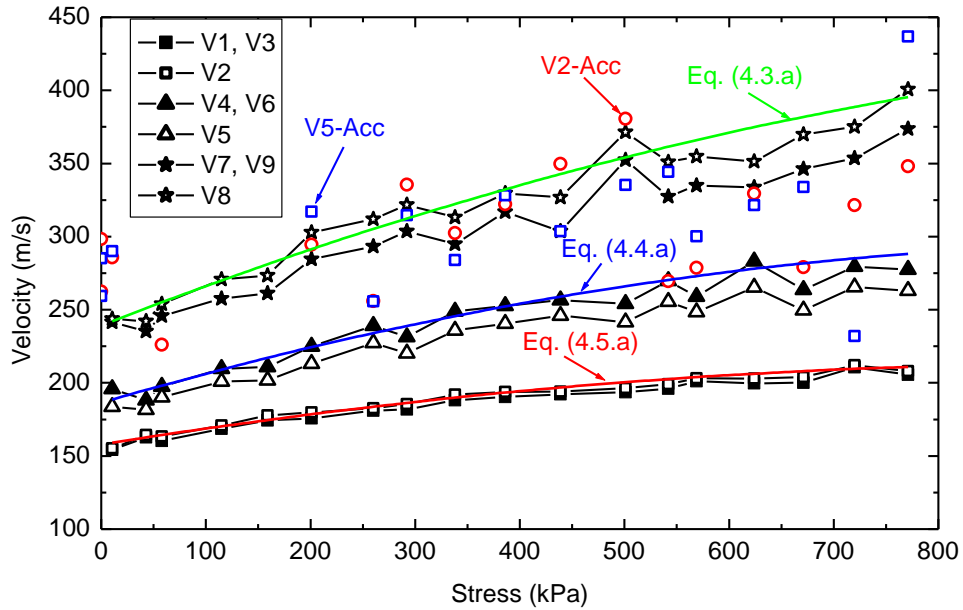


Figure 63: Variation of wave velocity at depths $d = 0$, B , and $2B$ from the backfill surface with vertical stresses

Similar expressions have been used to calculate the final velocity values for V_4 - V_9 . These mathematical calculations used for different wave velocities result in a relatively smooth trend of velocity variation with the applied vertical stresses on the strip footing. In addition, they engage several geophones in the calculation of each

velocity instead of just 2 local geophones. Results of these calculation processes are shown in Figure 63 as a variation of the final velocities V_I-V_o versus vertical stresses applied on the strip footing. It can be seen from Figure 63 that all velocities increase with the increase in the vertical stress. In addition, the variation of the wave velocity with vertical stress is slightly non-linear for all locations. It could be seen that the initial velocities at different locations are $V_o= 240, 186$ and 158 m/s for $d = 0, B,$ and $2B,$ respectively. In addition, the increase in the velocity due to the applied vertical stress is larger for the location $d = 0$ compared to the other locations $d = B$ and $2B.$ In this regard, the velocity measured at location $d = 0$ is $V_{d=0} = 396$ m/s at vertical stress $\sigma_v = 770$ kN/m² while the velocity $V_{d=2B} = 210$ m/s at the same applied vertical stress of $\sigma_v = 770$ kN/m². Therefore, for the same increase of applied vertical stress $\Delta\sigma_v = 770$ kN/m², the velocity under the footing increases with $\Delta V = 156$ and 52 m/s at locations $d = 0$ (directly under the footing) and $2B,$ respectively. The nonlinear and linear relationships that relate velocity change ΔV (i.e., velocity increase above V_o) at different locations with the applied vertical stress $\sigma_v,$ are given by the following relationships:

$$\Delta V_{top} = 0.28\sigma_v - 0.0001\sigma_v^2 \quad (R^2 = 0.955) \quad (4.3.a)$$

$$\Delta V_{top} = 0.19\sigma_v \quad (R^2 = 0.939) \quad (4.3.b)$$

$$\Delta V_{d=B} = 0.21\sigma_v - 0.0001\sigma_v^2 \quad (R^2 = 0.958) \quad (4.4.a)$$

$$\Delta V_{d=B} = 0.12\sigma_v \quad (R^2 = 0.921) \quad (4.4.b)$$

$$\Delta V_{d=2B} = 0.115\sigma_v - 0.00006\sigma_v^2 \quad (R^2 = 0.955) \quad (4.5.a)$$

$$\Delta V_{d=2B} = 0.066\sigma_v \quad (R^2 = 0.931) \quad (4.5.b)$$

In the above set of equations, $\Delta V_{top}, \Delta V_{d=B},$ and $\Delta V_{d=2B}$ are velocity increases calculated at $d = 0, B,$ and $2B,$ respectively, and σ_v is the vertical stress applied at the top of the ground surface using a strip footing shape with width $B.$ It can be seen from the correlation coefficient R^2 associated to each equation that the nonlinear equations are better fit of the measured data compared to the linear equations. However, the improvement in the correlation coefficient is not significant if the nonlinear relations are used instead of linear relations.

Based on the results presented in Figure 63, the percentage increase in the wave velocity ($\Delta V/V_o$) due to the application of the strip footing vertical stress is calculated and presented in Figure 64 at $d = 0, B$, and $2B$. As expected, the percentage increase in the wave velocity ($\Delta V/V_o$) increases as the vertical stresses applied on the strip footing increase. The variation of the percentage increase in the wave velocity is nonlinear with the applied vertical stress. In addition, the percentage increase in the wave velocity is smaller as the depth below the strip footing becomes larger. Three nonlinear relationships are derived to relate the percentage changes in wave velocity ($\Delta V/V_o$) with the variation of σ_v . Equation (4.6) represents the bottom boundary of the measured data at depth $d = 2B$ while Equation (4.8) represents the upper boundary of the measured data at depth $d = 0.0$. Equation (4.7) is derived based on the other two equations to represent the average response of the wave velocity change ($\Delta V/V_o$) with the variation of σ_v . The three equations are formulated based on regression analysis and take the following forms:

$$\frac{\Delta V}{V_o} = 0.0793\sigma_v - 5 \times 10^{-3} \sigma_v^2 \dots \dots (R^2 = 0.97) \quad (4.6)$$

$$\frac{\Delta V}{V_o} = 0.0881\sigma_v - 6 \times 10^{-4} \sigma_v^2 \dots \dots (R^2 = 0.94) \quad (4.7)$$

$$\frac{\Delta V}{V_o} = 0.13\sigma_v - 7 \times 10^{-3} \sigma_v^2 \dots \dots (R^2 = 0.93) \quad (4.8)$$

The variation of the change in wave velocity could be interpreted in the form of the stress variation calculated under strip footing using the principles of the theory of elasticity. Equation (4.9) is used to calculate the vertical stress σ_{v-d} at a point located at depth d caused by a strip footing, applying a vertical stress σ_v at the foundation level (i.e., at $d = 0$) as follows:

$$\sigma_{v(d)} = \frac{\sigma_{v(d=0)}}{\pi} \left\{ \tan^{-1} \left[\frac{d}{x - \left(\frac{B}{2}\right)} \right] - \tan^{-1} \left[\frac{d}{x + \left(\frac{B}{2}\right)} \right] - \frac{Bd \left[x^2 - d^2 - \left(\frac{B^2}{4}\right) \right]}{\left[x^2 + d^2 - \left(\frac{B^2}{4}\right) \right]^2 + B^2 d^2} \right\} \quad (4.9)$$

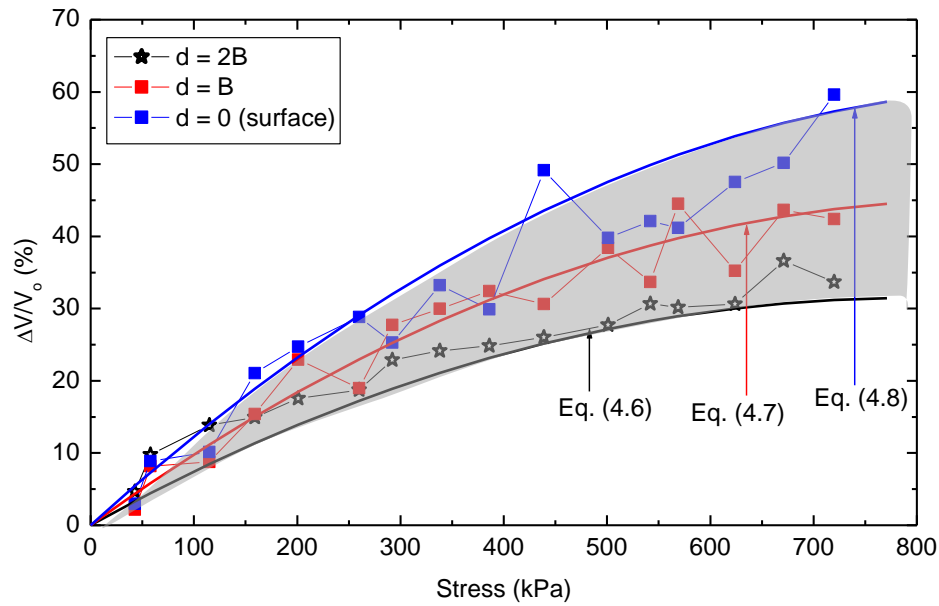


Figure 64: Variation of percentage increase in wave velocity at depths $d = 0, B,$ and $2B$ from the backfill surface with vertical stresses

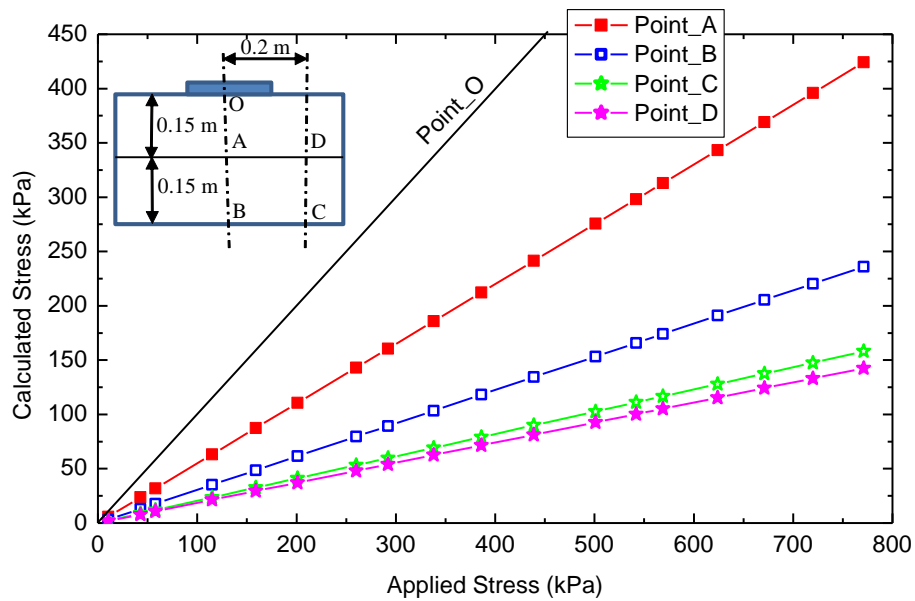


Figure 65: Variation of stress calculated using Equation (4.9) at different locations with the applied vertical stresses

Where d is the depth below the footing bottom surface (foundation level), B is the width of the strip footing, and x is the horizontal distance between the point and the centerline of the footing. Results of the application of Equation (4.9) at points O, A, B, C, and D that are located at different depths are shown in Figure 65. These points are chosen as representatives of the wave velocities $V_8, V_5, V_2, V_1,$ and $V_4,$ respectively. It can be seen that stresses decrease as the depth (d) below the footing

increases. In addition, as the point move further from the strip footing centerline in the horizontal direction, the vertical stress at the point decreases. It could be seen that stresses calculated at points C and D are nearly equal in magnitude despite the difference in x and d for both points. This could be attributed to the location of the two points at the same stress isobar (i.e., stress contour line). It can be seen that the wave velocity changes ($\Delta V/V_o$) with the applied vertical stress σ_v , shown in Figure 64, following the variation of the vertical stresses calculated at different depth. In other words, the change in wave velocity ($\Delta V/V_o$) at $d = 0$ is the largest as the calculated vertical stress is the largest. Similarly, the change in velocity at $d = 2B$ is the smallest as the calculated vertical stress is the smallest. The only exception is the nonlinear trend of the variation of wave velocity with calculated stress, which is different from the linear trend in case of calculated vertical stress. It can be concluded that the velocity variation with the applied stress on the strip footing is similar to the vertical stress variation calculated at different depths.

To eliminate the depth effect on wave velocity and stress changes, normalized velocity ratio and stress ratio are calculated and plotted in Figure 66. The applied vertical stress σ_v at the level of foundation can be calculated using Equation (4.10) together with the wave velocity measured at the foundation level $V_{d=0}$ and at any depth d , V_d . The vertical stress at the depth d below the foundation level $\sigma_{v(d)}$ can be related to the applied vertical stress σ_v through Equation (4.9) presented in the previous paragraph.

$$\frac{\sigma_v}{\sigma_{v(d)}} = 0.18e^{1.7\left(\frac{V_{d=0}}{V_d}\right)} \dots(R^2=0.996) \quad (4.10)$$

Equation (4.10) can be used to calculate the stress applied at any level with the velocity ratio at two different depths. This can be done by measuring the velocity profile with depth, using geophones, and calculating the stress profile with depth using Equation (4.9).

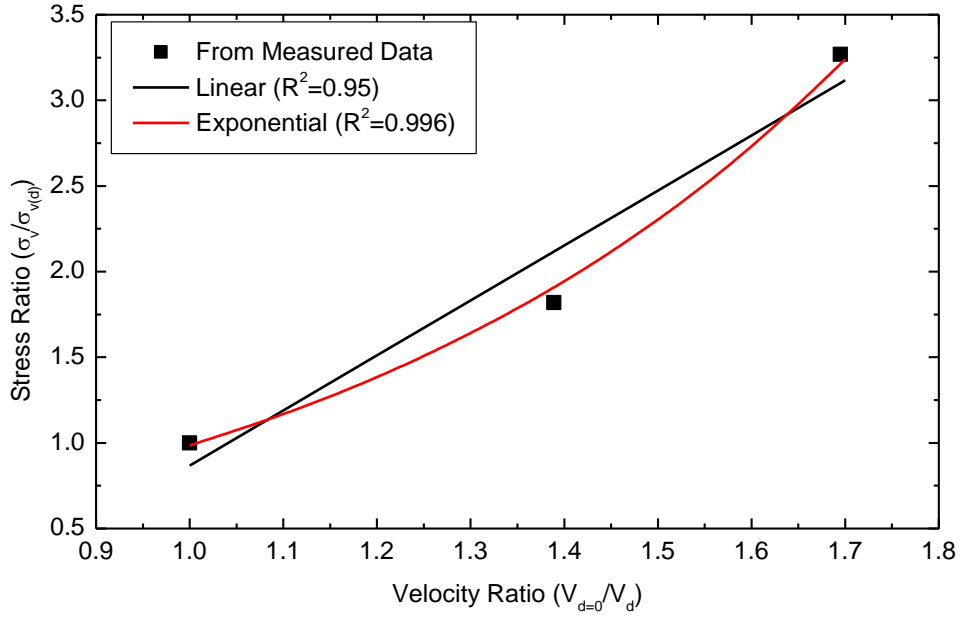


Figure 66: Variation of stress ratio versus velocity ratio

$$\frac{V_{d=0}}{V_d} = 0.59 \ln\left(\frac{\sigma_v}{\sigma_{v(d)}}\right) + 1.013 \dots \dots (R^2=0.996) \quad (4.11)$$

Equation (4.10) could be reformatted in different way to be used to calculate the variation of normalized P-wave velocity under the strip footing ($V_{d=0}/V_d$) at different applied vertical stress σ_v , as shown in Equation (4.11). Vertical stress at depth d in Equation (4.11) could be calculated using Equation (4.9).

Chapter 5: Conclusion and Recommendations

5.1 Conclusion

In this study, a number of twenty index tests have been conducted in the Geotechnical Engineering Lab at the AUS. Index tests were performed in order to study the effect of different soil parameters on the soil wave velocity. The effect of degree of compaction which is reflected on the void ratio of each soil specimen is investigated. The current research uses different soil gradation, starting with original RAK sandy soil which is passing No. 4 sieve, moving to modified RAK soil passing 2 mm and 1.18 mm sieves, and ending with fine RAK sandy soil that is passing 0.6 mm sieve. In addition, the effect of clay content on the measured wave velocity is explored and presented. Finally, the effect of cement inclusion with the modified original RAK soil passed by 2 mm sieve is presented and explained. In addition to all these soil parameters, different water contents and degrees of saturation were used to highlight the effect of water on the measured wave velocity. Based on the results of these index tests, the following important outcomes are worth noting:

1. Generally, the P-wave velocity decreases with increasing water and degree of saturation up to threshold values; whereas, the wave velocity shows no change. The water content threshold value ranges between 3.75% to 4.5%, and the degree of saturation threshold values start at 20% for lightly compacted specimen to 50% for heavily compacted specimen.
2. Void ratio of the soil specimens decreases as the compaction effort increases, and thus the soil wave velocity increases.
3. P-wave velocity increases as the soil gradation becomes finer, or when the soil fine content percent increases. This is usually accompanied by a reduction in the soil void ratio.
4. Regardless of the soil gradation, the wave velocity decreases with the water content and degree of saturation percent, up to threshold values, where the velocity starts to show slight increase. Value of saturation threshold increases as the soil fine content percent increases, or as the soil grading curve moves towards the finer side of the grain size distribution.

5. The effect of compaction effort on wave velocity is similar to the effect of fine contents, as both lead to a change in void ratio and hence a change in wave velocity.
6. The contamination of sand with clay contents significantly increases the P-wave velocity up to 10% clay content. This conclusion is true for degree of saturation less than 30%. Once the clay content increases beyond 10% and/or the degree of saturation increases beyond 30%, wave velocity starts to decrease. In conclusion, the effect of the clay content on the wave velocity also depends on the water content and degree of saturation.
7. Values of threshold degree of saturation, where the wave velocity starts to decrease/increase with clay content, increases as the clay content increases.
8. Wave velocity increases as the cement content increases, and the largest wave velocity was recorded after 3 days of curing time regardless of the cement content percent. It is worth noting that more curing time beyond 3 days does not improve the wave velocity further.
9. Cement content of 3% is found to be significantly effective in increasing the wave velocity of sand; however, increasing the cement content beyond this percentage doesn't improve the wave velocity equivalently.

This research also presents results from the large scale strip footing test. First, variation of wave velocity profile under the strip footing is presented at different applied vertical stresses. Then, wave velocity from both geophones and accelerometers is compared and presented as a relationship of footing applied stresses. Finally, the relationship between applied vertical stress at the footing and measured velocity at different locations around the footing is discussed. The following outcomes from the strip footing test are highlighted:

1. The measured wave velocity at all depths below the strip footing increases with increasing the applied vertical stress at the top of the strip footing.
2. Slight disagreements between the velocities measured from the side hits and that measured from the top hits occur at some applied stress increments, and an average value is advised to be used to estimate the final velocity at each location.
3. The P-wave velocities measured using accelerometers are relatively larger than the same velocities measured using geophones at the same location. In addition,

the velocities measured using accelerometers are more scattered than that measured using geophones.

4. Engaging all geophones in different arrangement and combination, regarding the distances, to calculate wave velocity through soil gives better representation of the velocities due to covering larger distances than the velocities propagate through.
5. The P-wave velocity measured directly under the footing represents the largest value, and then the velocity decreases with the depth under the footing. In addition, the velocity nonlinearly changes with the applied vertical stress.
6. Nonlinear relationships have been developed to calculate the increase in the P-wave velocity due to strip footing applied stress. This increase can be used with V_o , that can be measured using any suitable method, to estimate the change in soil modulus at different depths below the footing.
7. A nonlinear logarithmic relationship is developed to relate the normalized vertical stress applied at the strip footing to the normalized velocity measured under the strip footing.

5.2 Recommendations for Future Research

Based on the results and conclusion discussed in this research, the following recommendations are suggested for future work:

1. Other percentages of water contents could be investigated for the same soil types.
2. Different types of sandy soils could be tested in order to generalize the results of this research.
3. Different soil parameters could be tested and related to the soil wave velocity.
4. Other measurement techniques like ultrasonic Pundits and Bender elements can be used to test more samples and verify the two methods of measurements against each other.
5. Different values of clay and cement contents need to be tested.

References

- [1] E. J Bowles. *Foundation Analysis and Design*. McGraw-Hill, 1996, pp. 115-117.
- [2] B. M Das. *Principles of Foundation Engineering*. Thomson Brooks, 2004, pp. 97-99.
- [3] S. L Kramer. *Geotechnical Earthquake Engineering*. Prentice Hall, 1996, pp. 67-70.
- [4] Amaral, M., Vianada Fonseca, A., Arroyo, M., Cascante, G., and Carvalho, J.M. "Compression and shear wave propagation in cemented-sand specimens." *Géotechnique Letters*, vol. 54, pp. 1-6, 2011.
- [5] Pineda, J.A., Arroyo, M., Romero, E., and Alonso, E.E. "Dynamic tracking of hydraulically induced clay stoned egradation." in *Proc. of the 4th International Symposium Deformation Characteristics of Geomaterials*, 2008, pp. 809-817.
- [6] Santamarina, J. C., Klein, K. A., and Fam, M. A. *Soils and Waves*. Chichester, UK, 2001, pp. 145-148.
- [7] K.F. Oyedele, S. Oladele and O. Adedoyin. "Application of Geophysical and Geotechnical Methods to Site Characterization for Construction Purposes at Ikoyi, Lagos, Nigeria." *Journal of Earth Sciences and Geotechnical Engineering*, vol. 1, pp. 87-100, 2011.
- [8] M. Jamiolkowski. "Role of Geophysical Testing in Geotechnical Site Characterization." *Soils and Rocks*, vol. 35, pp. 1-21, 2012.
- [9] Sirikarn Narongsirikul. "rock physics/ reservoir geophysics/ geomechanics." Ph.D. Candidate, University of Oslo and Norwegian Geotechnical Institute, Norway, 2013.
- [10] Gardner G.H.F, Gardner L.W, and Gregory A.R. "Formation velocity and density the diagnostic basics for stratigraphic traps." *Geophysics*, vol. 39, pp. 770-780, 1974.
- [11] Dey A.K and Stewart R.R. "Predicting density using Vs and Gardner's relationship." *Crewes*, vol. 13, pp. 77-82, 2001.
- [12] Minsu Cha and Gye-Chun Cho. "Shear Strength Estimation of Sandy Soils Using Shear Wave Velocity." *Geotechnical Testing Journal*, vol. 6, no. 30, pp. 1-12, 2007.
- [13] Sirles. *Geophysical Methods Commonly Employed for Geotechnical Site Characterization*. Washington, 2006, pp. 1-44.

- [14] Schulze W.E. *Deutsche Forschungsgesellschaft für Bodenmechanik*, 7th ed. Leipzig, 1943, pp. 150-157.
- [15] Hardin B. O and Black W.L. "Vibration modulus of normally consolidated clays." *Journal of the Soil Mechanics and Foundation Division, ASCE*, vol. 94, pp. 353-369, 1968.
- [16] Hardin B.O and Drnevich V.P. "Shear modulus and damping in soils ." *Journal of the Soil Mechanics and Foundation Division ASCE*, vol. 98, pp. 667-692, 1972.
- [17] Ohkubo T and Terasaki A, Physical property and seismic wave velocity of Rocks. Japan: OYO Corporation, 1976.
- [18] Tezcan Semih, Ozdemir Zuhail , Keceli Ali , and Erkal Aykut. "A Rapid Technique to Determine Allowable Bearing Pressure." *International Earthquake Symposium Kocaeli, Istanbul*, vol. 22, pp. 234-241, 2007.
- [19] Tezcan S. S and Ozdemir Z. "Allowable Bearing Pressure in Soils and Rocks through Seismic Wave Velocities." *Earth Science Research*, vol. 28, pp. 170-179, 2012.
- [20] Joseph Gordian Atat, Idara Okan Akpabio, and Nyak. "Allowable Bearing Capacity for Shallow Foundation in Eket Local Government Area, Akwa Ibom State, Southern Nigeria." *International Journal of Geoscience*, vol. 22, pp. 110-117, 2013.
- [21] G.G Meyerhof. "Some recent research on the bearing capacity of foundations." *Canadian Geotechnical Journal*, vol. 1, pp. 16-26, 1963.
- [22] Vesil A. "Theoretical Studies of Cratering Mechanisms Affecting the Stability of Cratered Slopes." *US Army Engineer Nuclear Cratering Group of Atlanta*, vol. 22, pp. 10-123, 1963.
- [23] Terzaghi K and Peck R.B. *Soil mechanics in engineering practice*. New York, 1948, pp. 120-128.
- [24] Krizek R. J. "Approximation for Terzaghi's bearing capacity." *Journal of Soil Mechanics & Foundations*, vol. 91, pp. 1-3, 1965.
- [25] R. Wicaksono, Y. Tsutsumi, T. Sato, J. Koseki and R. Kuwano. "Laboratory Wave Measurementson Toyoura Sandand Hime Gravel." *Bulletin of ERS*, vol. 41, pp. 123-129, 2011.
- [26] Ning. Z and Evans. T.M. "Discrete Element Method Study of Shear Wave Propagation in Granular Soil." *in Proc. of the 18th International Conference on Soil Mechanics and Geotechnical Engineering*, 2013, pp.1031-1034.
- [27] R. Zhang, B. Jiang and W. Cao. "Influence of sample size on ultrasonic phase velocity measurements in piezoelectric ceramics." *Journal of Applied Physics*,

vol. 91, no. 12, pp. 94-101, 2002.

- [28] A. Heitor, B. Indraratna and C. Rujikiatkamjorn. "Characterising Compacted Soil Using Shear Wave Velocity and Matric Suction." *Australian Geomechanics*, vol. 47, no. 2, pp. 79-86, 2012.
- [29] B. Bonner, P. Berge and D. Wildenschild. "Compressional and Shear Wave Velocities for Artificial Granular Media Under Simulated Near Surface Conditions." *SEG Technical Programme Expanded Abstracts*, vol. 9, pp. 1419-1422, 2001.
- [30] B. Indraratna, A. Heitor and C. Rujikiatkamjorn. "Effect of compaction energy on shear wave velocity of dynamically compacted silty sand soil." in *Proc. 5th Asia-Pacific Conference on Unsaturated Soils*, 2012, pp. 635-640.
- [31] S. Thevanayagam, T. Shenthan and T. Kanagalingam, "Role of Intergranular Contact on Mechanisms Causing Liquefaction & Slope Failures in Silty Sands." *Mechanics and Geotechnical Engineering*, vol. 7, pp. 126-131, 2017.
- [32] Drury, J C. "Ultrasonics Part 7. The ultrasonic beam." *Insight - Non-Destructive Testing and Condition Monitoring*, vol. 47, No. 5, pp. 297-299, 2005.
- [33] Marjanovic, J. "The Study of Shear and Longitudinal Velocity Measurements of Sands and Cohesive Soils." Master's Thesis, Massachusetts Institute of Technology, Cambridge, USA, 2012.
- [34] D. A. Black. "Shear Wave Velocity Measurement of Kaolin During Undrained Unconsolidated Triaxial Compression." in *Proc. 62nd Canadian Geotechnical Conference*, 2009, pp. 552-596.
- [35] Viggiani, G. and Atkinson, J.H. "Interpretation of bender element tests." *Géotechnique*, vol. 45, pp. 149-154, 1995.
- [36] Arulnathan, R., Boulanger, R.W. and Riemer, M.F. "Analysis of bender element tests." *ASTM Geotechnical Testing Journal*, vol. 21, pp. 120-131, 1998.
- [37] Lings, M.L. and Greening, P.D. "A novel bender/extender for soil testing." *Géotechnique*, vol. 51, pp. 713-717, 2001.
- [38] Clayton, C.R.I., Theron, M. and Best, A.I. "The measurement of vertical shear-wave velocity using side-mounted bender elements in the triaxial apparatus." *Géotechnique*, vol. 54, pp. 495-498, 2004.
- [39] Porbaha, A., Ghaeheri, F. and Puppala, A.J. "Soil cement properties from borehole geophysics correlated with laboratory tests." in *Proc. of the International Conference on Deep Mixing Best Practice and Recent Advances*, 2005, pp. 605-611.

- [40] Mohsin A.K.M. and Airey D.W. "Automating Gmax measurements in triaxial tests." in *Proc. of The Prefailure Deformation Characteristics of Geomaterials*, 2003, pp. 73-80.
- [41] Jovicic, V., Coop, M.R., Simic, M. "Objective criteria for determining Gmax from bender element tests." *Geotechnique*, vol. 46, pp. 357–362, 1996.
- [42] L. P. Suwal and R. Kuwano. "Disk shaped piezo-ceramic transducer for P and S wave measurement in a laboratory soil specimen." *Soils and Foundations*, vol. 53, no. 4, pp. 510–524, 2013.

Vita

Mohammad Okab Amer was born and raised in the city of Abu Dhabi, in the United Arab Emirates. He was educated in Al Mutanabbi Secondary School and graduated in 2010. After that, Mohammad joined the American University of Sharjah (AUS) and got his Bachelor's Degree in Civil Engineering in 2014. After graduation, Mohammad received a scholarship from the AUS to continue his higher studies and pursue a Master's Degree in Civil Engineering. During his study, he worked as a teaching assistant at AUS.